

MSc thesis in computational mechanics for civil engineering

# Modeling the finite strain response of PEEK with strain-dependent viscosity within the EGP model

Mark Aarsen  
2022





MODELLING THE FINITE STRAIN RESPONSE OF PEEK  
WITH STRAIN-DEPENDENT VISCOSITY  
WITHIN THE EGP MODEL

A thesis submitted to the Delft University of Technology in partial fulfillment of the  
requirements for the degree of Master of Science in Civil Engineering

Master of Science in Civil Engineering

by

Mark Aarsen

January 2022

Mark Aarsen: *Modelling the finite strain response of PEEK with strain-dependent viscosity within the EGP model* (2022)

© This work is licensed under a Creative Commons Attribution 4.0 International License. To view a copy of this license, visit

<http://creativecommons.org/licenses/by/4.0/>.

The work in this thesis was made in the:



Computational Mechanics group  
Applied Mechanics Section  
Faculty of Civil Engineering and Geosciences  
Delft University of Technology

Committee: Dr.ir. F.P. (Frans) van der Meer  
Ir. C. (Cor) Kasbergen  
D. (Dragan) Kovacevic

# PREFACE

---

Dear reader,

This master thesis marks for me the end of many years of studying. First at the University of applied sciences HAN and then at the Technical University of Delft. However, that does not mean that I am done learning. I came to the TU Delft to get more insight and a better understanding of the current state of structural mechanics. That is why I would like to thank the chair of my committee, Frans van der Meer, for allowing me to graduate within the computational mechanics group at the TU Delft. This has given me a great insight into computational methods and viscoplastic constitutive models. He also has, together with my other committee members Dragan Kovacevic and Cor Kasbergen, given me useful directions for my research. I had weekly meetings with Dragan about the contents of my research. I would like to thank him for his guidance and time, even when most of our meetings have been online. I also want to thank my friends and parents for being able to discuss some parts of my research and for checking the final product. Specifically my mother, Esther and Rik for proofreading my thesis, which improved the quality.

I sincerely hope that this thesis is an interesting read. I also hope that it gives insight into accurately modelling PEEK with the EGP model.  
Enjoy reading!

*Mark Aarsen*  
*The Hague, January 2022*



# ABSTRACT

---

The University of Twente performed experimental uniaxial compression tests of Poly(ether-ether-ketone) (PEEK) and the TU Delft made a comparison with a numerical model; the viscoplastic Eindhoven Glassy Polymer (EGP) model. A higher strain-rate dependency and a higher yield stress at lower temperatures are observed in the experimental results. It is of importance to correctly model the stress-strain behaviour of PEEK for future research in long term behaviour of fibre reinforced PEEK by adapting the EGP model to account for these differences. The viscosity of the EGP model is based on the Ree-Eyring equation [Ree and Eyring, 1955] in which the three Ree-Eyring parameters (activation volume, activation energy and initial viscosities) are constants within the EGP model. It is observed that all three Ree-Eyring parameters are not constant over the strain when the original Ree-Eyring equation is fitted to the experimental data. Thus, non-constant Ree-Eyring parameters should be included in the EGP model. Evolving all three Ree-Eyring parameters leads to accurate stress-strain results, except for the pre-yield regime. The EGP model does not behave as stiff as the experiment in this region. Thus, a higher stiffness is included by evolving the shear moduli over the pre-yield regime. The evolution of the Ree-Eyring parameters is expressed by a  $\tanh()$  function and quadratic function, while the evolution of the shear moduli is only expressed by a  $\tanh()$  function. The evolution based on the  $\tanh()$  function mostly influences the behaviour at small strains and the evolution based on the quadratic function mostly influences the behaviour at large strains. The evolution of the Ree-Eyring parameters at large strains leads to the insertion of viscous strain hardening in the EGP model. The viscous strain hardening qualitatively describes the Bauschinger effect for a cyclic loading case. The Bauschinger effect can be explained as the change of material behaviour when stresses are present. What occurs when the loading direction reverses within a cyclic loading case. An invariant function that is proportional to the strain determines the strain dependency of the evolution of the Ree-Eyring parameters and shear moduli. This invariant function is prevented from reducing for the evolution based on the  $\tanh()$  function when the loading direction is reversed but does reduce for the evolution based on the quadratic function to correctly model cyclic loading. Furthermore, the linearization of the stiffness tensor is updated for the changes to the EGP model and a part of the stiffness tensor which was omitted in the original implementation is added.

Including the evolution of the Ree-Eyring parameters and shear moduli with the mentioned characteristics in the EGP model makes the EGP model correspond very well with the experimental results for all investigated temperatures and strain-rates.



# CONTENTS

1	INTRODUCTION	1
1.1	Experimental results	2
1.2	Thesis outline	2
2	LITERATURE REVIEW	5
2.1	Deformation behaviour of polymers	5
2.2	General overview of the EGP model	7
2.2.1	Kinematics	8
2.2.2	Hydrostatic stress	9
2.2.3	Driving stress	9
2.2.4	Hardening stress	11
3	BENCHMARK	15
3.1	Characterization of the original EGP model	15
3.2	EGP model settings/FEM settings	18
3.3	Results of the benchmark	19
3.4	Confirmation of the problem statement	22
4	STRAIN-DEPENDENT PARAMETERS	23
4.1	Ree-Eyring parameters and pressure dependency	23
4.2	Strain dependency	26
4.3	Small to moderate strain range	26
4.4	Pre-yield regime	30
4.5	Large strain range	31
4.6	Characterization of the updated EGP model	33
4.7	Evolution over the full strain range	35
4.8	Larger temperature and strain-rate range	37
5	CYCLIC LOADING	39
5.1	The invariant function	39
5.2	Comparison with literature	41
5.3	The fully updated EGP model	43
6	LINEARIZATION	45
6.1	Deviatoric stiffness tensor ${}^4S_d$	46
6.2	State variable stiffness tensor ${}^4S_x$	47
6.3	Convergence rate	50
7	CONCLUSION AND DISCUSSION	55
7.1	Recommendations	59
A	ORIGINAL EGP MODEL PARAMETERS	65
B	CHARACTERIZATION OF THE BENCHMARK	69
C	STRESS-STRAIN CURVES FROM THE BENCHMARK	71
D	STRESS-STRAIN CURVES FROM THE UPDATED EGP MODEL	75
E	UPDATED C++ CODE FOR THE STRESS CALCULATION	79
F	LARGER TEMPERATURE AND STRAIN RATE RANGE STRESS-STRAIN CURVES	83
G	DERIVATIVE OF THE VISCOSITY	85
H	UPDATED C++ CODE FOR THE STIFFNESS CALCULATION	87



## LIST OF FIGURES

Figure 1.1	The stress-strain curves of experimental uniaxial compression tests of PEEK conducted by the University of Twente at (a) 20°C, (b) 60°C and (c) 100°C. . . . .	3
Figure 2.1	Schematic and annotated stress-strain behaviour of a polymer.	6
Figure 2.2	Schematic influence of (a) different relaxation processes on the strain-rate dependency and (b) ageing at different temperatures on stress-strain results. . . . .	7
Figure 2.3	Schematisation of the EGP model stress decomposition. . . . .	8
Figure 2.4	Schematic influence of the elastic strain hardening parameters on the hardening stress contribution. . . . .	11
Figure 3.1	The strain-rate dependency of the experimental results (see section 1.1) at a strain of 0.4 shown as markers for different temperatures. The grey line is indicative for the slope. . . . .	17
Figure 3.2	The simple 8-noded hexahedral finite element. . . . .	18
Figure 3.3	(a, c, e) The difference between the experimental results and the original EGP model benchmark results. (b, d, f) The experimental stress-strain results plotted with markers and the original EGP results plotted in solid lines. Both for a number of different strain-rates and at (a, b) 20°C, (c, d) 60°C and (e, f) 100°C. The grey lines in the plots with the difference are the exact difference including the noise from the experiments while the black lines are without the noise, which are obtained by filtering the grey lines with a Butterworth filter. . . . .	20
Figure 3.4	The strain-rate dependency of the original EGP model results and experimental results for a temperature of (a) 20°C, (b) 60°C and (c) 100°C taken at a strain of 0.1. . . . .	21
Figure 3.5	The pre-yield stress-strain behaviour at 100°C of (a) the experimental results and (b) original EGP model results. . . . .	21
Figure 4.1	The fitted original Ree-Eyring equation (solid lines) to the experimental results (markers) for a strain of (a) 0.075 and (b) 0.3 and the fitted equation to determine the pressure dependency (solid lines) to the experimental results (markers) at 100°C for a strain of (c) 0.075 and (d) 0.3 in strain-rate dependency plots. . . . .	25
Figure 4.2	The evolution of the (a) activation volume, (b) activation energy, (c) rate constant and (d) pressure dependency, as characterized from the original Ree-Eyring equation (Equation 4.1) and the equation to determine the pressure dependency (Equation 4.2). . . . .	25
Figure 4.3	Visualisation of the behaviour of the constants for the Ree-Eyring parameters evolution in which $k = V, \Delta H$ or $\eta$ . . . . .	27
Figure 4.4	The difference between the EGP model results and the experimental results for (a, c) the benchmark and (b, d) the updated EGP model. This is shown at 20°C (a+b) and (c, d) 100°C. . . . .	28
Figure 4.5	The difference between the EGP model results and the experimental results for the EGP model with the Ree-Eyring parameters and shear moduli evolution. This is shown at (a) 20°C and (b) 100°C. . . . .	31

Figure 4.6	(a) The stress-strain curves created with the updated EGP model for the pre-yield regime plotted in black solid lines and the experimental stress-strain curves plotted with markers. (b) The equivalent plastic strain for the pre-yield regime. Both at 100°C. . . . .	32
Figure 4.7	The characterization of the activation volume, which is based on fitting the original Ree-Eyring equation to experimental results. . . . .	32
Figure 4.8	(a, c, e) The difference between the experimental results and the updated EGP model benchmark results. (b, d, f) The experimental stress-strain results plotted with markers and the updated EGP results plotted in solid lines. Both for a number of different strain-rates and at (a, b) 20°C, (c, d) 60°C and (e, f) 100°C. The grey lines in the plots with the difference are the exact difference including the noise from the experiments while the black lines are without the noise, which are obtained by filtering the grey lines with a Butterworth filter. . . . .	36
Figure 4.9	The strain-rate dependency of the updated EGP model results for the larger temperature and strain-rate range. . . . .	37
Figure 5.1	The stress-strain graph of a cyclic loading case with the updated EGP model as described in section 4.7 with a strain-rate of $10^{-3} \text{ s}^{-1}$ and at 100°C. . . . .	40
Figure 5.2	(a) The activation volume and cyclic stress-strain curves at (b) 20°C and (c) 100°C for 2 different proposals: $I_r$ is prevented from reducing (Non-reducing $I_r$ ) and $I_r$ in $\tanh()$ term is prevented from reducing (Non-reducing $\tanh(I_r)$ term). . . . .	40
Figure 5.3	"Constant strain-rate saw-tooth fully-reversed cyclic loading of PEEK in shear" with a strain-rate of $10^{-3} \text{ s}^{-1}$ and at 20°C, taken from Li et al. [2019]. . . . .	41
Figure 5.4	(a) The schematic influence of the viscous hardening stress, taken from Senden et al. [2010]. (b) The stress-strain graph of a cyclic loading case with the original and updated EGP model at 20°C and a strain-rate of $10^{-3} \text{ s}^{-1}$ . The $I_r$ in the $\tanh()$ term of the evolution of the Ree-Eyring parameters is prevented from reducing. The elastic strain hardening parameters are increased to $G_r = 7$ and $\alpha = 0.32$ for the original EGP model to create a useful visual representation of the elastic strain hardening behaviour. . . . .	42
Figure C.1	The original EGP model results and experimental results at 20°C and a strain rate of (a) $10^{-2}$ , (b) $10^{-3}$ , (c) $10^{-4}$ and (d) $10^{-5}$ . . . . .	71
Figure C.2	The original EGP model results and experimental results at 60°C and a strain rate of (a) $10^{-1}$ , (b) $10^{-2}$ , (c) $10^{-3}$ , (d) $10^{-4}$ and (e) $10^{-5}$ . . . . .	72
Figure C.3	The original EGP model results and experimental results at 100°C and a strain rate of (a) $10^{-1}$ , (b) $10^{-2}$ , (c) $10^{-3}$ , (d) $10^{-4}$ and (e) $10^{-5}$ . . . . .	73
Figure D.1	The updated EGP model results and experimental results at 20°C and a strain rate of (a) $10^{-2}$ , (b) $10^{-3}$ , (c) $10^{-4}$ and (d) $10^{-5}$ . . . . .	75
Figure D.2	The updated EGP model results and experimental results at 60°C and a strain rate of (a) $10^{-1}$ , (b) $10^{-2}$ , (c) $10^{-3}$ , (d) $10^{-4}$ and (e) $10^{-5}$ . . . . .	76
Figure D.3	The updated EGP model results and experimental results at 100°C and a strain rate of (a) $10^{-1}$ , (b) $10^{-2}$ , (c) $10^{-3}$ , (d) $10^{-4}$ and (e) $10^{-5}$ . . . . .	77

Figure F.1	The updated EGP model results for a large strain-rate range at $-20^{\circ}\text{C}$ . . . . .	83
Figure F.2	The updated EGP model results for a large strain-rate range at $20^{\circ}\text{C}$ . . . . .	83
Figure F.3	The updated EGP model results for a large strain-rate range at $60^{\circ}\text{C}$ . . . . .	84
Figure F.4	The updated EGP model results for a large strain-rate range at $100^{\circ}\text{C}$ . . . . .	84
Figure F.5	The updated EGP model results for a large strain-rate range at $140^{\circ}\text{C}$ . . . . .	84



## LIST OF TABLES

---

Table 3.1	The Carreau-Yassuda function fitting parameters. . . . .	17
Table 3.2	The time increments of the arc-length control method for different strain-rates. . . . .	19
Table 4.1	Used values for the evolution of the Ree-Eyring parameters in section 4.3. . . . .	29
Table 4.2	Used values for the evolution of the Ree-Eyring parameters and shear moduli in section 4.4. . . . .	30
Table 4.3	The characterized parameters for the updated EGP model. . .	34
Table 6.1	(a) The number of iterations and (b) run-time needed to reach a strain of 0.8 at 60°C for the original EGP model. The results are shown for a fixed step-size using either the original or updated linearization and using either the Modified Newton-Raphson (MNR) or Full Newton-Raphson (FNR) iteration scheme. . . . .	53
Table 6.2	(a) The number of iterations and (b) run-time needed to reach a strain of 0.8 at 60°C for the original EGP model. The results are shown for a variable step-size using either the original or updated linearization and using either the Modified Newton-Raphson (MNR) or Full Newton-Raphson (FNR) iteration scheme. . . . .	53
Table 6.3	(a) The number of iterations and (b) run-time needed to reach a strain of 0.8 at 60°C for the updated EGP model. The results are shown for a small variable step-size using either the original or updated linearization and using either the Modified Newton-Raphson (MNR) or Full Newton-Raphson (FNR) iteration scheme. . . . .	54
Table 6.4	(a) The number of iterations and (b) run-time needed to reach a strain of 0.8 at 60°C for the updated EGP model. The results are shown for a large variable step-size using either the original or updated linearization and using either the Modified Newton-Raphson (MNR) or Full Newton-Raphson (FNR) iteration scheme. . . . .	54
Table A.1	All parameters of the original EGP model. For each parameter; it's name, equations it was used in, and influence on the model is given. . . . .	65
Table B.1	The general parameters of the original EGP model. . . . .	69
Table B.2	The modal parameters for the $\alpha$ -process of the original EGP model. . . . .	70
Table B.3	The modal parameters for the $\beta$ -process of the original EGP model. . . . .	70



# NOMENCLATURE

---

## ACRONYMS

EGP	Eindhoven Glassy polymer
FNR	Full Newton-Raphson
MNR	Modified Newton-Raphson
PC	Polycarbonate
PEEK	Poly(ether-ether-ketone)
PMMA	Poly(methyl methacrylate)
PPO	Poly(p-phenylene oxide)
PS	Polystyrene

## VARIANTS OF SYMBOLS

$\tilde{X}$	Isochoric variant of a parameter $X$
$\dot{X}$	Time derivative of a parameter $X$
$X_x$	Parameter $X$ is different for each process
$X_\alpha$	$\alpha$ -process variant of parameter $X$
$X_\beta$	$\beta$ -process variant of parameter $X$
$X_{x,i}$	Modal variant of parameter $X$
$X_{\alpha,j}$	Modal variant for the $\alpha$ -process of parameter $X$
$X_{\beta,k}$	Modal variant for the $\beta$ -process of parameter $X$
$X^d$	Deviatoric variant of a parameter $X$
$X_e$	Elastic variant of a parameter $X$
$X_p$	Plastic variant of a parameter $X$
$X_{exp}$	Experimental results of a parameter $X$
$X_{EGP}$	EGP model results of a parameter $X$

## GREEK SYMBOLS

$\alpha$	Parameter for characterizing the pressure dependency
$\alpha_r$	The (limited) extensibility of the network of molecular chains in polymers
$\bar{\gamma}$	equivalent strain
$\dot{\gamma}_0$	pre-exponential factor
$\dot{\gamma}_{eq}$	Parameter for characterizing the pressure dependency
$\Gamma$	Shear modulus divided by viscosity
$\sigma$	True stress
$\sigma_d$	Deviatoric stress
$\sigma_h$	Hydrostatic stress
$\sigma_r$	Hardening stress
$\sigma_s$	Deriving stress
$\epsilon$	True strain
$\dot{\epsilon}$	Strain-rate
$\dot{\epsilon}_0$	Rate constant
$\eta$	Viscosity
$\eta_0$	Initial viscosity
$\eta_{const}$	Constant/basis initial viscosity
$\kappa$	Bulk modulus
$\lambda$	Plasticity parameter

(Continued on the next page)

$\mu$	Pressure dependency
$\zeta_r$	Mobility of the entanglements of the molecular chains in polymers
$\bar{\tau}$	Total equivalent stress
$\tau_0$	Characteristic shear stress
$\tau_{eq}$	Parameter for characterizing the pressure dependency
$\Phi$	System of equations for iterative stress calculation
$\Omega$	Rate of rotation

## LATIN SYMBOLS

${}^4\mathbf{A}^{(2)}$	Tensor function which is used in the stress and stiffness calculation
$\mathbf{B}$	Left Cauchy-Green deformation tensor
${}^4\mathbf{B}$	Tensor function which is used in the stiffness calculation
$C_1$	Evolution of initial viscosity in the original EGP model
$C_2$	Evolution of activation energy in the original EGP model
$C_{\Delta H,1}$	Initial decrease of the activation energy
$C_{\Delta H,2}$	Influence length of the initial decrease of the activation energy
$C_{\Delta H,3}$	Horizontal shift of the initial decrease of the activation energy
$C_{\Delta H,4}$	Large strain evolution of the activation energy
$C_{G,1}$	Initial decrease of the shear moduli
$C_{G,2}$	Influence length of the initial decrease of the shear moduli
$C_{G,3}$	Horizontal shift of the initial decrease of the shear moduli
$C_{\eta,1}$	Initial decrease of the initial viscosities
$C_{\eta,2}$	Influence length of the initial decrease of the initial viscosities
$C_{\eta,3}$	Horizontal shift of the initial decrease of the initial viscosities
$C_{\eta,4}$	Large strain evolution of the initial viscosities
$C_{V,1}$	Initial decrease of the activation volume
$C_{V,2}$	Influence length of the initial decrease of the activation volume
$C_{V,3}$	Horizontal shift of the initial decrease of the activation volume
$C_{V,4}$	Large strain evolution of the activation volume
$\mathbf{C}$	Right Cauchy-Green deformation tensor
$\mathbf{D}$	Rate of deformation
$E_{\Delta H}$	Function used for the derivative of the activation energy evolution
$E_G$	Function used for the derivative of the shear moduli evolution
$E_{\eta}$	Function used for the derivative of the initial viscosities evolution
$E_V$	Function used for the derivative of the activation volume evolution
$\mathbf{F}$	Deformation gradient
${}^4\mathbf{F}$	Tensor function which is used in the stiffness calculation
$G$	Shear modulus
$G_{const}$	Constant/basis shear modulus
$G_r$	Strain hardening modulus
$\Delta H$	Activation energy
$\Delta H_0$	Initial activation energy
$\Delta H_{const}$	Constant/basis activation energy
$I_r$	Invariant function
$I_{r,non}$	Non-reducing invariant function
$I_1$	First invariant
$I_2$	Second invariant
$\mathbf{I}$	Second order unit tensor
${}^4\mathbf{I}$	Fourth order unit tensor
$J$	Volume change ratio
$k_b$	Boltzmann's constant
${}^4\mathbf{K}_{tot}$	Total stiffness tensor
$\mathbf{L}$	Velocity gradient
$M$	Scalar function used within the derivative of the viscosity function

(Continued on the next page)

$M$	Tensor function used within the derivative of the driving stress with respect to the plasticity parameter
$N_e$	Number of density entanglements
$p$	Pressure
$r_0$	Fitting parameter of the modified Carreau-Yassuda function
$r_1$	Fitting parameter of the modified Carreau-Yassuda function
$r_2$	Fitting parameter of the modified Carreau-Yassuda function
$R$	Gas constant
$R_\gamma$	Intrinsic strain softening function
$S$	State parameter
${}^4S$	Stiffness tensor
${}^4S_h$	Hydrostatic stiffness tensor
${}^4S_r$	Hardening stiffness tensor
${}^4S_d$	Deviatoric stiffness tensor
${}^4S_x$	State variable stiffness tensor
$S_a$	ageing parameter
$S_H$	Parameter related to the ageing of the activation energy
$S_S$	Parameter related to ageing due to material changes
$\Delta t$	Time step used in iterative calculations
$T$	Temperature
$T_{base}$	Temperature at which the modal parameters are characterized
$T_g$	Glass transition zone
$V$	Activation volume
$V^*$	Activation volume from the original Ree-Eyring equation
$V_{const}$	Constant/basis activation volume



## INTRODUCTION

---

This thesis sets out to solve a problem with a viscoplastic model that is used for modelling polymers, this model is the Eindhoven Glassy Polymer (EGP) model. The problem arises when modelling the polymer Poly(ether-ether-ketone) (PEEK).

**PROBLEM DEFINITION** The project ‘SafeRIDE’ aims to determine the long-term performance of fibre-reinforced thermoplastic composites. The investigated fibre reinforced thermoplastic is made up of PEEK and carbon fibres. The University of Twente performed experimental uniaxial compression tests of Poly(ether-ether-ketone) (PEEK), and the TU Delft made numerical calculations with the EGP model. Two discrepancies were found between the experimental tests and the numerical model: *A lower yield stress at lower temperatures and a lower strain-rate dependency at the low and moderate strain range is observed in the numerical model in comparison with the uniaxial compression tests.*

**GOAL** The goal of this thesis is to obtain a better fit of the EGP model to the experimental observations of PEEK by updating the EGP model and/or its characterization.

**RESEARCH QUESTION** The problem definition and goal lead to the research question, which is as follows:

*How can the **Eindhoven Glassy Polymer model** be adapted to correspond **better** to the higher experimentally observed **strain-rate dependency** and higher experimentally observed **yield stress** at lower temperatures for **uniaxial compression tests** of **Poly(ether-ether-ketone)**?*

**SCOPE** The following limits are set to limit the scope of this thesis:

- Only the EGP model is used for modelling the polymer behaviour;
- Only the behaviour of the polymer PEEK is investigated;
- The research is conducted in 3D, but with uniaxial loading;
- The uniaxial compression loading case is investigated quantitatively and cyclic loading cases is investigated qualitatively;
- A strain-rate range of  $10^{-5} \text{ s}^{-1}$  to  $10^{-1} \text{ s}^{-1}$  is investigated quantitatively and a larger range of  $10^{-7} \text{ s}^{-1}$  to  $10^1 \text{ s}^{-1}$  is investigated qualitatively;
- A range of temperatures up to the glass transition temperature of PEEK ( $143^\circ\text{C}$ ) is considered.

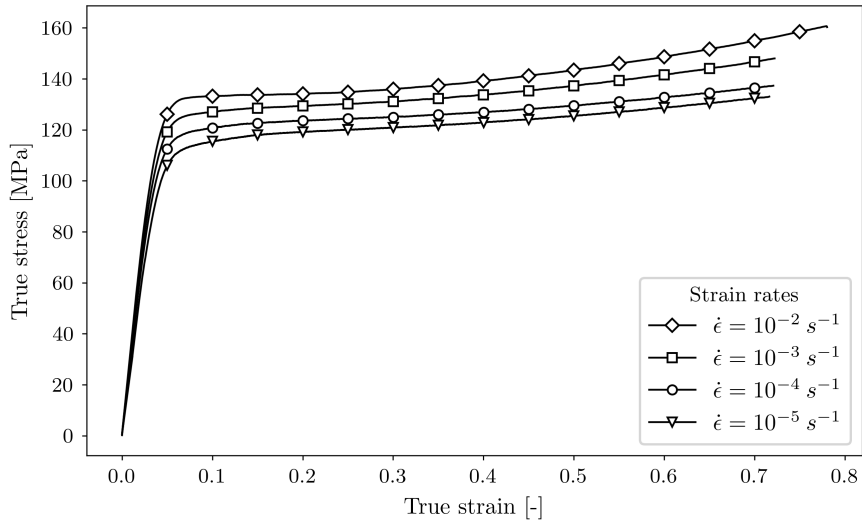
## 1.1 EXPERIMENTAL RESULTS

Uniaxial compression tests of PEEK are conducted by [Sundararajan and Govaert \[2021\]](#). This has been done for a range of strain-rates from  $10^{-5} \text{ s}^{-1}$  to  $10^{-1} \text{ s}^{-1}$  and temperatures of  $20^\circ\text{C}$ ,  $60^\circ\text{C}$  and  $100^\circ\text{C}$ . The stress-strain results of these experimental tests can be seen in [Figure 1.1](#). These experimental results will be considered accurate and representative for this thesis. The target for the EGP model is to reproduce these measurements as accurately as possible with two remarks. Firstly, adiabatic heating has influenced the stress-strain behaviour of the experimental tests with a high strain-rate of  $10^{-1} \text{ s}^{-1}$ , thus these experimental results are not used within this thesis and are dashed in [Figure 1.1](#). Secondly, stresses at strains higher than 0.5 are not fully reliable since the lubrication of the samples and in-homogeneous deformation play a role in the stress-strain behaviour.

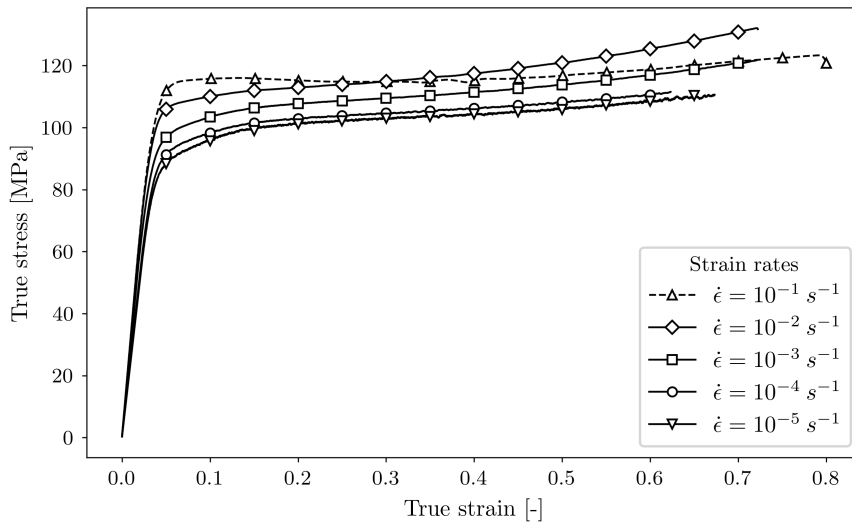
## 1.2 THESIS OUTLINE

The overall structure of this thesis takes the form of seven chapters. An important split exists between the **original** EGP model and the **updated** EGP model. The original EGP model is as described in the literature, while the updated EGP model is changed according to the work within this thesis.

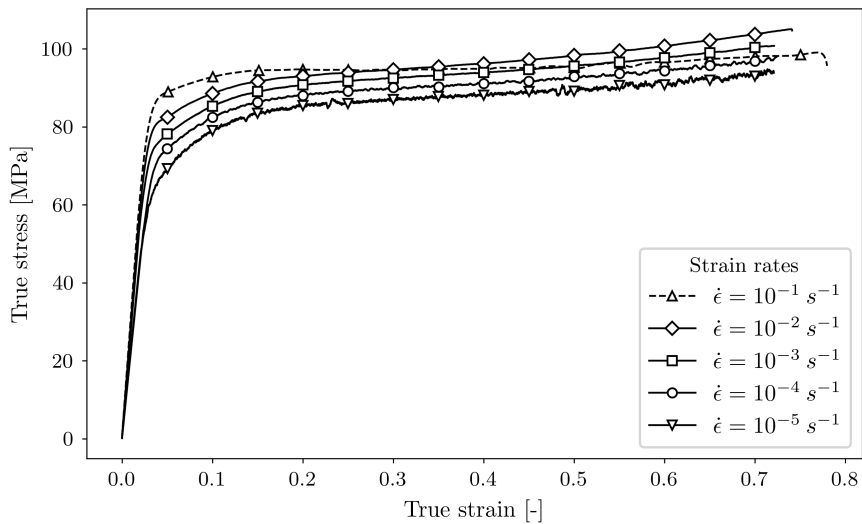
Two important subjects for this thesis are the deformation behaviour of polymers and the setup of the original EGP model. These subjects are explored in [chapter 2](#). The original EGP model is then characterized in [chapter 3](#) for two important reasons. Firstly, to confirm the claim of discrepancies between the experimental tests and the EGP model as noted in the problem definition above. Secondly, to create the basis for a benchmark. This benchmark is used to test results and check if these are improvements. Both reasons are also expanded upon in [chapter 3](#). [Chapter 4](#) draws together the key findings for the uniaxial compression case. Since the problem statement mentions long term performance testing in which cyclic loading cases for fatigue are of importance, a cyclic loading case is also investigated qualitatively in [chapter 5](#). [Chapters 4](#) and [5](#) lead together to the fully updated EGP model in [section 5.3](#), which then leads to a updated linearization of the stiffness tensor that is given in [chapter 6](#). The findings of this thesis are concluded and extensively discussed in [chapter 7](#), which lastly yields several recommendations.



(a)



(b)



(c)

Figure 1.1: The stress-strain curves of experimental uniaxial compression tests of PEEK conducted by the University of Twente at (a) 20°C, (b) 60°C and (c) 100°C.



## LITERATURE REVIEW

---

This chapter reviews the literature of two important subjects for this thesis. The first subject is the behaviour of polymers (section 2.1), which is important since this thesis is focused on the polymer PEEK. The second subject is the setup of the original EGP model (section 2.2), which is important since the EGP model will be used to model PEEK.

### 2.1 DEFORMATION BEHAVIOUR OF POLYMERS

**TEMPERATURE DEPENDENCY** The temperature has a large influence on the molecular structure of polymers, whereas the behaviour of polymers is very dependent on its molecular structure. The molecular structure of a polymer can be in three different states, based on a range of temperatures called the glass transition  $T_g$  zone [Roylance, 2001]:

- Glassy ( $T < T_g$ ): There is a stiff and brittle response.
- Leathery ( $T \approx T_g$ ): There is a leathery response (largely viscoelastic behaviour).
- Rubbery ( $T > T_g$ ): There is a large rubbery and fully reversible strain response.

**CRYSTALLINITY** A polymer is made up of long chains of molecules and can be categorised as amorphous, crystalline or semi-crystalline. In amorphous polymers, these chains are scattered randomly like cooked spaghetti. In crystalline polymers, the chains are structured as lamellae which are orderly and tightly packed and folded into a mostly planar zigzag and helical configuration. Semi-crystalline polymers have both amorphous and crystalline segments in which the degree of crystalline segments relative to amorphous segments is defined as the crystallinity. The crystallinity of semi-crystalline polymers differs between types of polymers and increases with temperature [Bower, 2003].

**STRESS-STRAIN BEHAVIOUR** The stress-strain curve of semi-crystalline polymers has the characteristics as seen in Figure 2.1. At the start of loading, this material behaves linear viscoelastic and develops to behave nonlinear viscoelastic [Clarijs, 2017] due to the elongation of the amorphous segments [Barba et al., 2020]. At a certain point, irreversible plastic flow leads to the yield point. The plastic flow occurs due to tilting of lamellar chains and the separation of crystalline segments. This leads to strain softening after the yield point since the previously locked amorphous chains are released. This effect is more pronounced in polymers with a higher crystallinity (for example, due to a lower temperature) and leads to higher yield stresses [Bower, 2003]. At higher strains, the amorphous molecular chains and crystalline segments are oriented parallel to the load which leads to strain hardening [Barba et al., 2020].

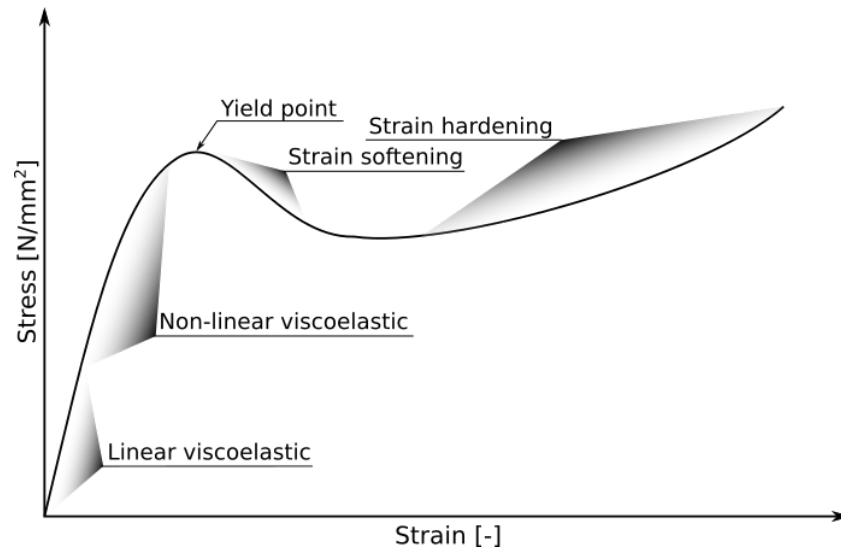


Figure 2.1: Schematic and annotated stress-strain behaviour of a polymer.

The strain hardening process already starts at the onset of loading but overtakes the other molecular processes at larger strains [Senden, 2009].

Polymers are strongly dependent on the strain-rate and temperature. When an experiment with a higher strain-rate is performed, a higher yield stress is obtained, while higher temperatures lead to lower yield stresses [Clarijs, 2017].

Some polymers are thermorheologically simple, but most are thermorheologically complex [Klompén and Govaert, 1999]. Thermorheologically simple polymers are influenced by only one relaxation process, while thermorheologically complex polymers are influenced by multiple relaxation processes [Senden, 2009]. Relaxation is defined as a time-dependent decrease of stress under a constant strain. A second (or higher) relaxation process influences the stress-strain behaviour, temperature dependency and strain-rate dependency of polymers. This happens below certain temperatures and above certain strain-rates. A change in the slope of the stress at a certain strain plotted against the strain-rate in a semilog plot (as seen in Figure 2.2a) indicates the presence of multiple relaxation processes. The slope of the curves in Figure 2.2a is from here on called the strain-rate dependency. An important observation is that the strain-rate dependency of different relaxation processes is additive [Klompén and Govaert, 1999].

**POLYMER AGEING** The ageing of a polymer influences its behaviour. This age represents the time, stress and temperature history of a polymer object. Polymers will have a higher yield stress and a stronger strain softening effect at a higher age [Clarijs, 2017]. Figure 2.2b demonstrates that the yield behaviour changes when samples have been annealed at different temperatures.

**THE BAUSCHINGER EFFECT** The Bauschinger effect is another substantial effect that influences the stress-strain behaviour of polymers and is related to the stress history of a material. A standard example of the Bauschinger effect is that the elastic limit is higher for subsequent loading in the same direction after uniaxial plastic straining when compared to loading in the reverse direction [Bauschinger, 1881]. Another example is the very different yield behaviour of polymers when the molecular chains are pre-oriented in any direction [Senden, 2009]. This means that the behaviour of material changes due to a (previous) stress state within the material. This is relevant for the cyclic loading cases that are qualitatively investigated within this thesis.

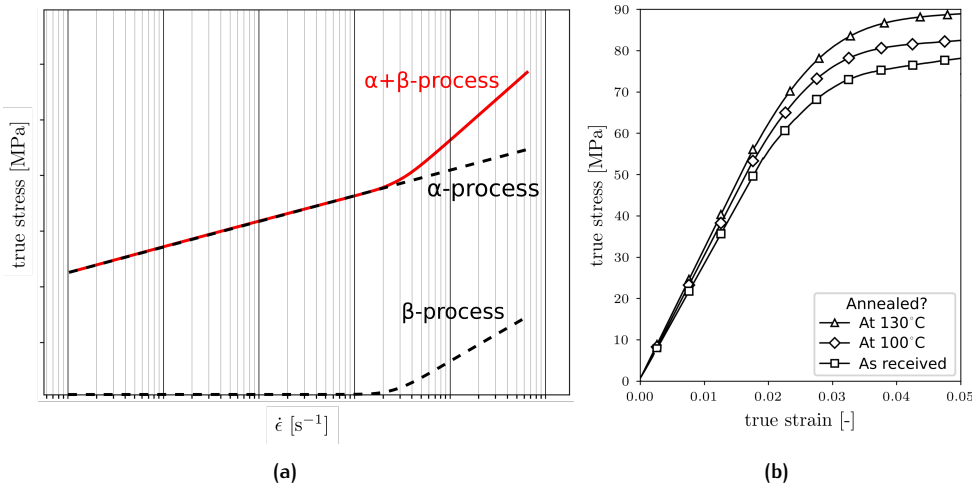


Figure 2.2: Schematic influence of (a) different relaxation processes on the strain-rate dependency and (b) ageing at different temperatures on stress-strain results.

**POLY(ETHER-ETHER-KETONE)** PEEK is a high-grade semi-crystalline polymer. Its full scientific name is poly(oxy-1,4-phenylene-oxy-1,4-phenylenecarbonyl-1,4-phenylene). PEEK has a high glass transition zone  $T_g$  around approximately 143°C, is largely crystalline and can be easily processed by melting [Rae et al., 2007]. The material is thermorheologically complex with multiple relaxation processes governing the deformation kinetics. Most literature sources attribute two relaxation processes to PEEK [El-Qoubaa and Othman, 2015; Klompen and Govaert, 1999], but three relaxation processes for very high strain-rates is also argued [El-Qoubaa and Othman, 2015; Safari et al., 2013]. The first process is associated with the relaxation of the amorphous segment of the material. The second process is associated with the chain mobility (glass transition) of the amorphous segment of the material [Senden, 2009].

## 2.2 GENERAL OVERVIEW OF THE EGP MODEL

The Eindhoven glassy polymer (EGP) model is a constitutive model based on the work of Haward and Thackray [1968]. They proposed that the post-yield behaviour of glassy polymers consists of a rate-dependent plastic flow process and a rate-independent contribution of the entanglement network. This work is one-dimensional and has been expanded to 3D by Boyce et al. [1989] as the 'BPA-model'. The development of the EGP model started around the mid-nineties by Tervoort et al. [1996] and is still expanding. This thesis will expand on the most recent (2021) implementation of the EGP model by the computational mechanics group at TU Delft, which is also described by Clarijs [2017].

The model can be schematized as seen in Figure 2.3. The total Cauchy stress tensor  $\sigma$  is decomposed into the hydrostatic stress  $\sigma_h$  and deviatoric stress  $\sigma_d$ . The deviatoric stress is then decomposed into an elasto-viscoplastic driving stress  $\sigma_s$  and an elastic hardening stress  $\sigma_r$  (Equation 2.1). This stress decomposition is one of the key characteristics of the model:

$$\sigma = \sigma_h + \sigma_s + \sigma_r \quad (2.1)$$

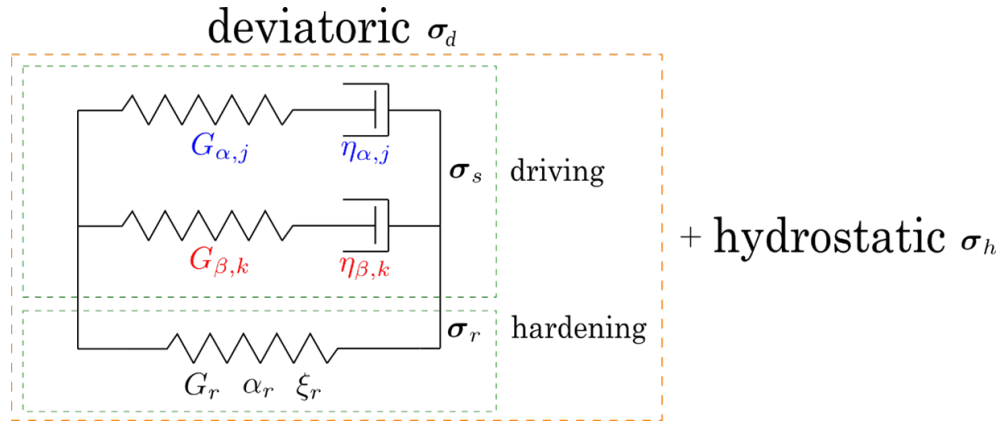


Figure 2.3: Schematisation of the EGP model stress decomposition.

### 2.2.1 Kinematics

A few kinematic relations, based on the theory of continuum mechanics, are defined to get a better overview of the EGP model.

Another key characteristic of the EGP model is the multiplicative decomposition of the deformation gradient in the elastic and plastic part:

$$\mathbf{F} = \mathbf{F}_e \cdot \mathbf{F}_p \quad (2.2)$$

The plastic part indicates deformation of the relaxed stress free configuration. This state would instantly be recovered when the stress would be removed [Govaert et al., 2000]. The multiplicative decomposition of the deformation gradient has two implications. First, the following holds for the velocity gradient tensor  $\mathbf{L}$ :

$$\begin{aligned} \mathbf{L} &= \dot{\mathbf{F}} \cdot \mathbf{F}^{-1} \\ &= \dot{\mathbf{F}}_e \cdot \mathbf{F}_e^{-1} + \mathbf{F}_e \cdot \dot{\mathbf{F}}_p \cdot \mathbf{F}_p^{-1} \cdot \mathbf{F}_e^{-1} \\ &= \mathbf{L}_e + \mathbf{L}_p \end{aligned} \quad (2.3)$$

The velocity gradient tensor  $\mathbf{L}$  can be written as an additive split in an elastic part  $\mathbf{L}_e$  and a plastic part  $\mathbf{L}_p$ .

Secondly, the multiplicative decomposition of the deformation gradient is not unique because no plastic rotation is specified. To solve this problem, it is assumed that the plastic deformation is spin free [Boyce et al., 1989]:

$$\mathbf{L}_p = \mathbf{D}_p + \mathbf{\Omega}_p = \mathbf{D}_p \quad (2.4)$$

$\mathbf{D}_p$  denotes the plastic rate of deformation and  $\mathbf{\Omega}_p$  denotes the plastic rate of rotation. Another assumption is that the plastic deformation is incompressible (isochoric), thus all volumetric changes due to loading are elastic. The volume change ratio  $J$  can then be written as:

$$J = \det(\mathbf{F}_e) \quad (2.5)$$

Volumetric deformations are described using the isochoric deformation gradient  $\tilde{\mathbf{F}}$ :

$$\tilde{\mathbf{F}} = J^{-\frac{1}{3}} \mathbf{F} \quad (2.6)$$

The same can be done for the elastic isochoric deformation  $\tilde{\mathbf{F}}_e$ . The time derivative of the elastic isochoric Cauchy-Green deformation tensor ( $\tilde{\mathbf{B}}_e = \tilde{\mathbf{F}}_e \cdot \tilde{\mathbf{F}}_e^T$ ) is used to compute elastic strain changes:

$$\dot{\tilde{\mathbf{B}}}_e = (\tilde{\mathbf{L}}^d - \mathbf{D}_p) \cdot \tilde{\mathbf{B}}_e + \tilde{\mathbf{B}}_e \cdot (\tilde{\mathbf{L}}^d - \mathbf{D}_p)^T \quad (2.7)$$

Equation 2.7 shows that  $\dot{\tilde{\mathbf{B}}}_e$  is reduced by the plastic rate of the deformation tensor  $\mathbf{D}_p$ .  $\mathbf{D}_p$  can be computed with a constitutive description based on the viscosity function which is described in subsection 2.2.3 [Clarijs, 2017].

### 2.2.2 Hydrostatic stress

The hydrostatic stress is computed quite straightforward and is based on the constant bulk modulus  $\kappa$ , the volume change ratio  $J$  and the second order unit tensor  $I$  [Tervoort et al., 1994]:

$$\sigma_h = \kappa(J - 1)I \quad (2.8)$$

The hydrostatic stress is shown as a separate component in Figure 2.3 since it is directly dependent on the (elastic) deformation gradient instead of being dependent on the left Cauchy-Green deformation tensor, which defines the other two stress components. Therefore in the mechanical analogue, the hydrostatic stress is not placed in parallel with the driving and hardening stress component.

### 2.2.3 Driving stress

Thermorheologically complex polymers are characterized by multiple relaxation processes. PEEK is a thermorheologically complex polymer of which two relaxation processes are modelled, denoted as  $\alpha$  and  $\beta$ . Within the EGP model, both these relaxation processes consist of a spectrum of relaxation times to correctly model the yield behaviour. This can be schematized as several parallel (Thus, additive) spring-dashpot systems (Leonov modes). These are called modes from here on and denoted by subscripts  $j$  and  $k$  for the  $\alpha$ - and  $\beta$ -process, respectively. In Figure 2.3, the  $\alpha$ - and  $\beta$ -process schematically consist of summations of  $j$  and  $k$  number of modes. The main difference between modes and processes is that the relaxation kinetics are the same for all modes within a process but differ between processes [Clarijs, 2017]. The spring of each mode is characterized by a shear modulus  $G_{\alpha,j}/G_{\beta,k}$  and the relaxation time is included in the deviatoric part of the isochoric, elastic left Cauchy-Green deformation tensor  $\tilde{\mathbf{B}}_{e_{\alpha,j}}^d / \tilde{\mathbf{B}}_{e_{\beta,k}}^d$  related to the dashpot of a mode:

$$\begin{aligned} \sigma_s &= \sum_{j=1}^n \sigma_{\alpha,j} + \sum_{k=1}^n \sigma_{\beta,k} \\ &= \sum_{j=1}^n G_{\alpha,j} \tilde{\mathbf{B}}_{e_{\alpha,j}}^d + \sum_{k=1}^n G_{\beta,k} \tilde{\mathbf{B}}_{e_{\beta,k}}^d \end{aligned} \quad (2.9)$$

The deviatoric part of the modal isochoric, elastic left Cauchy-Green deformation tensor is computed by:

$$\begin{aligned} \tilde{\mathbf{B}}_{e_{x,i}}^d &= \left( \tilde{\mathbf{F}}_{e_{x,i}} \cdot \tilde{\mathbf{F}}_{e_{x,i}}^T \right)^d \\ &= J^{-\frac{2}{3}} \left( \mathbf{F}_{e_{x,i}} \cdot \mathbf{F}_{e_{x,i}}^T \right)^d \end{aligned} \quad (2.10)$$

Where  $x = \alpha$  or  $\beta$  and  $i = j$  or  $k$ . This shows that Equation 2.7 is used in its modal form and is computed for each mode separately.

**THE VISCOSITY FUNCTION** The plastic rate of deformation  $D_p$  is used to reduce the accumulation of isochoric elastic strain, as seen in Equation 2.7. The following Non-Newtonian flow rule is used to describe the plastic rate of deformation gradient with the driving stress:

$$D_{p_{x,i}} = \frac{\sigma_{x,i}}{2\eta_{x,i}} \quad (2.11)$$

Where  $\eta_{x,i}$  is the scalar viscosity function and is based on Ree-Eyring flow theory. This theory uses a semi-empirical relation for viscosity based on the relaxation process of viscous flow. This can be visualized as "the sudden shifting of some small patch on one side of a shear surface with respect to the neighboring material on

the other side of the shear surface" [Ree and Eyring, 1955]. These shear surfaces are, in the case of semi-crystalline polymers, the different (amorphous/crystalline) segments [Tervoort et al., 1996].

The viscosity function in the original EGP model is dependent on temperature, strain-rate and pressure. The strain-rate dependency is based on an equivalent stress proportional to the Von Mises stress [Tervoort et al., 1997]. The viscosity function is also based on the rejuvenated state (a state where no ageing has occurred [Van Breemen et al., 2011]). The viscosity function as used in the original EGP model is as follows:

$$\eta_{x,i} = \underbrace{\eta_{0,x,i} \frac{\bar{\tau}_x / \tau_{0,x}}{\sinh(\bar{\tau}_x / \tau_{0,x})}}_{\text{Part 1}} \exp\left(\frac{\Delta H_x}{RT}\right) \underbrace{\exp\left(\frac{\mu_x p}{\tau_{0,x}}\right) \exp(S_x)}_{\text{Part 2}} \quad (2.12)$$

In which part 1 originates from the original Ree-Eyring formulation and part 2 originates from EGP development. The following parameters are used within the viscosity function for process  $x = \alpha$  or  $\beta$  and for mode  $i = j$  or  $k$ :

- $\tau_{0,x}$  is the characteristic shear stress, defined as:

$$\tau_{0,x} = \frac{k_b T}{V_x} \quad (2.13)$$

- $T$  is the temperature;
- $V_x$  is the activation volume;
- $\Delta H_x$  is the activation energy;
- $\eta_{0,x,i}$  is the initial viscosity;
- $\mu_x$  is the pressure dependency;
- $S_x$  is the state parameter;
- $\bar{\tau}_x$  is the total equivalent stress, defined as:

$$\bar{\tau}_x = \sqrt{\frac{1}{2} \boldsymbol{\sigma}_x : \boldsymbol{\sigma}_x} \quad (2.14)$$

- $p$  is the pressure, defined as:

$$p = -\kappa(J - 1) \quad (2.15)$$

- $\kappa$  is the bulk modulus (= 5475 N/mm<sup>2</sup> for PEEK);
- $k_b$  is the Boltzmann's constant (= 1.38064852 · 10<sup>-23</sup> m<sup>2</sup> kg s<sup>-2</sup> K<sup>-1</sup>);
- $R$  is the gas constant (= 8.3145 J mol<sup>-1</sup> K<sup>-1</sup>).

**THE STATE PARAMETER** The thermomechanical history of the material is taken into account with the scalar state parameter  $S_x$ . This defines the current thermomechanical state and the inherent strain-softening behaviour. The state parameter is a function of the equivalent plastic strain  $\bar{\gamma}_p$ :

$$S_x = S_x(\bar{\gamma}_p) = S_{a_x} R_{\gamma_x}(\bar{\gamma}_p) \quad (2.16)$$

The ageing parameter  $S_{a_x}$  determines and the height of the yield drop and the intrinsic strain softening function  $R_{\gamma_x}$  describes the shape of the yield drop.

By proposal of Senden et al. [2012a],  $S_{a_x}$  is split in a part related to material changes  $S_{S_x}$  and a part related to ageing of the activation energy  $S_{H_x}$ :

$$S_{a_x} = \frac{S_{H_x}}{RT} + S_{S_x} \quad (2.17)$$

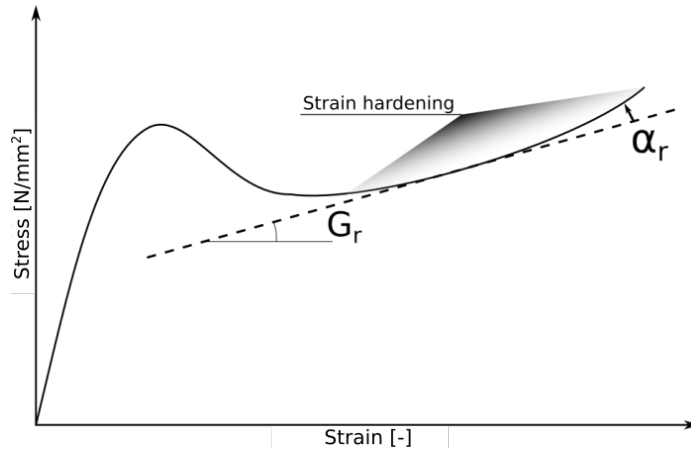


Figure 2.4: Schematic influence of the elastic strain hardening parameters on the hardening stress contribution.

A function for the activation energy is added to the EGP model to account for the ageing of this parameter:

$$\Delta H_x = \Delta H_{0_x} + S_{H_x} R_{\gamma_x}(\bar{\gamma}_p) \quad (2.18)$$

The equivalent plastic strain mentioned in Equation 2.16 is calculated with its rate and based on the mode with the highest viscosity. This mode indicates the onset of macroscopic yielding [Van Breemen et al., 2011]. It is assumed that the mode with the highest viscosity is the first  $\alpha$ -mode:

$$\dot{\bar{\gamma}}_p = \frac{\bar{\tau}_{\alpha,1}}{\eta_{\alpha,1}} \quad (2.19)$$

$\bar{\tau}_{\alpha,1}$  and  $\eta_{\alpha,1}$  can be determined with Equations 2.14 and 2.12, respectively.

The softening function  $R_{\gamma_x}$  is described by a modified Carreau-Yasuda function [Yasuda, 1979] as proposed by Klompen et al. [2005]:

$$R_{\gamma_x}(\bar{\gamma}_p) = \left[ \frac{1 + (r_{0_x} \exp(\bar{\gamma}_p))^{r_{1_x}}}{1 + r_{0_x}^{r_{1_x}}} \right]^{\frac{r_{2_x}-1}{r_{1_x}}} \quad (2.20)$$

In which  $r_{0_x}$ ,  $r_{1_x}$  and  $r_{2_x}$  are fitting parameters. It is assumed that these fitting parameters are the same for each mode within a process.

#### 2.2.4 Hardening stress

The strain hardening is a combined elastic-viscous occurrence as indicated by multiple studies [Kramer, 2005; Hoy and Robbins, 2008; Senden et al., 2010; Nayak et al., 2011]. Both nonlinear elastic strain hardening and viscous strain hardening are included in the EGP model. The nonlinear elastic strain hardening is shown as a spring in the schematisation of the EGP model in Figure 2.3 and the viscous strain hardening is incorporated in the viscosity function (Equation 2.12).

**ELASTIC STRAIN HARDENING** The elastic hardening stress can be schematised as a nonlinear spring characterized by the Edwards-Vilgis slip link model [Edwards and Vilgis, 1986]. This model is used due to its high accuracy and is defined as follows:

$$\sigma_r = \frac{G_r}{J} (\bar{\mathbf{B}} \cdot \mathbf{Z})^d \quad (2.21)$$

Tensor  $\mathbf{Z}$  is defined as:

$$\begin{aligned} \mathbf{Z} = & \frac{\alpha_r^2(1 + \zeta_r)(1 - \alpha_r^2)}{(1 - \alpha_r^2 \cdot \text{tr}(\tilde{\mathbf{B}}))^2} \text{tr}(\tilde{\mathbf{B}} \cdot (\mathbf{I} + \zeta_r \tilde{\mathbf{B}})^{-1}) \mathbf{I} \\ & + \frac{(1 + \zeta_r)(1 - \alpha_r^2)}{1 - \alpha_r^2 \cdot \text{tr}(\tilde{\mathbf{B}})} \left( (\mathbf{I} + \zeta_r \tilde{\mathbf{B}})^{-1} - \zeta_r (\mathbf{I} + \zeta_r \tilde{\mathbf{B}})^{-1} \cdot (\mathbf{I} + \zeta_r \tilde{\mathbf{B}})^{-1} \cdot \tilde{\mathbf{B}} \right) \\ & + \zeta_r (\mathbf{I} + \zeta_r \tilde{\mathbf{B}})^{-1} - \frac{\alpha_r^2}{1 - \alpha_r^2 \cdot \text{tr}(\tilde{\mathbf{B}})} \mathbf{I} \end{aligned} \quad (2.22)$$

In which:

- $G_r$  is the strain hardening modulus that is actually comprised of  $G_r = N_e k_B T$ . This function is temperature-dependent, but  $G_r$  is assumed constant in the EGP model. With:
  - $N_e$  is the number of density entanglements;
  - $k_b$  is the Boltzmann constant ( $= 1.38064852 \cdot 10^{-23} \text{ m}^2 \text{ kg s}^{-2} \text{ K}^{-1}$ );
  - $T$  is temperature;
- $\zeta_r$  is the mobility of the entanglements of the molecular chains in polymers. Since the entanglement network stays intact during plastic deformation, this parameter is kept at 0;
- $\alpha_r$  is the (limited) extensibility of the network of molecular chains in polymers.

Figure 2.4 shows the influence of  $G_r$  and  $\alpha_r$  on the elastic strain hardening stress contribution.  $G_r$  determines the slope of the linear curve of the elastic hardening behaviour and  $\alpha_r$  leads to nonlinear behaviour of this curve.

Taking  $\zeta_r = \alpha_r = 0$  reduces the expression to a Neo-Hookean strain hardening relation. This strain hardening relation was incorporated in earlier versions of the EGP model [Clarijs, 2017].

**VISCOUS HARDENING STRESS** Strain hardening has a viscous component by making the driving stress deformation dependent. This effect is in the EGP model incorporated in the viscosity function (Equation 2.12). Due to this, loading-unloading situations are described realistically because the Bauschinger effect (see section 2.1) is captured [Senden et al., 2010]. The deformation dependence of the model is described with the invariant function  $I_r(\tilde{\mathbf{B}})$ , which is approximately proportional to the strain:

$$I_r(\tilde{\mathbf{B}}) \underset{\sim}{\propto} \epsilon \quad (2.23)$$

$$I_r(\tilde{\mathbf{B}}) = \sqrt{\frac{1}{2} \tilde{\mathbf{B}}^d : \tilde{\mathbf{B}}^d} = \sqrt{\frac{1}{3} I_1^2 - I_2} \quad (2.24)$$

Where:

$$I_1 = \text{tr}(\tilde{\mathbf{B}}) \quad (2.25)$$

$$I_2 = \frac{1}{2} (\text{tr}^2(\tilde{\mathbf{B}}) - \text{tr}(\tilde{\mathbf{B}} \cdot \tilde{\mathbf{B}})) \quad (2.26)$$

Senden et al. [2012a] determined that the initial viscosity and activation energy should be deformation-dependent to model the Bauschinger effect in polycarbonate. These parameters are quadratically dependent on the invariant function for the  $\alpha$ -process and linearly dependent on the invariant function for the  $\beta$ -process. The initial viscosities are now determined as follows:

$$\eta_{0,\alpha,i}(I_r(\tilde{\mathbf{B}})) = \eta_{0,\alpha,i} \exp(C_{2,\alpha}(I_r(\tilde{\mathbf{B}}))^2) \quad (2.27)$$

$$\eta_{0_{\beta,i}}(I_r(\tilde{\mathbf{B}})) = \eta_{0_{\beta,i}} \exp(C_{2,\beta} I_r(\tilde{\mathbf{B}})) \quad (2.28)$$

The relation for the activation energy in Equation 2.18 is updated for the deformation dependency, such that:

$$\Delta H_{\alpha}(I_r(\tilde{\mathbf{B}})) = \Delta H_{0_{\alpha}} + C_{1,\alpha}(I_r(\tilde{\mathbf{B}}))^2 + S_{H_{\alpha}} R_{\gamma_{\alpha}}(\bar{\gamma}_p) \quad (2.29)$$

$$\Delta H_{\beta}(I_r(\tilde{\mathbf{B}})) = \Delta H_{0_{\beta}} + C_{1,\beta} I_r(\tilde{\mathbf{B}}) + S_{H_{\beta}} R_{\gamma_{\beta}}(\bar{\gamma}_p) \quad (2.30)$$



## BENCHMARK

---

In this chapter, the original EGP model is firstly characterized in section 3.1 for PEEK based on experimental data from the University of Twente [Sundrarajan and Govaert, 2021]. This experimental data was introduced and described in section 1.1. The characterization is performed for two important reasons. Firstly, to create a benchmark in sections 3.2 and 3.3 that can be used to compare results from the updated EGP model and check if these are improvements. The benchmark consists of stress-strain curves, difference plots and strain-rate dependency plots. Secondly, to confirm in section 3.4 the claim of discrepancies between the experimental tests and the EGP model as noted in the problem definition in chapter 1.

### 3.1 CHARACTERIZATION OF THE ORIGINAL EGP MODEL

Appendix A lists the included parameters, their names, their influence on the model and in what equation(s) within the literature review (chapter 2) they can be found. All parameters need to be characterized by taking the following steps:

1. Determine the activation volume by assuming other needed parameters and fitting the strain-rate dependency of the EGP model and the experimental results;
2. Determine the pressure dependency with the procedure outlined by Govaert et al. [2001];
3. Determine the elastic strain hardening and viscous strain hardening parameters;
4. Determine the modal parameters of the  $\alpha$ -process:
  - a) Determine the shear moduli and initial viscosities with the procedure outlined by Van Breemen et al. [2011];
  - b) Determine the state factor and softening shape by fitting the softening response of the experimental results;
5. Determine the activation energy of the  $\alpha$ -process by fitting experimental results at different temperatures. This is only necessary if more than one temperature is modelled;
6. Determine the modal parameters and the activation energy of the  $\beta$ -process in the same way as for the  $\alpha$ -process. This is only necessary if the  $\beta$ -process is present.

The steps correspond with the following paragraphs.

**STEP 1; DETERMINATION ACTIVATION VOLUME** The activation volume changes the strain-rate dependency of the EGP model. The strain-rate dependency can be observed as the slope of the curve in a semi-log plot of the stress against the strain-rate (Figure 2.2a). A constant value for the activation volume has been found by firstly taking representative parameters based on another characterization of the EGP model [Sundararajan and Govaert, 2021] and secondly fitting the strain-rate dependency with the activation volume at a strain of 0.3. The following constant values for the activation volume have been obtained for the  $\alpha$ - and  $\beta$ -process:  $V_\alpha = 9.20 \text{ nm}^3$  and  $V_\beta = 5.00 \text{ nm}^3$ .

**STEP 2; DETERMINATION PRESSURE DEPENDENCY** The pressure dependency  $\mu_x$  can be determined with the procedure outlined by Govaert et al. [2001]. However, this method did not yield constant values as later discussed in section 4.1. For the sake of the characterization, a constant value of 0.06 has been chosen for the pressure dependency. This value is based on an earlier characterization of another PEEK sample performed by the University of Twente [Sundararajan and Govaert, 2021] and leads to realistic stress-strain curves.

**STEP 3A; DETERMINATION ELASTIC STRAIN HARDENING PARAMETERS** The elastic strain hardening modulus  $G_r$ , the limited extensibility of the molecular network  $\alpha_r$  and the mobility of the entanglements of the molecular network  $\zeta_r$  are determined in this step. The large strain response of the EGP model is manually fitted to the experimental results by varying the elastic strain hardening parameters. An EGP analysis with only one  $\alpha$ -process mode and an assumed shear modulus and initial viscosity is used for this analysis.  $G_r$  determines the slope of the linear curve of the elastic hardening behaviour and  $\alpha_r$  leads to nonlinear behaviour of this curve as seen in Figure 2.4.  $\zeta_r$  is assumed 0 as described in subsection 2.2.4. Since the slope of the stress-strain curves increases at higher strains, it is assumed that a nonlinear hardening effect is present and  $\alpha_r$  is non-zero.

The described analysis led to a strain-hardening modulus  $G_r$  of 5.0 MPa and a  $\alpha_r$  of 0.22.

**STEP 3B; DETERMINATION VISCOUS STRAIN HARDENING PARAMETERS** The Viscous strain hardening parameters  $C_{1,\alpha}$ ,  $C_{2,\alpha}$ ,  $C_{1,\beta}$  and  $C_{1,\beta}$  lead to an evolution of the activation energy and initial viscosities. By correctly characterizing these parameters evolution, the viscous strain hardening can be modelled leading to correctly capturing the Bauschinger effect [Senden et al., 2012a] when performing cyclic loading. All four parameters are kept at 0 because this chapter focuses on a uniaxial compression loading case.

**STEP 4A; DETERMINATION SHEAR MODULI AND INITIAL VISCOSITIES  $\alpha$ -PROCESS** The procedure outlined in Van Breemen et al. [2011] is used to determine the shear moduli and initial viscosities for the Leonov modes that are used to represent the  $\alpha$ -relaxation process. The parameters needed to determine the shear moduli and initial viscosities have been determined in the previous sections. There should be no influence of the  $\beta$ -process on the parameters for the  $\alpha$ -process. Thus, A stress-strain result should be used where only the  $\alpha$ -process is present. Figure 3.1 shows the strain-rate dependency of the experiments, which can be observed as the slope of the curves in this semi-log plot of the stress against the strain-rate. The slope is less steep when only the  $\alpha$ -process is present instead of when both the  $\alpha$ - and  $\beta$ -process are present. There can then be seen in the figure that only the  $\alpha$ -process is present at  $100^\circ\text{C}$  and a strain-rate of  $10^{-3} \text{ s}^{-1}$ . Thus, the experimental stress-strain result for this temperature and strain-rate has been used.

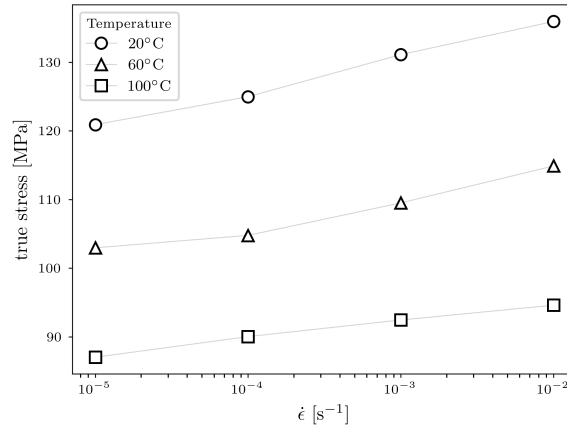


Figure 3.1: The strain-rate dependency of the experimental results (see section 1.1) at a strain of 0.4 shown as markers for different temperatures. The grey line is indicative for the slope.

Table 3.1: The Carreau-Yassuda function fitting parameters.

		$\alpha$ -process	$\beta$ -process
<b>Carreau-Yassuda fitting parameter 0</b>	$r_0$	0.965	0.965
<b>Carreau-Yassuda fitting parameter 1</b>	$r_1$	-5.0	-5.0
<b>Carreau-Yassuda fitting parameter 2</b>	$r_2$	-5.0	-5.0

Following, the determined initial viscosities are shifted to correct for the current thermodynamic state:

$$\eta_{0_{x,i}} = \eta_{0_{x,i,calc}} \exp(-S_x) \exp\left(\frac{-\Delta H_x}{RT_{x,base}}\right) \quad (3.1)$$

$T_{x,base}$  is the temperature that is used to characterize the modal parameters of a certain process. A  $T_{\alpha,base}$  of 100°C has been used within this step.

The resulting shear moduli and initial viscosities are listed in Table B.2 within appendix B. A high number of modes is used since the goal of this thesis is to obtain results that are as accurate as possible and more modes lead to more accurate results.

#### STEP 4B; DETERMINATION STATE FACTOR AND SOFTENING SHAPE $\alpha$ -PROCESS

The experimental results show a slight softening behaviour. This indicates that the state factor  $S_x$  should be low, but non-zero. After testing multiple state factors for shifting the initial viscosities (Equation 3.1), a state factor of 2.0 leads to the correct softening behaviour.  $S_{a_x}$  determines the height of the stress drop after the yield point and should be set equal to 2.0 as well.  $S_{a_x}$  is additively split in the ageing of the activation volume  $S_{H_x}$  and the ageing of the material  $S_{S_x}$  as seen in Equation 2.17. (Partly) contributing the softening behaviour to the ageing of the activation energy would lead to higher activation energy around the yield point, as can be seen in Equation 2.18. However, a higher activation volume around the yield point leads to less accurate results. Thus, the softening behaviour is fully contributed to the ageing of the material. This means that  $S_{H_x} = 0.0$  and  $S_{S_x} = 2.0$ .

The softening shape has been determined by assuming a higher state factor and then creating the correct shape with the modified Carreau-Yassuda function fitting parameters. The fitting parameters are shown in Table 3.1. It should be noted that the fitting parameters are not very exact due to the small softening shape of the experimental results. Thus, the fitting parameters should be used with care for experimental results of PEEK with a high state factor.

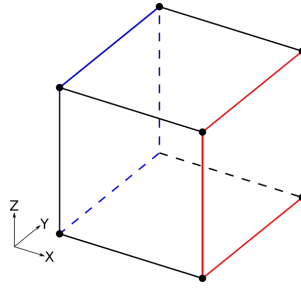


Figure 3.2: The simple 8-noded hexahedral finite element.

**STEP 5; DETERMINATION ACTIVATION ENERGY  $\alpha$ -PROCESS** The activation energy of the  $\alpha$ -process describes the temperature dependency of the  $\alpha$ -process. Therefore it should be fitted on stress-strain behaviour from two different temperatures where only the  $\alpha$ -process is present. It can be seen in Figure 3.1 that this is the case for a strain-rate of  $10^{-4}$  at  $60^\circ\text{C}$  and  $100^\circ\text{C}$  according to the explanation in step 4a.

A value of  $685 \cdot 10^3 \text{ J mol}^{-1}$  leads to the best fit.

**STEP 6; DETERMINATION PARAMETERS  $\beta$ -PROCESS** The fact that the curves in Figure 3.1 are bi-linear instead of linear shows that a  $\beta$ -process is present and should be characterized as well. The same steps as for the  $\alpha$ -process have been taken to determine the equivalent  $\beta$  parameters. However, the following changes are made:

- *Modal parameters:* Stress-strain curves from the  $\alpha$ -process at  $20^\circ\text{C}$  and a strain-rate of  $10^{-3} \text{ s}^{-1}$  are obtained with the EGP model and subtracted from the experimental stress-strain curves at the same temperature and strain-rate to find a curve that is used for the procedure. The obtained shear moduli and initial viscosities can be found in Table B.3 within appendix B. No softening is observed for the  $\beta$ -process, thus  $S_{H_\alpha} = S_{S_\alpha} = 0.0$ .
- *Activation energy:* The stress-strain curves of a strain-rate of  $10^{-2} \text{ s}^{-1}$  at  $20^\circ\text{C}$  and  $60^\circ\text{C}$  have been used to obtain the activation energy for the  $\beta$ -process. A value of  $90 \cdot 10^3 \text{ J mol}^{-1}$  leads to the best fit.

**CHARACTERIZATION OF THE BENCHMARK** All parameters that are needed for the original EGP model (Appendix A) have been determined in this section. The characterization of the benchmark is shown in appendix B.

### 3.2 EGP MODEL SETTINGS/FEM SETTINGS

The EGP model is implemented by the computational mechanics group from TU Delft in a FEM program written in C++ using the programming tool kit *Jive* from Dynaflo [Dynaflo Research Group, 2020].

A simple 8-noded hexahedral finite element with a  $2 \times 2 \times 2$  Gauss integration scheme has been used for all analyses in this thesis.

Figure 3.2 shows the constraints on the cube for a uniaxial compression test. All four nodes on the red face are restrained in the x-direction and the two nodes on the bottom of the red face are additionally restrained in the y-direction. The cube is loaded in the positive x-direction on the four nodes of the blue face until a prescribed strain of 0.8 is reached in the cube.

Load increments are applied by the arc-length control method with adaptive stepping and the modified Newton-Raphson iteration scheme. The arc-length control method uses a precision of  $10^{-6}$ . The starting, minimal and maximal values of time increments for the arc-length control method have been defined for the adaptive stepping method and are listed in Table 3.2 for the different strain-rates.

**Table 3.2:** The time increments of the arc-length control method for different strain-rates.

	$10^{-1}$	$10^{-2}$	$10^{-3}$	$10^{-4}$	$10^{-5}$
<b>Starting increment</b>	0.01	0.1	1.0	10	100
<b>Minimal increment</b>	0.001	0.01	0.1	1.0	10
<b>Maximal increment</b>	0.02	0.2	2.0	20	200

### 3.3 RESULTS OF THE BENCHMARK

**DIFFERENCES** The results of the benchmark consist of the differences between the original EGP model results and the experimental results and is shown in several figures, namely:

- Figures 3.3a, 3.3c and 3.3e with the difference between the original EGP model stress-strain results and the experimental stress-strain results;
- Figures 3.3b, 3.3d and 3.3f with the stress-strain curves of both the original EGP model and the experiments zoomed in to the after-yield stress levels;
- Figure 3.4 with the strain-rate dependency at different temperatures;
- Figure 3.5 comparing the qualitative stress-strain behaviour of the pre-yield regime of the original EGP model and the experiments.

The four types of figures visualizing the differences are described and analyzed in the four following paragraphs.

**DIFFERENCE PLOTS** The difference between the experimental stress-strain results and the original EGP model stress-strain results is plotted for all strain-rates at multiple fixed temperatures. These plots are the main method of checking the difference between the EGP model and the experiments. They are for the benchmark shown in Figures 3.3a, 3.3c and 3.3e at 20°C, 60°C and 100°C respectively. These figures can also be created for the updated EGP model and be compared to these figures to check if the updated EGP model is an improvement upon the benchmark. The curves should be as close to the red 0-line as possible, as this means that there is no difference between an EGP model result and an experimental result.

**STRESS-STRAIN CURVES** Stress-strain curves have been determined with the original EGP model at a combination of the temperatures 20°C, 60°C and 100°C and the strain-rates of  $10^{-1} \text{ s}^{-1}$ ,  $10^{-2} \text{ s}^{-1}$ ,  $10^{-3} \text{ s}^{-1}$ ,  $10^{-4} \text{ s}^{-1}$  and  $10^{-5} \text{ s}^{-1}$ . Stress-strain curves plotted against the experimental results that are zoomed in to the after-yield stress levels can be seen in Figures 3.3b, 3.3d and 3.3f for the specified temperatures. The full curves can be found in appendix C.

**STRAIN-RATE DEPENDENCY** The semi-log plot of the stress against the strain-rate shows the strain-rate dependency at a specific strain. The strain-rate dependency is defined as the slope of the curves in these plots. The strain-rate dependency of the experimental results and the original EGP model at a strain of 0.1 at 20°C, 60°C and 100°C are shown in 3.4.

It can be seen that the slope of the curves is different for the experimental and original EGP model results. This means that there is a different strain-rate dependency at this strain level. The same is seen at almost all other strain levels.

**PRE-YIELD BEHAVIOUR** Figure 3.5 shows that the stress-strain behaviour of the experiments in the pre-yield regime is not captured by the original EGP model. The results of the original EGP model are independent of the strain-rate, while the experimental results are not.

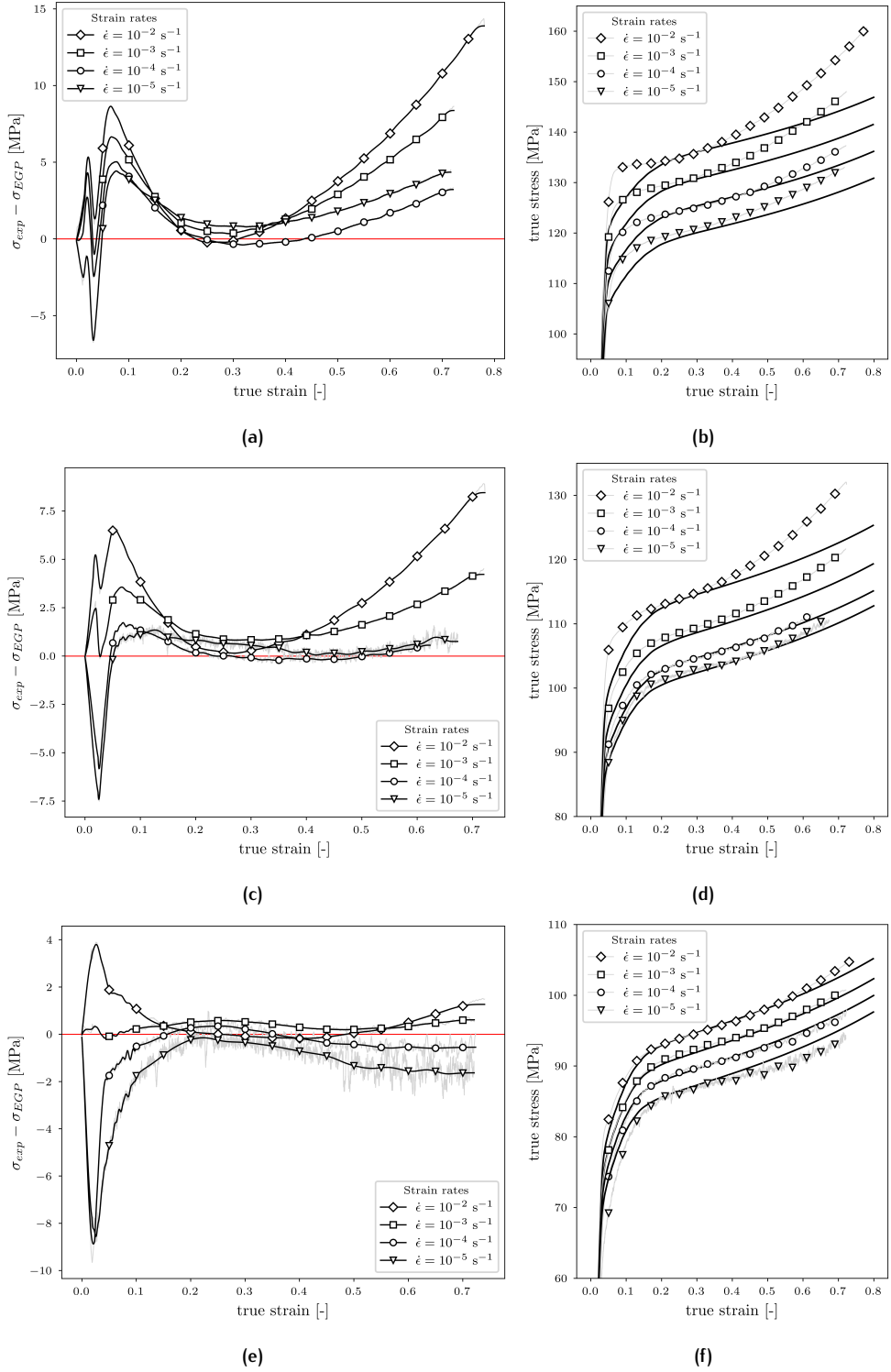


**Figure 3.3:** (a, c, e) The difference between the experimental results and the original EGP model benchmark results. (b, d, f) The experimental stress-strain results plotted with markers and the original EGP results plotted in solid lines. Both for a number of different strain-rates and at (a, b) 20°C, (c, d) 60°C and (e, f) 100°C. The grey lines in the plots with the difference are the exact difference including the noise from the experiments while the black lines are without the noise, which are obtained by filtering the grey lines with a Butterworth filter.

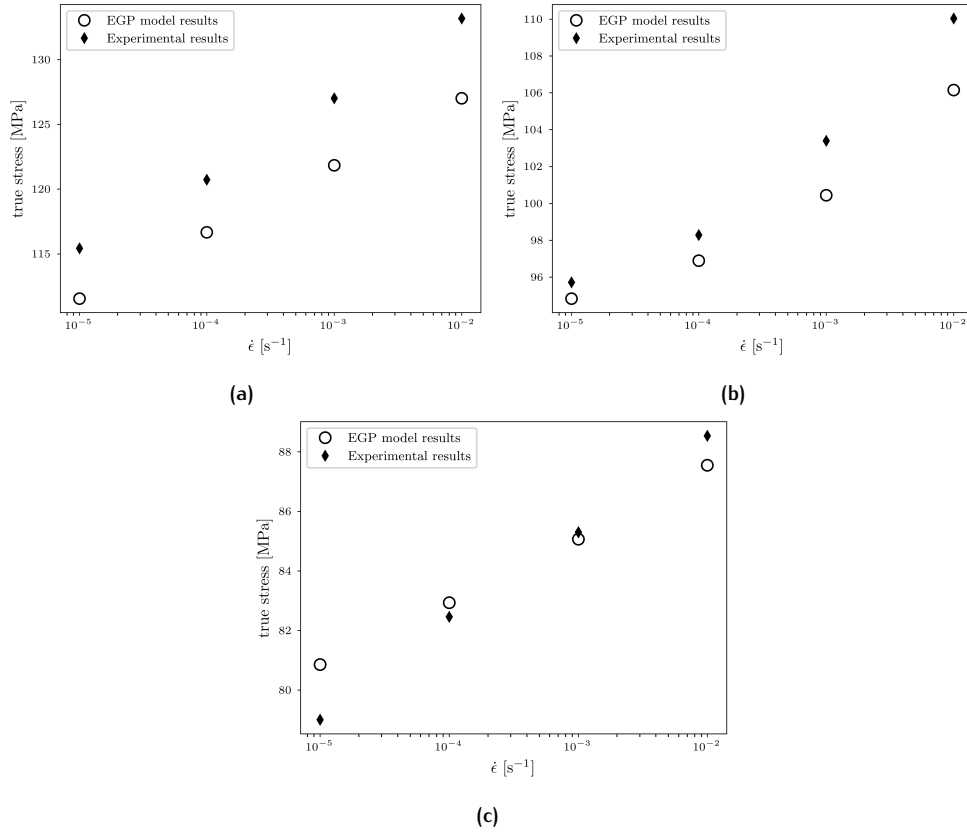


Figure 3.4: The strain-rate dependency of the original EGP model results and experimental results for a temperature of (a) 20°C, (b) 60°C and (c) 100°C taken at a strain of 0.1.

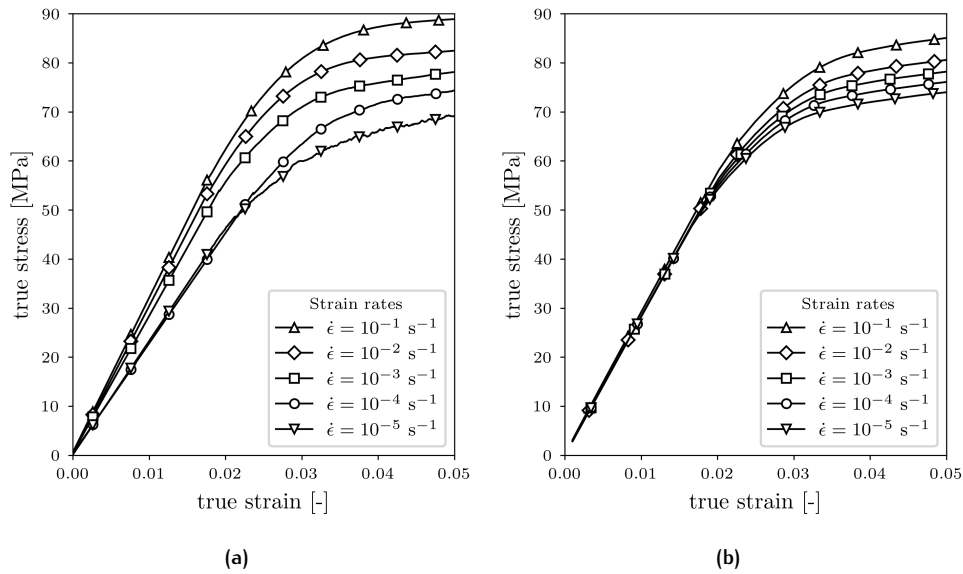


Figure 3.5: The pre-yield stress-strain behaviour at 100°C of (a) the experimental results and (b) original EGP model results.

### 3.4 CONFIRMATION OF THE PROBLEM STATEMENT

The claim of discrepancies between the experimental tests and the original EGP model as noted in the [problem definition](#) is as follows:

*A lower yield stress at lower temperatures and a lower strain-rate dependency at the low and moderate strain range is observed in the numerical model in comparison with the uniaxial compression tests.*

Two separate problems are listed and both checked based on the benchmark in section [3.3](#):

- *"lower yield stress at lower temperatures"*: the stress of the original EGP model at 20°C is always below the yield stress of the experimental results in Figure [3.3b](#). However, this is not observed in the results at 100°C (Figure [3.3f](#)). Thus, the effect is indeed present and only at lower temperatures.
- *"lower strain-rate dependency at the low and moderate strain range"*: Figure [3.4](#) does show a lower strain-rate dependency of the original EGP model results compared to the experimental results for a strain of 0.10. The discrepancy in the strain-rate dependency can also be observed in Figure [3.3](#), where the discrepancy in strain-rate dependency is larger when the curves within the difference plots for the different strain-rates are farther apart from each other.

It is concluded that the discrepancies specified in the stated claim are indeed present.

**ADDITIONAL DISCREPANCIES** Additionally, the lower strain-rate dependency is observed at higher strains, but not at the moderate strain range. This makes sense since the activation volume that determines the strain-rate dependency is fitted in the moderate strain range at 0.3. Another new observation is that the stress-strain behaviour in the pre-yield regime is strain-rate independent for the original EGP model results but it is strain-rate dependent for the experimental results, as shown in figure [3.5](#).

**ALL IDENTIFIED DIFFERENCES** The following identified differences of original EGP model results compared to the experimental results are to be solved in the chapter [4](#):

- A lower yield stress at lower temperatures;
- A lower strain-rate dependency at the small and large strains, but not at moderate strains;
- The original EGP model behaves strain-rate independent in the pre-yield regime.

## STRAIN-DEPENDENT PARAMETERS

The differences that are found between the experimental results and the EGP model results in section 3.4 are related to the strain-rate dependency and the temperature dependency. The characterization in section 3.1 shows that the strain-rate dependency and temperature dependency are respectively related to the Ree-Eyring parameters activation volume  $V_x$  and activation energy  $\Delta H_{0,x}$ . Thus, a solution related to these parameters is investigated in this chapter to reach an updated EGP model.

Section 4.1 will first show what indicates that a solution related to the Ree-Eyring parameters should be looked into. Section 4.2 discusses how to model strain dependency. Where-after, the found solution technique is first investigated for small to moderate strains in section 4.3, then for the pre-yield regime in section 4.4 and lastly for large strains in section 4.5. This leads to an updated EGP model in section 4.7. The solution introduces new parameters in the updated EGP model, section 4.6 describes how to characterize these new parameters. Lastly, an investigation outside of the temperature range and strain-rate range of the experiments is performed in section 4.8.

Chapter 5 expands on the found solution for a cyclic loading case instead of the uniaxial compression case that is discussed in this chapter. This leads to the fully updated EGP model in section 5.3. The stiffness tensor of the EGP model is lastly in chapter 6 updated for this fully updated EGP model.

### 4.1 REE-EYRING PARAMETERS AND PRESSURE DEPENDENCY

The original Ree-Eyring equation and an equation outlined by [Govaert et al. \[2001\]](#) have been used during the characterization of the original EGP model (Section 3.1) to determine multiple parameters. This yielded that these parameters are not constant over the strain while they are assumed constant within the EGP model. The equations have not been used within the characterization due to this reason, but they are expanded on in this section since they will lead to the solution of the problems stated in section 3.4. Please note that optimal constant values are not investigated, but only the true values of the parameters that evolve over the strain.

**ORIGINAL REE-EYRING EQUATION** The viscosity of the EGP model (Equation 2.12) is based on the Ree-Eyring flow theory, which is dependent on temperature and strain-rate and is characterized by the three original Ree-Eyring parameters: the activation volume  $V_x^*$ , the activation energy  $\Delta H_{0,x}$  and the rate constant  $\dot{\epsilon}_0$ , where  $x$  denotes the  $\alpha$ - or  $\beta$ -process:

$$\sigma(\dot{\epsilon}, T) = \sum_{x=\alpha,\beta} \frac{k_B T}{V_x^*} \sinh^{-1} \left( \frac{\dot{\epsilon}}{\dot{\epsilon}_{0,x}} \exp \left( \frac{\Delta H_x}{RT} \right) \right) \quad (4.1)$$

This function can be used to obtain an indication of the three Ree-Eyring parameters included in the EGP model. The rate constant is related to the initial viscosity and the activation volume from the original Ree-Eyring equation  $V_x^*$  is related to the activation volume used in the EGP model  $V_x$ . These parameters of the original Ree-Eyring equation are different due to changes made to the viscosity function during the development of the EGP model. This is the reason why only an indication of these parameters can be obtained with the original Ree-Eyring equation.

**PRESSURE DEPENDENCY** The pressure dependency  $\mu_x$  is used within the viscosity function (Equation 2.12). The following relation to determine the pressure dependency is outlined in Govaert et al. [2001]:

$$\tau_{eq} = \frac{\tau_0}{1 - \mu\alpha} \ln \left( \frac{2\dot{\gamma}_{eq}}{\dot{\gamma}_0} \right) \quad (4.2)$$

In which  $\tau_0 = \frac{V}{k_b T}$  with  $V$  the activation volume,  $k_b$  the Boltzmann's constant and  $T$  the temperature.  $\tau_{eq}$ ,  $\dot{\gamma}_{eq}$  and  $\alpha$  are parameters that are dependent on the loading conditions. These values are  $\frac{1}{3}\sqrt{3}\sigma_1$ ,  $\sqrt{3}\dot{\epsilon}_1$  and  $\frac{1}{3}\sqrt{3}$ , respectively, for the uniaxial compression case which is investigated. The unknown parameters are  $\mu$  and  $\dot{\gamma}_0$ , respectively the pressure dependency and a pre-exponential factor.

**METHOD** Equations 4.1 and 4.2 are fitted to the experimental results given in section 1.1 for several different strains to determine the three original Ree-Eyring parameters and the pressure dependency, respectively. The least squares method implemented in the scipy package in Python [Scipy org, 2021] is used to obtain a good fit.

The original Ree-Eyring equation (Equation 4.1) has been fitted to all experimental temperatures (20°C, 60°C and 100°C) and a strain-rate range of  $10^{-5} \text{ s}^{-1}$  to  $10^{-2} \text{ s}^{-1}$ . The equation to determine the pressure dependency (Equation 4.2) has been fitted to the experimental results at 100°C because only the  $\alpha$ -process is present for this temperature at the investigated strain-rate range of  $10^{-5} \text{ s}^{-1}$  to  $10^{-2} \text{ s}^{-1}$ . This means that the activation volume for the  $\alpha$ -process given in Appendix B can be used. The experimental results for a strain-rate of  $10^{-1} \text{ s}^{-1}$  have been omitted for fitting both equations since they are influenced by adiabatic heating and would lead to incorrect fits.

**RESULTS** The method leads to a good fit to the experimental results of both equations as can be seen by plotting the strain-rate dependency for the strains of 0.075 and 0.3 in Figure 4.1. The lines of equations 4.1 and 4.2 line well up with the markers from the experiments.

**IMPORTANT OBSERVATION** An important observation which is made after good fits have been obtained is that the values found for the three original Ree-Eyring parameters (the activation volume  $V_x^*$ , activation energy  $\Delta H_x$  and the rate constant  $\dot{\epsilon}_{0,x}$ ) and the pressure dependency are not constant when plotted against the strain. This can be seen well in Figure 4.2.

Already, two literature sources include an evolution of the Ree-Eyring parameters for modelling polymers. Senden et al. [2010] uses the EGP model as well and applies an evolving activation energy and initial viscosities (Equations 2.27-2.30) for PC. Wendlandt et al. [2005] uses another model that is similar to the EGP model and applies an evolving activation volume for PMMA, PPO, PC and PS. However, these works are different from this thesis because their goal is to describe the Bauschinger effect by including viscous hardening. They also focus on the large strain range, other polymers and investigate a cyclic loading case. The fit of the original Ree-Eyring equations in section 4.1 hints that all three Ree-Eyring parameters should evolve over the full strain range, but these papers only evolve one or two Ree-Eyring parameters.

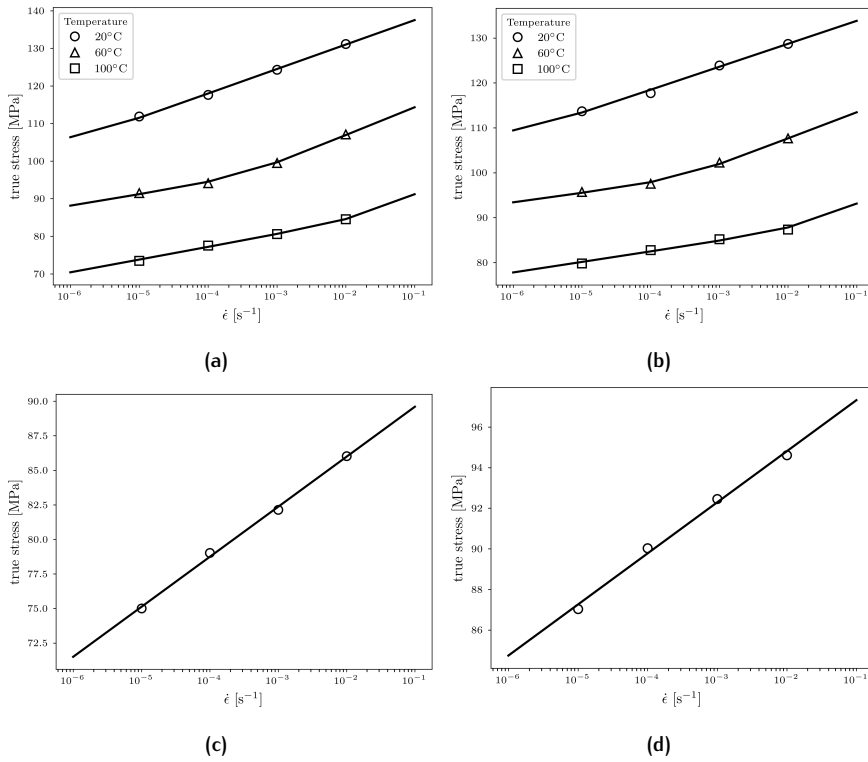


Figure 4.1: The fitted original Ree-Eyring equation (solid lines) to the experimental results (markers) for a strain of (a) 0.075 and (b) 0.3 and the fitted equation to determine the pressure dependency (solid lines) to the experimental results (markers) at 100°C for a strain of (c) 0.075 and (d) 0.3 in strain-rate dependency plots.

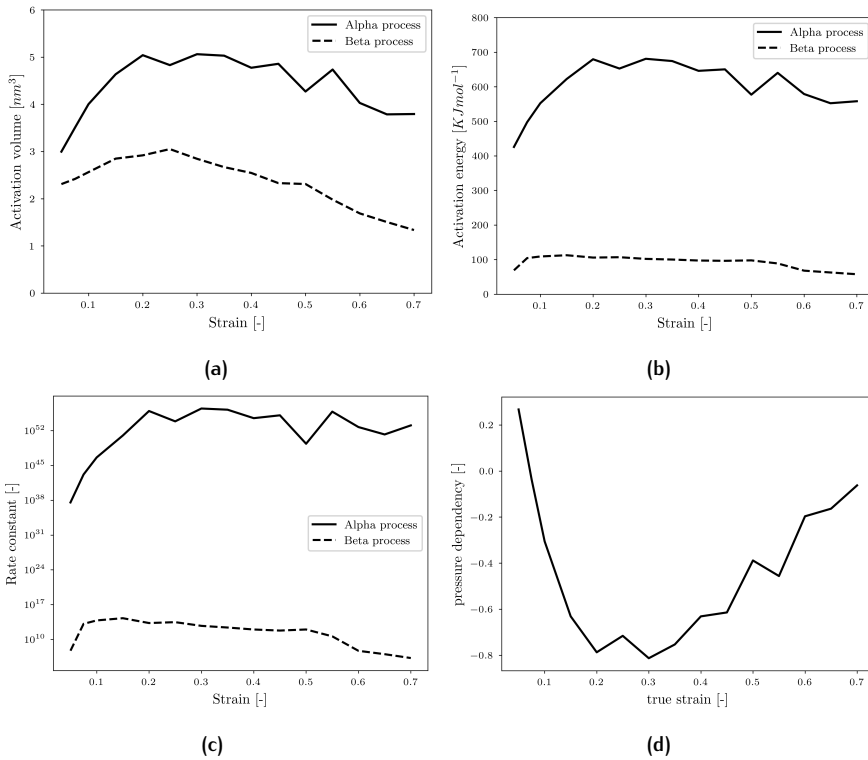


Figure 4.2: The evolution of the (a) activation volume, (b) activation energy, (c) rate constant and (d) pressure dependency, as characterized from the original Ree-Eyring equation (Equation 4.1) and the equation to determine the pressure dependency (Equation 4.2).

This chapter will further investigate making any or all of the three Ree-Eyring parameters strain-dependent to accurately model the stress over the entire strain range. Making the pressure dependency strain-dependent is not further investigated. This is because a strain-dependent pressure dependency leads to large changes in the stresses obtained from the EGP model, which did not correspond with the experimental stress-strain results.

## 4.2 STRAIN DEPENDENCY

Senden et al. [2012a] introduced the invariant function  $I_r(\tilde{\mathbf{B}})$  (Equation 2.24) which is approximately proportional to the total strain. This is valid for both positive strains and negative strains. The invariant function also stays approximately proportional to the strain when the loading direction is reversed. This function is good to model the strain dependency of the Ree-Eyring parameters.

Another option is to relate the Ree-Eyring parameters to the equivalent plastic strain (Equation 2.19). It would make sense to make the Ree-Eyring parameters dependent on the plastic strain since they are physically coupled. However, Figure 3.5 shows a discrepancy in the strain-rate dependency in the pre-yield regime. There should be the possibility to evolve the Ree-Eyring parameters from the onset of loading to change anything in this pre-yield regime. But the plastic strain starts to accumulate after the pre-yield regime. If the Ree-Eyring parameters are coupled to the plastic strain, they can only change after the pre-yield regime. Another disadvantage is that the plastic strain is directly coupled to the viscosity and thus the Ree-Eyring parameters, making characterization very hard. The last disadvantage is that the equivalent plastic strain does not decrease again when the loading direction is reversed, leading to less freedom in modelling the behaviour of the Ree-Eyring parameters in that loading case.

It is chosen to relate the Ree-Eyring parameters evolution to the invariant function  $I_r(\tilde{\mathbf{B}})$  due to the disadvantages of relating the Ree-Eyring parameters evolution to the equivalent plastic strain.

## 4.3 SMALL TO MODERATE STRAIN RANGE

Firstly, the small to moderate strain range ( $\epsilon < 0.4$ ) is investigated. The goal is to create an evolution of the Ree-Eyring parameters that stays constant after a certain strain. Only the small to moderate strain range is influenced in this way. The  $\tanh()$  function has this property, thus it has been chosen for the evolution of the Ree-Eyring parameters. This evolution looks in the most basic form as follows:

$$f(I_r(\tilde{\mathbf{B}})) = A + B \cdot \tanh(C \cdot (I_r - D)) \quad (4.3)$$

**NEEDED REE-EYRING EVOLUTION** It is investigated which of the three Ree-Eyring parameters should be strain-dependent. The Ree-Eyring parameters related to the  $\beta$ -process can be assumed constant at small to moderate strains based on Figure 4.2, only the Ree-Eyring parameters related to the  $\alpha$ -process have to be strain-dependent in this case.

An evolution of activation volume based on Equation 4.3 has been implemented in the EGP model while the activation energy and initial viscosities are kept constant. This leads to too high stresses around the yield point for a fixed temperature.

Next, an evolution based on Equation 4.3 for all initial viscosities is also implemented in the EGP model. The strain-rate dependency and shape of the stress-strain curve are very well approximated at the fixed temperature.

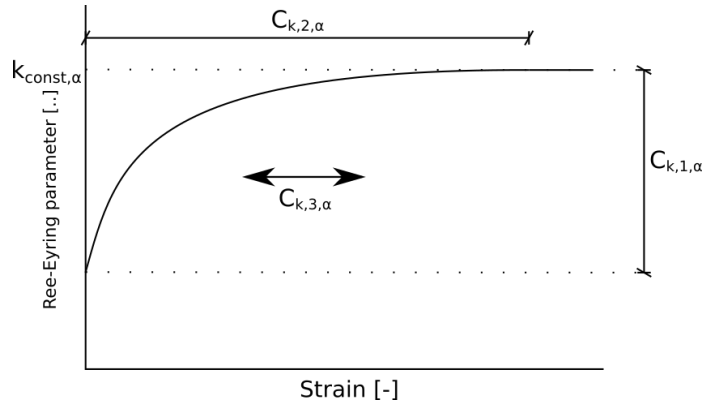


Figure 4.3: Visualisation of the behaviour of the constants for the Ree-Eyring parameters evolution in which  $k = V, \Delta H$  or  $\eta$ .

If the previously fixed temperature is changed, then the stresses are again incorrect around the yield point. An evolution of the activation energy is needed to correctly model other temperatures. If the characterization has only been performed at one temperature and no other temperature will be used in any analysis, the evolution of the activation energy can be omitted. This can also mathematically be seen in Equation 4.8 where the term with the activation energy will always be equal to one if an analysis with the same temperature as the characterization base temperature is run.

It is concluded that all three Ree-Eyring parameters should be strain-dependent to quantitatively model the stress-strain behaviour in the small to moderate strain range.

**REE-EYRING PARAMETERS EVOLUTION FUNCTIONS** The following functions for the evolution of the Ree-Eyring parameters are created:

$$V_{\alpha} = (V_{const,\alpha} - C_{V,1,\alpha}) + C_{V,1,\alpha} \cdot \tanh(C_{V,2,\alpha} \cdot (I_r - C_{V,3,\alpha})) \quad (4.4)$$

$$\Delta H_{0\alpha} = (\Delta H_{const,\alpha} - C_{\Delta H,1,\alpha}) + C_{\Delta H,1,\alpha} \cdot \tanh(C_{\Delta H,2,\alpha} \cdot (I_r - C_{\Delta H,3,\alpha})) + S_{H_{\alpha}} R_{\gamma_{\alpha}} \quad (4.5)$$

$$\eta_{0,\alpha,i} = \eta_{const,\alpha,i} \cdot 10^{-C_{\eta,1,\alpha} + C_{\eta,1,\alpha} \cdot \tanh(C_{\eta,2,\alpha} \cdot (I_r - C_{\eta,3,\alpha}))} \quad (4.6)$$

The influence of each constant is visualized in Figure 4.3. It can be seen that the  $k_{const,\alpha}$  constants for  $k = V, \Delta H$  and  $\eta$  are the same value as the previous constant values. The Ree-Eyring parameters will stay constant after an 'influence length of the evolution' that is determined with the  $C_{k,2,\alpha}$  constants. The  $C_{k,1,\alpha}$  constants determine how large the decrease of a Ree-Eyring parameter is at the onset of loading. The  $C_{k,1,\alpha}$  constants cannot be larger than the constant values  $k_{const,\alpha}$  since negative values for the Ree-Eyring parameters are incorrect. The  $C_{k,3,\alpha}$  constants are used to shift the function. This can be useful to get a better fit. However,  $C_{k,3,\alpha}$  should be used with care because it can lead to negative Ree-Eyring parameters that are incorrect.

An advantage of these formulations is that by taking all three  $C_{k,1,\alpha}$  constants equal to zero, The functions reduce to the old formulation where the  $k_{const,\alpha}$  constants are the constant Ree-Eyring parameters  $V_{\alpha}$ ,  $\Delta H_{\alpha}$  and  $\eta_{\alpha}$  from the original EGP model.

**AGEING DEPENDENCE OF THE ACTIVATION ENERGY** Equation 4.5 includes the term  $S_{H_{\alpha}} R_{\gamma_{\alpha}}$  introduced by Senden et al. [2012a] to fit the temperature dependency

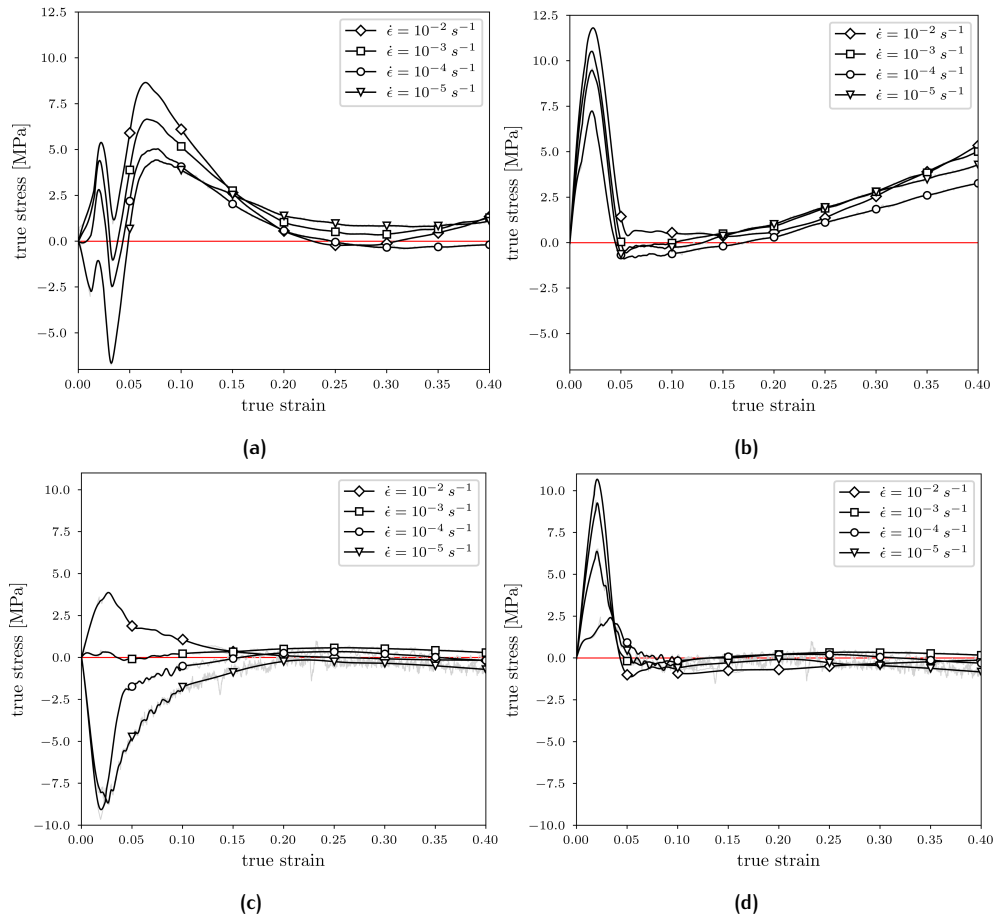


**Figure 4.4:** The difference between the EGP model results and the experimental results for (a, c) the benchmark and (b, d) the updated EGP model. This is shown at 20°C (a+b) and (c, d) 100°C.

of the yield point. However, it is unknown how large the influence of these parameters should be if the evolution of the Ree-Eyring parameters for the small-moderate range is included in the model. The Evolution of the Ree-Eyring parameters is already used to fit the temperature dependency of the yield point. This cannot be investigated with the experimental data from [Sundrarajan and Govaert \[2021\]](#) because practically no ageing of the material is involved. However, [Senden et al. \[2012b\]](#) determined that the activation energy is influenced by the ageing of polymers.

It has been chosen to still include the term  $S_{H_\alpha} R_{\gamma_\alpha}$  since it cannot be determined that the term  $S_{H_\alpha} R_{\gamma_\alpha}$  can be removed with the new evolution of the Ree-Eyring parameters and [Senden et al. \[2012b\]](#) indicates that this could be relevant with an aged sample.

**IMPLEMENTATION IN THE CODE** Equation 3.1 shows that the initial viscosities are shifted based on the state factor and the activation energy. The shift that is based on the activation energy should become strain-dependent since the activation energy is now strain-dependent. This shift is performed in the updated EGP model itself instead of an operation on the inputted initial viscosities. Thus, Equation 3.1 is changed to:

$$\eta_{0_{x,i}} = \eta_{0_{x,i,calc}} \exp(-S_x) \quad (4.7)$$

and the viscosity Equation 2.12 is changed to:

$$\eta_{x,i} = \eta_{0_{x,i}} \frac{\bar{\tau}_x / \tau_{0_x}}{\sinh(\bar{\tau}_x / \tau_{0_x})} \exp\left(\frac{\Delta H_x}{R} \left(\frac{1}{T} - \frac{1}{T_{x,base}}\right)\right) \exp\left(\frac{\mu_x p}{\tau_{0_x}}\right) \exp(S_x) \quad (4.8)$$

Table 4.1: Used values for the evolution of the Ree-Eyring parameters in section 4.3.

		$k_{const,\alpha}$	$C_{k,1,\alpha}$	$C_{k,2,\alpha}$	$C_{k,3,\alpha}$
<b>Activation volume;</b>	$k = V$	$9.2 \cdot 10^{-18}$	$9.2 \cdot 10^{-18}$	5.0	0.0
<b>Activation energy;</b>	$k = \Delta H$	$640 \cdot 10^6$	$640 \cdot 10^6$	6.85	0.0
<b>Initial viscosities;</b>	$k = \eta$	see appendix B	22.6	5.2	0.06

$T_{x,base}$  is the temperature that is used to characterize the modal parameters of a certain process. The following is correct for the characterization of the EGP model in this thesis:  $T_{x,base}$  is 100°C and 20°C for the  $\alpha$ - and  $\beta$ -process, respectively. This can be seen in section 3.1.

**COMPARISON WITH THE BENCHMARK** Equations 4.4, 4.5 and 4.6 are implemented in the EGP model. The parameters listed in Table 4.1 have been used to produce updated stress-strain curves. Section 4.6 describes how these values are obtained. The parameters related to the  $\beta$ -process are dependent on the  $\alpha$ -process because the stresses of the  $\alpha$ -process are subtracted from the experimental stresses to characterize the modal parameters for the  $\beta$ -process. Due to the different results for the  $\alpha$ -process, the modal parameters related to the  $\beta$ -process have been re-characterized.

The difference plots for the benchmark and the updated EGP model are shown next to each other in Figure 4.4. The stresses of the updated EGP model confirm well with the experimental results at moderate strain levels ( $\epsilon \approx 0.05$  till 0.25), which is an improvement upon the benchmark. The strain-rate dependency of the updated EGP model also corresponds well with the experimental results since the different curves in the difference plot are close to each other. However, the results are worse than before for the large strain range and the pre-yield regime ( $\epsilon < 0.05$ ).

**REDUCTION OF PARAMETERS** A disadvantage of the Ree-Eyring parameters evolution shown in Equations 4.4-4.6 is that multiple new parameters are added to the EGP model. A general goal is to use as few parameters as possible for models such as the EGP model. Thus, several methods have been used to try to reduce the number of parameters:

- Find similarities between the evolution of the three Ree-Eyring parameters. The goal is to couple constants needed for the evolution of the Ree-Eyring parameters => No similarities are found that lead to the possibility of coupling any of the constants for the evolution of the Ree-Eyring parameters;
- Find similarities between the evolution of the three Ree-Eyring parameters in literature => None are found;
- Approximate the evolution of the three Ree-Eyring parameters with a single function that is added to the viscosity function => This leads to inaccurate results due to the complex dependencies on other parameters;
- Including a non-constant activation volume in the determination of the initial viscosities and shear moduli to account for the evolution of the activation volume with the modes => Correct stress-strain behaviour is not obtained. Furthermore, this leads to unstable FEM analyses due to a very high number of resulting modes ( $\pm 60$ ), which is computationally very expensive;
- Find other functions than the  $\tanh()$  function with the same characteristics => None are found that have fewer parameters.

None of the approaches leads to a reduction of the number of parameters. Therefore, it is concluded that the approach with the  $\tanh()$  function and multiple new parameters is the best approach to follow.

**Table 4.2:** Used values for the evolution of the Ree-Eyring parameters and shear moduli in section 4.4.

		$k_{const,\alpha}$	$C_{k,1,\alpha}$	$C_{k,2,\alpha}$	$C_{k,3,\alpha}$
<b>Activation volume;</b>	$k = V$	$9.2 \cdot 10^{-18}$	$9.2 \cdot 10^{-18}$	5.0	0.0
<b>Activation energy;</b>	$k = \Delta H$	$640 \cdot 10^6$	$640 \cdot 10^6$	6.85	0.0
<b>Initial viscosities;</b>	$k = \eta$	see appendix B	22.6	5.2	0.06
<b>Shear moduli;</b>	$k = G$	see appendix B	0.50	20	0.0

#### 4.4 PRE-YIELD REGIME

Two separate problems are discussed in this section. Firstly, the new problem that occurs when applying the evolution of the Ree-Eyring parameters, which is shown in Figure 4.4. This figure shows that a large stress difference is present between the updated EGP model and the experimental results for the pre-yield regime ( $\epsilon < 0.05$ ). Secondly, the problem regarding the absence of strain-rate dependency in the pre-yield regime as discussed in section 3.4 and shown in Figure 3.5.

**FIRST PROBLEM; STRESS DEVIATIONS PRE-YIELD REGIME** Changing the evolution of the Ree-Eyring parameters (Equations 4.4, 4.5 and 4.6) does not in any way lead to stress-strain results for the pre-yield regime that correspond better with the experimental results. This is because the Ree-Eyring parameters change the viscosity of the model, which is linked to the plastic deformation while the pre-yield behaviour is largely elastic.

There may be an unidentified effect at play that leads to higher experimental results for the pre-yield regime. The taken approach is to increase the shear moduli for the pre-yield regime, which would shift the stress with the same value for all strain-rates and temperatures. Almost the same deviation is visible at all strain-rates and temperatures in the pre-yield regime. Thus, this approach is justified.

The evolution of the shear moduli is also based on a  $\tanh()$  function related to the invariant function. The reason for this is that the  $\tanh()$  function reduces to 1. The evolution can be set such that only the pre-yield regime is influenced. Furthermore, the evolution works in the same way as the evolution of the Ree-Eyring parameters. A function leading to more optimal results is a  $\tanh^2()$  function, but this is not applied since it is harder to characterize. The function for the shear moduli evolution is given by:

$$G_{0,\alpha,i} = G_{const,\alpha,i} \cdot [1 + C_{G,1,\alpha} - C_{G,1,\alpha} \cdot \tanh(C_{G,2,\alpha} \cdot (I_r(\tilde{\mathbf{B}}) - C_{G,3,\alpha}))] \quad (4.9)$$

**COMPARISON WITH THE BENCHMARK** Equation 4.9 is implemented in the updated EGP model from section 4.3. The parameters listed in Table 4.2 are used for the results in Figure 4.5. The influence length of the shear moduli evolution has been made very small by using a value of 20 for the  $C_{G,2,\alpha}$  parameter. This limits the influence to the pre-yield regime.

Figure 4.5 shows that the curves in the pre-yield regime are shifted downwards from the state in Figures 4.4b and 4.4d. This shift leads to better results in the pre-yield regime. However, the strain-rate dependency for the results at 20°C is still not optimal. As mentioned before, since the strain-rate dependency/activation volume is coupled to the plastic strain, it cannot be solved by modifying the activation volume for the (elastic) pre-yield regime.

**SECOND PROBLEM; PRE-YIELD BEHAVIOUR AND PLASTIC STRAIN** Figure 3.5 shows that the pre-yield behaviour of the original EGP model is qualitatively different from the experimental results. The original EGP model does not show any strain-rate de-

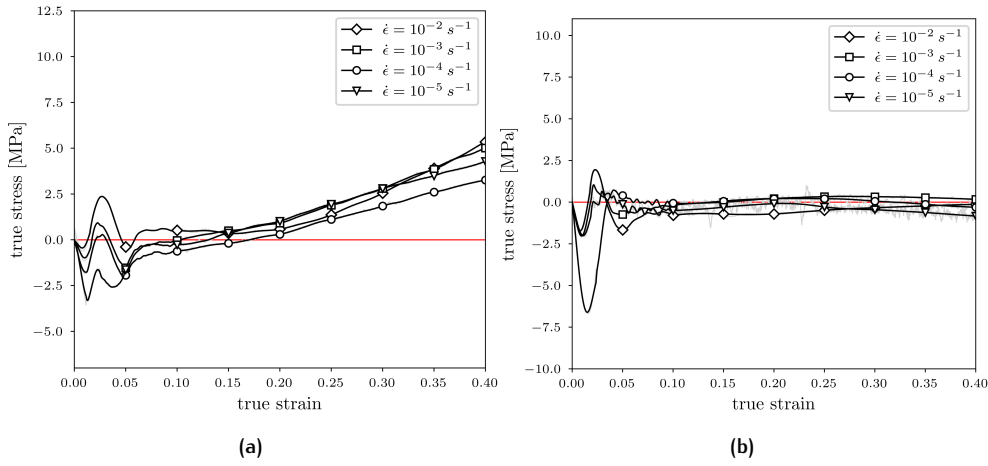


Figure 4.5: The difference between the EGP model results and the experimental results for the EGP model with the Ree-Eyring parameters and shear moduli evolution. This is shown at (a) 20°C and (b) 100°C.

pendency in the pre-yield regime, while strain-rate dependency is present in the experiments.

Figure 4.6a shows that quantitatively better behaviour is obtained with the updated EGP model. Thus, this problem is already solved by introducing the evolution of the Ree-Eyring parameters from section 4.3.

Figure 4.6b shows the equivalent plastic strain as defined in Equation 2.19 for the original and updated EGP model. This equivalent plastic strain is directly dependent on the viscosity function. The figure shows no plastic flow in the pre-yield regime of the original EGP model. The strain-rate independence of the original EGP model can be explained by this absence of the plastic flow. The plastic flow starts at the onset of loading by introducing the evolution of the Ree-Eyring parameters, which is supported by the fact that the plastic deformation in polymers develops upon loading [Govaert et al., 2001].

## 4.5 LARGE STRAIN RANGE

Figure 4.5 clearly show that there are still deviations at large strains. These deviations are observed at all strain-rates and temperatures in Figure 3.3. The evolution of the Ree-Eyring parameters introduced in section 4.3 only influences the small to moderate strains, while Figure 4.2 clearly shows that the Ree-Eyring parameters should decrease in the large strain range ( $\epsilon > 0.4$ ). These deviations are solved when a quadratic evolution of the Ree-Eyring parameters for the  $\alpha$ -process as well as for the  $\beta$ -process in the following form is implemented for  $k = \Delta H, V$  or  $\eta$  and  $x = \alpha$  or  $\beta$ :

$$f(I_r(\tilde{\mathbf{B}})) = k - C_{k,A,x} \cdot I_r^2 \quad (4.10)$$

The stresses from the EGP model are incorrect when the activation energy or activation volume is near zero when or the initial viscosities become very small. The term  $C_{k,A,x} \cdot I_r^2$  leads to monotonically decreasing Ree-Eyring parameters. Thus, this incorrect stress behaviour will happen if strains become large enough. The  $C_{k,A,x}$  constant should be lowered if these large strains are expected. Consequently, the Ree Eyring parameters decrease more gradually, possibly preventing the incorrect stresses but leading to less accurate results. It is also possible to limit all three Ree-Eyring parameters when one given lower limit has been reached. However, the values for these lower limits are unknown since there is no experimental data for such large strains. This can be a subject for future research.

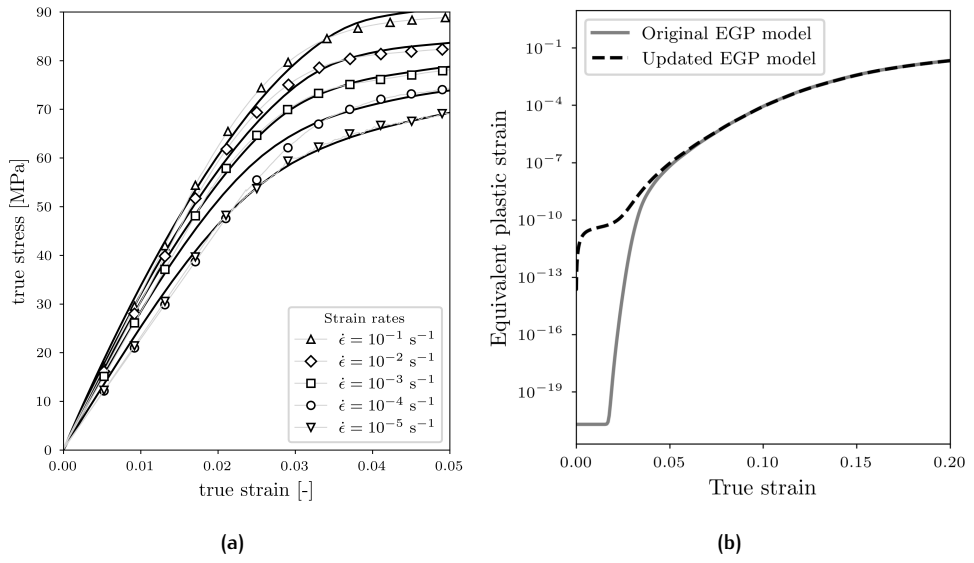


Figure 4.6: (a) The stress-strain curves created with the updated EGP model for the pre-yield regime plotted in black solid lines and the experimental stress-strain curves plotted with markers. (b) The equivalent plastic strain for the pre-yield regime. Both at  $100^\circ\text{C}$ .

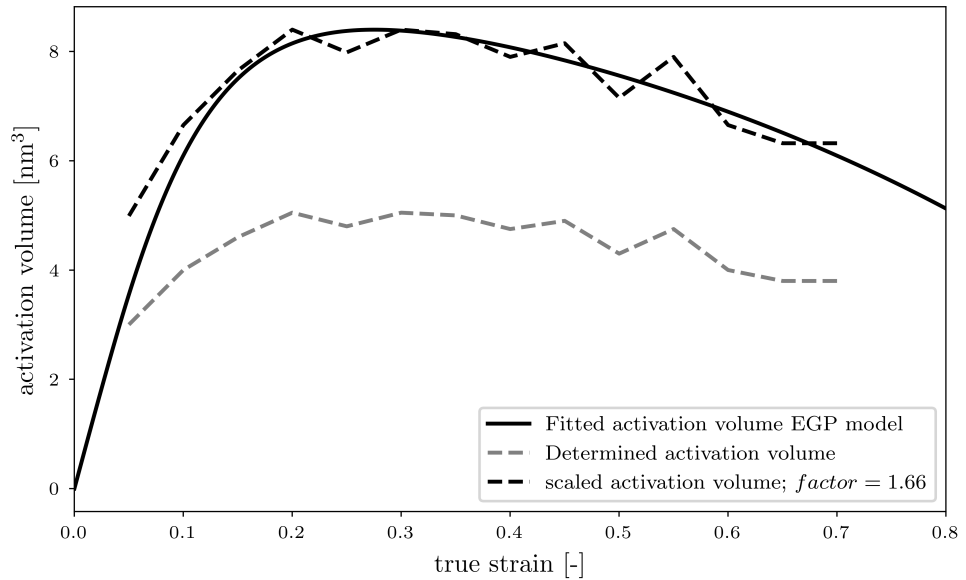


Figure 4.7: The characterization of the activation volume, which is based on fitting the original Ree-Eyring equation to experimental results.

## 4.6 CHARACTERIZATION OF THE UPDATED EGP MODEL

The Ree-Eyring parameters evolution (Equations 4.4-4.6) and shear moduli evolution (Equation 4.9) need to be characterized by taking the following steps after all other parameters have been determined:

1. Determine the evolution of the Ree-Eyring parameters by fitting Equation 4.1 to the experimental results;
2. Determine the strain-rate dependency and corresponding activation volume at a fixed strain with the EGP model;
3. Scale the evolution of the activation volume from step 1 to the needed activation volume at the fixed strain from step 2 as seen in Figure 4.7;
4. Fit the activation volume for the  $\alpha$ -process within the EGP model (Equation 4.11) to the scaled activation volume evolution from step 3 with the fitting parameters  $V_{const,\alpha}$ ,  $C_{V,1,\alpha}$ ,  $C_{V,2,\alpha}$ ,  $C_{V,3,\alpha}$  and  $C_{V,4,\alpha}$  as seen in Figure 4.7;
5. Run the EGP model at the temperature where the modal parameters of the  $\alpha$ -process are determined ( $T_{\alpha,base}$ ) to fit the stress-strain curve from the updated EGP model to the experimental stress-strain curve with the evolution of the initial viscosities for the  $\alpha$ -process;
6. Run the EGP model with a different temperature on a strain-rate where only the  $\alpha$ -process is present to fit the evolution of the activation energy for the  $\alpha$ -process;
7. Recharacterize the modal parameters for the  $\beta$ -process because different results for the  $\alpha$ -process lead to a different characterization of the  $\beta$ -process;
8. repeat steps 4-6 for the  $\beta$ -process;
9. Apply an evolution of the shear moduli with an 'influence length' equal to the pre-yield regime to correctly shift the response of the pre-yield regime upwards or downwards.

It can be easier to first fit the small to moderate strain range with  $X_{const,\alpha}$ ,  $X_{const,\beta}$ ,  $C_{x,1,\alpha}$ ,  $C_{x,2,\alpha}$  and  $C_{x,3,\alpha}$  then repeat all steps to fit the large strain range with  $C_{x,4,\alpha}$  and  $C_{x,4,\beta}$ .

The number of needed stress-strain curves to characterize the updated EGP model stays the same, which is a significant feature of the new evolution of the Ree-Eyring parameters.

The listed steps are taken to create an updated characterization. This characterization is from here on used for the updated EGP model. Table 4.3 shows the values that have been obtained to create a good fit. The values for the initial viscosities in Table 4.3b are very different than for the benchmark due to using Equation 4.8 instead of 3.1 for shifting the initial viscosities. The stress-strain figures and difference figures corresponding to the characterization are discussed in the next section.

Table 4.3: The characterized parameters for the updated EGP model.

(a) General parameters.

Parameter	Value	Unit	Parameter	Value	Unit
$T$	Variable	$^{\circ}\text{C}$	$C_{G,1,\alpha}$	0.50	-
$R$	8.31	$\text{J} \cdot \text{mol}^{-1} \cdot \text{K}^{-1}$	$C_{G,2,\alpha}$	20.0	-
$k_b$	$1.38 \cdot 10^{-20}$	$\text{N} \cdot \text{mm} \cdot \text{K}^{-1}$	$C_{G,3,\alpha}$	0.0	-
$G_r$	5.0	$\text{MPa}$	$C_{\eta,1,\alpha}$	52	-
$\alpha_r$	0.22	-	$C_{\eta,2,\alpha}$	5.2	-
$\zeta_r$	0	-	$C_{\eta,3,\alpha}$	0.06	-
$\mu_{\alpha}$	0.06	-	$C_{\eta,4,\alpha}$	-27.6	-
$\mu_{\beta}$	0.06	-	$C_{\eta,4,\beta}$	0	-
$S_{S_{\alpha}}$	2.0	-	$\Delta H_{const,\alpha}$	$640 \cdot 10^3$	$\text{J} \cdot \text{mol}^{-1}$
$S_{S_{\beta}}$	0	-	$C_{\Delta H,1,\alpha}$	$640 \cdot 10^3$	$\text{J} \cdot \text{mol}^{-1}$
$S_{H_{\alpha}}$	0	-	$C_{\Delta H,2,\alpha}$	6.85	-
$S_{H_{\beta}}$	0	-	$C_{\Delta H,3,\alpha}$	0	-
$r_{0,\alpha}$	0.965	-	$C_{\Delta H,4,\alpha}$	$-100 \cdot 10^3$	$\text{J} \cdot \text{mol}^{-1}$
$r_{1,\alpha}$	-5.0	-	$\Delta H_{const,\beta}$	$100 \cdot 10^3$	$\text{J} \cdot \text{mol}^{-1}$
$r_{2,\alpha}$	-5.0	-	$C_{\Delta H,4,\beta}$	$-55 \cdot 10^3$	$\text{J} \cdot \text{mol}^{-1}$
$r_{0,\beta}$	0.965	-	$V_{const,\alpha}$	$9.2 \cdot 10^{-18}$	$\text{mm}^3$
$r_{1,\beta}$	-5.0	-	$C_{V,1,\alpha}$	$9.2 \cdot 10^{-18}$	$\text{mm}^3$
$r_{2,\beta}$	-5.0	-	$C_{V,2,\alpha}$	5.0	-
$\kappa$	5475	$\text{N}/\text{mm}^2$	$C_{V,3,\alpha}$	0	-
			$C_{V,4,\alpha}$	$-3.0 \cdot 10^{-18}$	$\text{mm}^3$
			$V_{const,\beta}$	$5.0 \cdot 10^{-18}$	$\text{mm}^3$
			$C_{V,4,\beta}$	$-3.0 \cdot 10^{-18}$	$\text{mm}^3$

(b) Modal parameters.

 $\alpha$ -process modes $\beta$ -process modes

Mode	shear modulus	initial viscosity	shear modulus	initial viscosity
	$G_{const,i}$ [MPa]	$\eta_{const,i}$ [MPa · s]	$G_{const,i}$ [MPa]	$\eta_{const,i}$ [MPa · s]
1	97.663	$1.402 \cdot 10^{39}$	24.519	260.259
2	96.330	$1.975 \cdot 10^{38}$	39.148	278.018
3	43.014	$1.260 \cdot 10^{37}$	39.761	56.583
4	50.714	$2.122 \cdot 10^{36}$		
5	51.848	$3.099 \cdot 10^{35}$		
6	64.795	$5.532 \cdot 10^{34}$		
7	84.610	$1.032 \cdot 10^{34}$		
8	109.077	$1.900 \cdot 10^{33}$		
9	99.498	$2.476 \cdot 10^{32}$		
10	75.487	$2.683 \cdot 10^{31}$		
11	34.353	$1.744 \cdot 10^{30}$		
12	36.707	$2.663 \cdot 10^{29}$		
13	24.847	$2.574 \cdot 10^{28}$		
14	24.904	$3.686 \cdot 10^{27}$		
15	17.940	$3.793 \cdot 10^{26}$		
16	21.714	$6.558 \cdot 10^{25}$		
17	15.974	$6.891 \cdot 10^{24}$		
18	14.928	$9.199 \cdot 10^{23}$		
19	15.567	$1.370 \cdot 10^{23}$		
20	8.351	$1.050 \cdot 10^{22}$		
21	6.457	$1.160 \cdot 10^{21}$		
22	1.166	$2.992 \cdot 10^{19}$		
23	35.205	0.961		

## 4.7 EVOLUTION OVER THE FULL STRAIN RANGE

The evolution of the Ree-Eyring parameters for the small to moderate strain range is determined in section 4.3 and is shown in Equations 4.4-4.6. These equations for the  $\alpha$ -process are updated with the evolution for large strains determined in section 4.5 as shown in Equation 4.10. The evolution of the Ree-Eyring parameters for the  $\beta$ -process are fully derived from Equation 4.10. Equations 4.11-4.16 show the evolution of the Ree-Eyring parameters for both processes and over the full strain range:

$$V_\alpha = (V_{const,\alpha} - C_{V,1,\alpha}) + C_{V,1,\alpha} \cdot \tanh(C_{V,2,\alpha} \cdot (I_r(\tilde{\mathbf{B}}) - C_{V,3,\alpha})) + C_{V,4,\alpha} I_r^2(\tilde{\mathbf{B}}) \quad (4.11)$$

$$\Delta H_{0\alpha} = (\Delta H_{const,\alpha} - C_{\Delta H,1,\alpha}) + C_{\Delta H,1,\alpha} \cdot \tanh(C_{\Delta H,2,\alpha} \cdot (I_r(\tilde{\mathbf{B}}) - C_{\Delta H,3,\alpha})) + C_{\Delta H,4,\alpha} I_r^2(\tilde{\mathbf{B}}) + S_{H_\alpha} R_{\gamma_\alpha}(\bar{\gamma}_p) \quad (4.12)$$

$$\eta_{0,\alpha,i} = \eta_{const,\alpha,i} \cdot \exp(-C_{\eta,1,\alpha} + C_{\eta,1,\alpha} \cdot \tanh(C_{\eta,2,\alpha} \cdot (I_r(\tilde{\mathbf{B}}) - C_{\eta,3,\alpha}))) \cdot \exp(C_{\eta,4,\alpha} I_r^2(\tilde{\mathbf{B}})) \quad (4.13)$$

$$V_\beta = V_{const,\beta} + C_{V,4,\beta} I_r^2(\tilde{\mathbf{B}}) \quad (4.14)$$

$$\Delta H_{0\beta} = \Delta H_{const,\beta} + C_{\Delta H,4,\beta} I_r^2(\tilde{\mathbf{B}}) + S_{H_\beta} R_{\gamma_\beta}(\bar{\gamma}_p) \quad (4.15)$$

$$\eta_{0,\beta,i} = \eta_{const,\beta,i} \cdot \exp(C_{\eta,4,\beta} I_r^2(\tilde{\mathbf{B}})) \quad (4.16)$$

Section 4.4 shows that the shear moduli should also evolve within the pre-yield regime according to Equation 4.9.

**IMPLEMENTATION IN THE CODE** Appendix E shows the updated C++ code. The updated viscosity function from Equation 4.8 and the new functions related to the evolution of the Ree-Eyring parameters and shear moduli as seen in Equations 4.11-4.16 and 4.9 are implemented in the code. The parameter *htBnon* is also already included. This parameter is related to cyclic loading of the material and will be introduced in chapter 5.

**STRESS-STRAIN RESULTS UPDATED EGP MODEL** Figure 4.8 shows the difference between the updated EGP model results and the experimental results with the characterization shown in Table 4.3. Stress-strain graphs zoomed in to after-yield stress levels for each temperature can also be seen in Figure 4.8 and the full curves can be found in appendix D. Notice that these results from the updated EGP model are a large improvement upon the results from the benchmark shown in Figure 3.3 and appendix C.

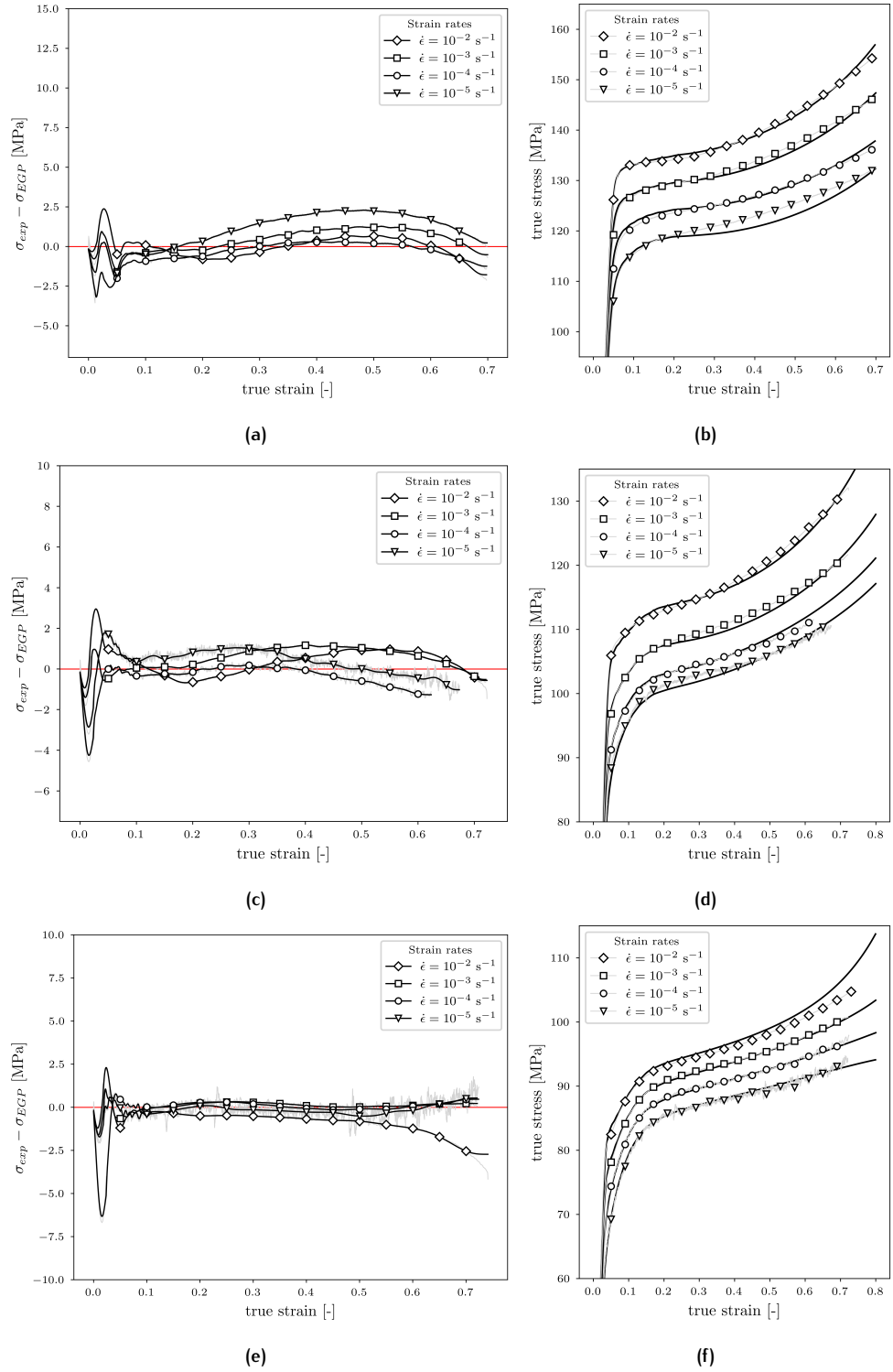


**Figure 4.8:** (a, c, e) The difference between the experimental results and the updated EGP model benchmark results. (b, d, f) The experimental stress-strain results plotted with markers and the updated EGP results plotted in solid lines. Both for a number of different strain-rates and at (a, b) 20°C, (c, d) 60°C and (e, f) 100°C. The grey lines in the plots with the difference are the exact difference including the noise from the experiments while the black lines are without the noise, which are obtained by filtering the grey lines with a Butterworth filter.

## 4.8 LARGER TEMPERATURE AND STRAIN-RATE RANGE

The updated characterization, Ree-Eyring parameters evolution and shear moduli evolution are based on the available experimental data for a strain-rate range of  $10^{-1} \text{ s}^{-1}$  to  $10^{-5} \text{ s}^{-1}$  and a temperature range of  $20^\circ\text{C}$  to  $100^\circ\text{C}$ . The model should still perform well outside of these ranges. Thus these ranges have been expanded by adding the strain-rates of  $10^1 \text{ s}^{-1}$ ,  $10^0 \text{ s}^{-1}$ ,  $10^{-6} \text{ s}^{-1}$ ,  $10^{-7} \text{ s}^{-1}$  and the temperatures of  $-20^\circ\text{C}$  and  $140^\circ\text{C}$ . A side note on the temperature of  $140^\circ\text{C}$  is that this temperature is within the glass transition zone of PEEK, while the model is not fully valid within the glass transition zone. The results of this widened scope are compared with the theory of polymers introduced in chapter 2 and the original EGP model.

The model should yield results that lead to bi-linear curves for all temperatures and strain-rates in the strain-rate dependency plot as shown in 2.2a. It can be seen in Figure 4.9 that this is indeed the case for the strain-rate dependency plot at a strain of 0.4. This is the case as well for all strains after yielding.

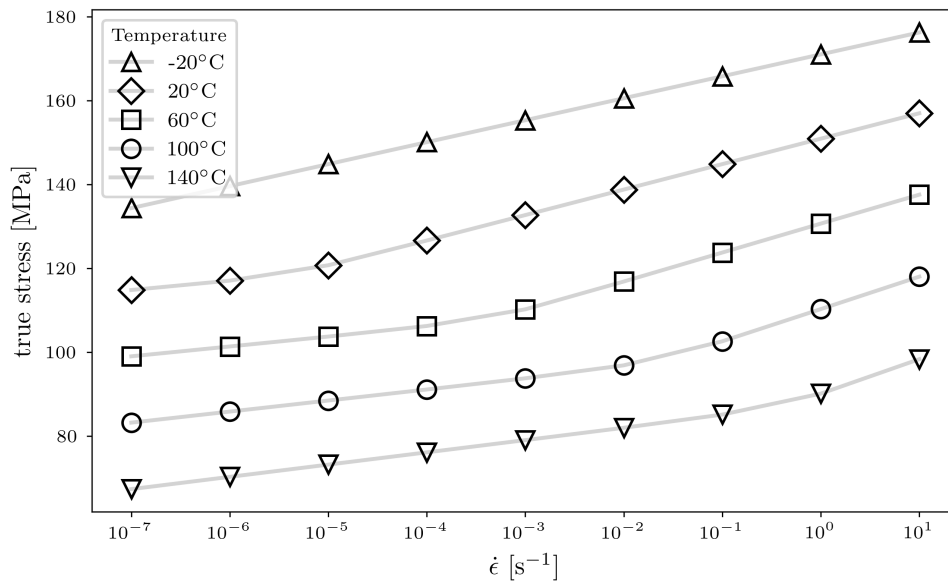


Figure 4.9: The strain-rate dependency of the updated EGP model results for the larger temperature and strain-rate range.

Appendix F shows all stress-strain curves at a strain of 0.4 for the larger strain-rate and temperature range. The strain softening effect becomes stronger at the temperature of  $-20^\circ\text{C}$  and for higher strain-rates (Figure F.1). This is in accordance with the theory of polymers [Bower, 2003].

The stress-strain results at  $140^\circ\text{C}$  (Figure F.5) show high yield stresses with a dip in stress afterwards for higher strain-rates. Barba et al. [2020] shows that this is the expected behaviour for PEEK within the glass transition zone. The original EGP model does not show this behaviour. This hints that the updated EGP model performs better than the original EGP model at  $140^\circ\text{C}$ .

The lowest strain-rates show a decrease in stress at high strains in the updated EGP model, while this is once again not observed in the original EGP model. There is no evidence that this should be the case. This effect perhaps comes from the fact that the EGP model is not fully suited to model the stresses in and beyond the glass transition zone.



## CYCLIC LOADING

---

Since the problem statement mentions long term performance testing in which cyclic loading cases for fatigue are of importance, a cyclic loading case is investigated qualitatively in this chapter in section 5.1. No experimental data is available for a cyclic loading case, thus the results are compared with available literature in section 5.2. Lastly, the results from this chapter lead together with the results from chapter 3 to the final updated EGP model in section 5.3.

The updated EGP model should perform well for all types of load cases. Tension loading is implicitly tested by running the cyclic loading cases. Furthermore, shear loading cases work with the updated EGP model but are not further discussed in this thesis.

### 5.1 THE INVARIANT FUNCTION

**REDUCING INVARIANT FUNCTION  $I_r$**  A cyclic loading test is run in which a face of the 1x1x1 cube, as described in chapter 3, is loaded in compression until a displacement of 0.6 is reached, then loaded in tension until a displacement of  $-0.6$  is reached and lastly loaded in compression until the displacement is back at the original state. The updated EGP as described in section 4.7 is used for this analysis. The stress-strain curve obtained by this test is shown in Figure 5.1. Large stress spikes occur around zero strain, which is not the expected behaviour. The stiffness of the material should remain the same around zero strain [Li et al., 2019]. The stress spikes are fully contributed to the strain-dependent Ree-Eyring parameters. The value of the invariant function  $I_r$  decreases when the strain decreases after the reversal of the loading direction, leading to a very low activation volume, activation energy and initial viscosities around zero strain.

**NON-REDUCING INVARIANT FUNCTION  $I_r$**  Figure 5.1 shows that the invariant function  $I_r$  leads to incorrect behaviour when it is always proportional to the strain and the loading direction is reversed. Two solutions proposed for this problem are:

1.  *$I_r$  is prevented from reducing:* The invariant function  $I_r$  is fully prevented from reducing. This would lead to cyclic behaviour that is dependent on the strain at which the loading direction is reversed;
2.  *$I_r$  in the  $\tanh()$  term is prevented from reducing:* Just the invariant function  $I_r$  that is used within the part related to the evolution at the low to moderate strain range cannot be reduced. This is the  $\tanh(I_r)$  term in Equations 4.11-4.13.

The difference between the two proposals is shown in Figure 5.2a for the activation volume but is also valid for the evolution of the activation energy and initial viscosities. The figure shows for the first proposal that the activation volume keeps the value it has at the strain at which the loading direction is reversed. The figure

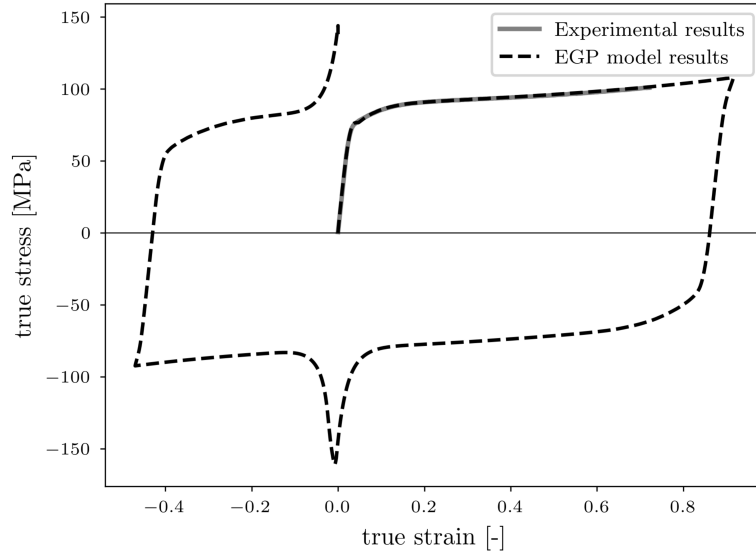


Figure 5.1: The stress-strain graph of a cyclic loading case with the updated EGP model as described in section 4.7 with a strain-rate of  $10^{-3} \text{ s}^{-1}$  and at  $100^\circ\text{C}$ .

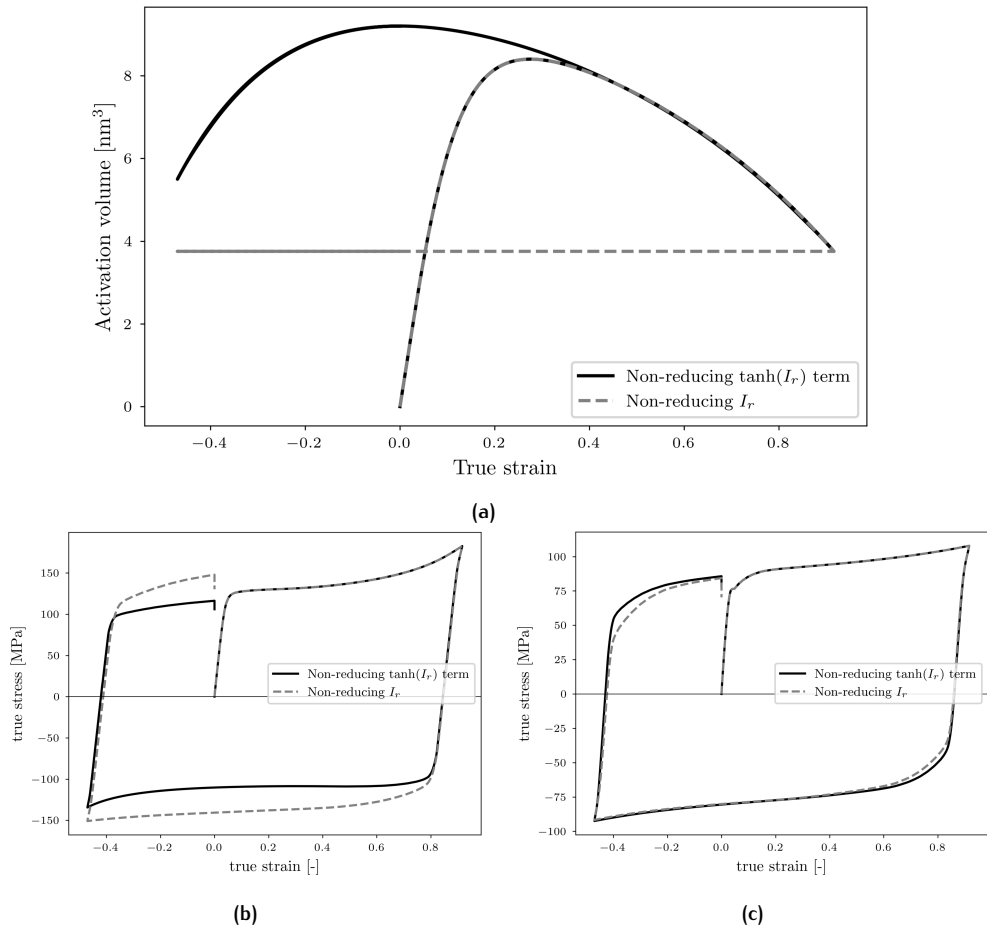


Figure 5.2: (a) The activation volume and cyclic stress-strain curves at (b)  $20^\circ\text{C}$  and (c)  $100^\circ\text{C}$  for 2 different proposals:  $I_r$  is prevented from reducing (Non-reducing  $I_r$ ) and  $I_r$  in  $\tanh()$  term is prevented from reducing (Non-reducing  $\tanh(I_r)$  term).

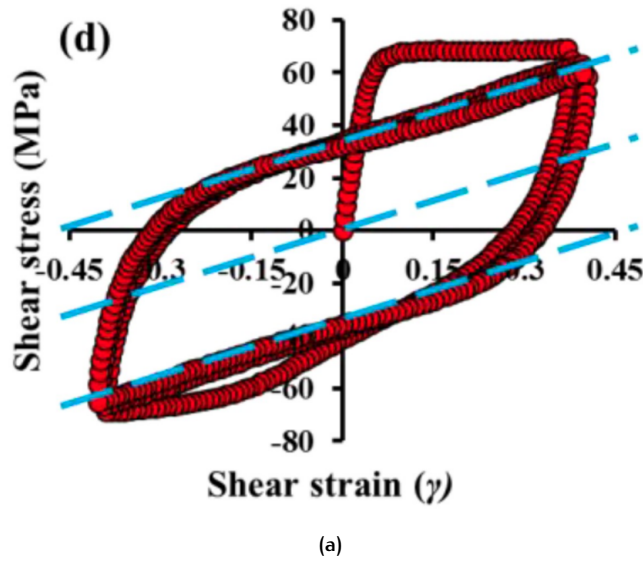


Figure 5.3: "Constant strain-rate saw-tooth fully-reversed cyclic loading of PEEK in shear" with a strain-rate of  $10^{-3} \text{ s}^{-1}$  and at  $20^\circ\text{C}$ , taken from Li et al. [2019].

shows for the second proposal that only the quadratic part of these equations can recover when the loading direction is reversed.

Figures 5.2b and 5.2c show the cyclic stress-strain behaviour at respectively  $20^\circ\text{C}$  and  $100^\circ\text{C}$  for both proposals. Hardening behaviour in tension is only seen in Figure 5.2b for the proposal in which the invariant function in the  $\tanh()$  term is prevented from reducing. This is because the viscous hardening stress decreases again with a reversal of loading direction. Hardening behaviour is expected to occur again in tension, thus the proposal where the invariant function is always prevented from reducing seems to lead to incorrect results. The behaviour at  $100^\circ\text{C}$  is almost the same for both proposals. No conclusion can be drawn on which proposal behaves better without experimental data on the same cyclic loading case at  $100^\circ\text{C}$ .

In this thesis, the choice is made to apply the proposal where the invariant function in the  $\tanh()$  term is prevented from reducing in the EGP model due to the expected non-constant viscous hardening behaviour after reversal of the loading direction [Senden et al., 2010]. However, the proposal should be verified with experimental data. Equations 4.11-4.13 and 4.9 are updated as shown for the activation volume below:

$$V_\alpha = (V_{const,\alpha} - C_{V,1,\alpha}) + C_{V,1,\alpha} \cdot \tanh(C_{V,2,\alpha} \cdot (I_{r,non} - C_{V,3,\alpha})) + C_{V,4,\alpha} I_r^2 \quad (5.1)$$

Where:

$$I_{r,non}(t_n) \geq I_{r,non}(t_{n-1}) \quad (5.2)$$

## 5.2 COMPARISON WITH LITERATURE

**STIFFNESS REDUCTION** Li et al. [2019] shows experimental data on cyclic loading of PEEK at  $20^\circ\text{C}$  and a strain-rate of  $10^{-3} \text{ s}^{-1}$ . This experimental data shows a strong decrease of stiffness after the first reversal of loading, as seen in Figure 5.3a taken from Li et al. [2019]. This decrease in stiffness is dependent on the strain level where the reversal of loading takes place. The updated EGP model does not show this decrease in stiffness (see Figure 5.4b with Ree-Eyring parameters evolution). Thus it is concluded that this effect is not correctly implemented in the EGP model.

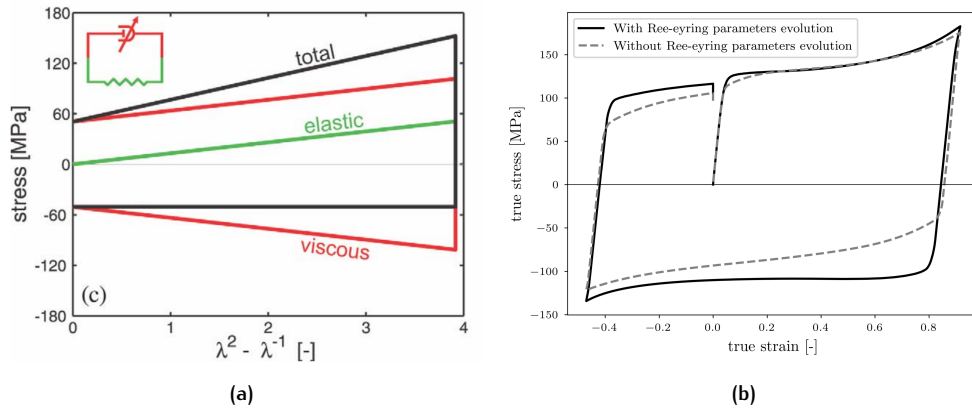


**Figure 5.4:** (a) The schematic influence of the viscous hardening stress, taken from Senden et al. [2010]. (b) The stress-strain graph of a cyclic loading case with the original and updated EGP model at 20°C and a strain-rate of  $10^{-3} \text{ s}^{-1}$ . The  $I_r$  in the  $\tanh()$  term of the evolution of the Ree-Eyring parameters is prevented from reducing. The elastic strain hardening parameters are increased to  $G_r = 7$  and  $\alpha = 0.32$  for the original EGP model to create a useful visual representation of the elastic strain hardening behaviour.

**THE BAUSCHINGER EFFECT** The Bauschinger effect is the change of material behaviour/parameters when stresses are present in the material or when they have been before. This is the case for cyclic loading where the loading direction is changed when stresses are present in the material. Experimentally it is seen that the tensile part of the curve is not parallel to the compressive part of the curve for cyclic loading of PEEK [Senden et al., 2010]. This indicates that the hardening is not fully elastic, which is the influence of the Bauschinger effect.

Senden et al. [2010] argues that viscous strain hardening should be included in the EGP model to correctly model the Bauschinger effect. The contribution of viscous strain hardening is shown with the red curve in Figure 5.4a. This viscous strain hardening contribution is added to the elastic contribution (green line) to get the total hardening stress (black line). Senden et al. [2012a] expanded on the idea of including viscous strain hardening and made the activation energy and initial viscosities for the  $\alpha$ -process quadratic dependent on the invariant function (Equation 2.24) and the  $\beta$ -process linearly dependent on the invariant function. Wendlandt et al. [2005] included viscous strain hardening by including a strain-dependent activation volume that is linearly dependent on the actual state of deformation.

This thesis concludes that all three Ree-Eyring parameters should be dependent on the strain in a quadratic way for large strains for both the  $\alpha$ - and  $\beta$ -process. The updated EGP model is run with and without the evolving Ree-Eyring parameters to investigate if viscous strain hardening is present. Figure 5.4b shows that there is only elastic strain hardening by using constant Ree-Eyring parameters. This can be concluded from the parallel response of the compressive and tensile parts of the curve. Including the evolution of the Ree-Eyring parameters shows that the Bauschinger effect is captured very well.

### 5.3 THE FULLY UPDATED EGP MODEL

The results from this chapter lead together with the results from chapter 4 to the fully updated EGP model. The following changes are made to the original EGP model to obtain the fully updated EGP model:

- The viscosity function is updated to Equation 4.8;
- The activation volume, activation energy, initial viscosities and shear moduli are made strain-dependent with functions 4.11-4.16 and 4.9 in which the invariant function  $I_r$  in the  $\tanh()$  term is prevented from reducing as defined in Equations 5.1 and 5.2.

The implementation of these changes in the stress calculation is shown in Appendix E.



## LINEARIZATION

Chapters 4 and 5 lead to the updated EGP model. The differences with the original EGP model are listed in section 5.3.

Besides this, there is an **original** linearization and a **updated** linearization of the stiffness tensor. This stiffness tensor consists of four parts, while only three parts are included in the original linearization. The updated linearization is derived in sections 6.1 and 6.2. It will include both this fourth part and all needed changes to account for the updated EGP model.

It should be clearly noted that running the updated EGP model is not analogous to using the updated linearization. For example, the updated EGP model can also be run with the original linearization.

Lastly, the convergence rate is shown for the original and the updated EGP model combined with both the original and updated linearization in section 6.3.

Please note the following notation for the subscripts in this chapter: the process is denoted by  $x = \alpha$  or  $\beta$ , the number of  $\alpha$ -modes is denoted by  $j$ , the number of  $\beta$ -modes is denoted by  $k$  and the total number of modes is denoted by  $i (= j + k)$ .

**STIFFNESS TENSOR DECOMPOSITION** The total stiffness tensor of the EGP model is calculated as follows:

$${}^4\mathbf{K}_{tot} = -{}^4\mathbf{I}^T \cdot \sigma + {}^4\mathbf{S} : \mathbf{F}^T \quad (6.1)$$

The fourth order identity tensor  ${}^4\mathbf{I}$ , the stress tensor  $\sigma$  and the deformation gradient  $\mathbf{F}$  are already known. The stiffness tensor  ${}^4\mathbf{S}$  is unknown and can be additively split in 4 parts

$${}^4\mathbf{S} = {}^4\mathbf{S}_h + {}^4\mathbf{S}_r + {}^4\mathbf{S}_d + {}^4\mathbf{S}_x \quad (6.2)$$

related to the hydrostatic stress, hardening stress, deviatoric stress and the state variables, respectively. The state variable stiffness tensor is not included in the original linearization but is included in the updated linearization.

The viscosity function is updated in the updated EGP model and new functions are implemented for the Ree-Eyring parameters and the shear moduli. The evolution of the Ree-Eyring parameters is included in the state variable stiffness tensor  ${}^4\mathbf{S}_x$ . The evolution of the shear moduli is included in both the state variable stiffness tensor  ${}^4\mathbf{S}_x$  and the deviatoric stiffness tensor  ${}^4\mathbf{S}_d$ . The deviatoric stiffness tensor  ${}^4\mathbf{S}_d$  and the state variable stiffness tensor  ${}^4\mathbf{S}_x$  are derived in the following two sections, respectively.

## 6.1 DEVIATORIC STIFFNESS TENSOR ${}^4\mathbf{S}_d$

The deviatoric stiffness tensor  ${}^4\mathbf{S}_d$  is computed by taking the derivative of the driving stress  $\sigma_s$  (Equation 2.9) with respect to the deformation gradient  $\mathbf{F}$ :

$$\frac{\partial \sigma_s}{\partial \mathbf{F}} = \sum_{j=1}^n \left( G_{\alpha,j} \frac{\partial \tilde{\mathbf{B}}_{e_{\alpha,j}}^d}{\partial \mathbf{F}} + \tilde{\mathbf{B}}_{e_{\alpha,j}}^d \frac{\partial G_{\alpha,j}}{\partial \mathbf{F}} \right) + \sum_{k=1}^m \left( G_{\beta,k} \frac{\partial \tilde{\mathbf{B}}_{e_{\beta,k}}^d}{\partial \mathbf{F}} + \tilde{\mathbf{B}}_{e_{\beta,k}}^d \frac{\partial G_{\beta,k}}{\partial \mathbf{F}} \right) \quad (6.3)$$

The first term is already derived in Clarijs [2017] and will not be expanded upon. The second term is new because the shear moduli  $G_{x,i}$  (Equation 4.9) are dependent on the deformation gradient  $\mathbf{F}$  in the updated EGP model:

$$\frac{\partial G_{x,j}}{\partial \mathbf{F}} = -G_{const,x,i} E_{G,x} \frac{\partial I_{r,non}}{\partial \mathbf{F}} \quad (6.4)$$

Where  $E_{G,\alpha}$  and  $E_{G,\beta}$  are introduced:

$$E_{G,\alpha} = C_{G,1,\alpha} C_{G,2,\alpha} \cdot \text{sech}^2(C_{G,2,\alpha} \cdot (I_{r,non} - C_{G,3,\alpha})) \quad (6.5)$$

$$E_{G,\beta} = 0 \quad (6.6)$$

This form will be used for all parameters that evolve over the strain within the updated EGP model.

The derivative of the invariant function  $I_r = \sqrt{\frac{1}{3}I_1^2 - I_2}$  (Equation 2.24) with respect to the deformation gradient  $\mathbf{F}$  is elaborated as:

$$\frac{\partial I_r}{\partial \mathbf{F}} = \frac{1}{2I_r} \left( \frac{2}{3}I_1 \frac{\partial I_1}{\partial \mathbf{F}} - \frac{\partial I_2}{\partial \mathbf{F}} \right) \quad (6.7)$$

In which:

$$\frac{\partial I_1}{\partial \mathbf{F}} = \mathbf{I} : \frac{\partial \tilde{\mathbf{B}}}{\partial \mathbf{F}} \quad (6.8)$$

$$\frac{\partial I_2}{\partial \mathbf{F}} = \text{tr}(\tilde{\mathbf{B}}) \cdot \mathbf{I} : \frac{\partial \tilde{\mathbf{B}}}{\partial \mathbf{F}} - \frac{1}{2} \left( {}^4\mathbf{I}^T : \frac{\partial \tilde{\mathbf{B}}}{\partial \mathbf{F}} : \tilde{\mathbf{B}} + \tilde{\mathbf{B}}^T : \frac{\partial \tilde{\mathbf{B}}}{\partial \mathbf{F}} \right) \quad (6.9)$$

The non-reducing invariant function  $I_{r,non}$  is defined the same as the invariant function  $I_r$  but has the requirement that  $I_{r,non}(t_n) \geq I_{r,non}(t_{n-1})$ . This means the following for the derivative of  $I_{r,non}$ :

$$\begin{cases} \frac{\partial I_{r,non}}{\partial \mathbf{F}} = \frac{1}{2I_{r,non}} \left( \frac{2}{3}I_1 \frac{\partial I_1}{\partial \mathbf{F}} - \frac{\partial I_2}{\partial \mathbf{F}} \right), & \text{if } I_{r,non}(t_n) > I_{r,non}(t_{n-1}) \\ \frac{\partial I_{r,non}}{\partial \mathbf{F}} = 0, & \text{otherwise} \end{cases} \quad (6.10)$$

The isochoric Cauchy-Green deformation tensor  $\tilde{\mathbf{B}}$  can be derived in the same way as the elastic variant in Equation 2.7 and is expanded with Equation 2.6:

$$\tilde{\mathbf{B}} = \tilde{\mathbf{F}} \cdot \tilde{\mathbf{F}}^T = J^{-\frac{2}{3}} \mathbf{F} \cdot \mathbf{F}^T \quad (6.11)$$

Next, its derivative with respect to the deformation gradient is derived:

$$\begin{aligned} \frac{d\tilde{\mathbf{B}}}{d\mathbf{F}} &= \frac{\partial \tilde{\mathbf{B}}}{\partial J} \frac{\partial J}{\partial \mathbf{F}} + \frac{\partial \tilde{\mathbf{B}}}{\partial \mathbf{F}} \\ &= -\frac{2}{3} J^{-\frac{5}{3}} \mathbf{B} \mathbf{J} \mathbf{F}^{-T} + J^{-\frac{2}{3}} \left( {}^4\mathbf{I} \cdot \mathbf{F}^T + \mathbf{F} \cdot {}^4\mathbf{I}^T \right) \\ &= J^{-\frac{2}{3}} \left( {}^4\mathbf{I} \cdot \mathbf{F}^T + \mathbf{F} \cdot {}^4\mathbf{I}^T - \frac{2}{3} \mathbf{B} \mathbf{F}^{-T} \right) \end{aligned} \quad (6.12)$$

The derivative of the volume change ratio  $J$  with respect to the deformation gradient  $F$  has been calculated to derive the Equation 6.12:

$$J = \det(\mathbf{F}_e) = \det(\mathbf{F}) \quad (6.13)$$

$$\frac{\partial J}{\partial \mathbf{F}} = J\mathbf{F}^{-T} \quad (6.14)$$

It should be noted that this derivative was incorrectly derived and implemented in the hydrostatic stiffness tensor  ${}^4\mathbf{S}_h$ . This has been fixed for both the original and updated linearization. The influence of this mistake is very minor.

In the end, the following equation is found for the deviatoric stiffness tensor  ${}^4\mathbf{S}_d$ :

$${}^4\mathbf{S}_d = \sum_{j=1}^n \left( G_{\alpha,j} \left( {}^4\mathbf{I} - \frac{1}{3} {}^4\mathbf{II} \right) : {}^4\mathbf{B}_{\alpha,j} : {}^4\mathbf{F} - G_{const,\alpha,j} E_{G,\alpha} \frac{\partial I_{r,non}}{\partial \mathbf{F}} \tilde{\mathbf{B}}_{e_{\alpha,j}}^d \right) + \sum_{k=1}^m \left( G_{\beta,k} \left( {}^4\mathbf{I} - \frac{1}{3} {}^4\mathbf{II} \right) : {}^4\mathbf{B}_{\beta,k} : {}^4\mathbf{F} - G_{const,\beta,k} E_{G,\beta} \frac{\partial I_{r,non}}{\partial \mathbf{F}} \tilde{\mathbf{B}}_{e_{\beta,k}}^d \right) \quad (6.15)$$

Where the definitions of the tensors  ${}^4\mathbf{B}_{x,i}$  and  ${}^4\mathbf{F}$  in the first term of both sums can be found in Clarijs [2017].

## 6.2 STATE VARIABLE STIFFNESS TENSOR ${}^4\mathbf{S}_x$

The state variables are the modal plasticity parameters  $\lambda_{x,i}$  and the equivalent plastic strain  $\tilde{\gamma}_p$ . They are used within the iterative stress calculation which is included in the EGP model. The stiffness tensor is dependent on these state variables since they are dependent on the deformation gradient  $F$  and determine the driving stress. This is shown in the following equation where  $x = [\lambda_{\alpha,1}, \dots, \lambda_{\alpha,j}, \lambda_{\beta,1}, \dots, \lambda_{\beta,k}, \tilde{\gamma}_p]$ :

$${}^4\mathbf{S}_x = \frac{\partial \sigma_s}{\partial x} \frac{\partial x}{\partial \mathbf{F}} \quad (6.16)$$

The following system of equations is solved for the iterative stress calculation:

$$\Phi = \begin{cases} f_{x,i} = \lambda_{x,i}(t_{n+1}) \cdot (\Delta t \Gamma_{x,i}(t_{n+1}) + 1) = 1 \\ g = \tilde{\gamma}_p(t_{n+1}) - \Delta t \dot{\tilde{\gamma}}_p(t_{n+1}) = \tilde{\gamma}_p(t_n) \end{cases} \quad (6.17)$$

Where  $\Gamma_{x,i} = \frac{G_{x,i}}{\eta_{x,i}}$ ,  $\Delta t$  is the time-step from a Backward Euler scheme used within the stress calculation and  $\dot{\tilde{\gamma}}_p$  is defined in Equation 2.19. The stiffness tensor is calculated when the iterative stress calculation is converged. This means that the following holds:

$$\begin{aligned} \frac{d\Phi}{d\mathbf{F}} &= \frac{\partial \Phi}{\partial \mathbf{F}} + \frac{\partial \Phi}{\partial x} \frac{\partial x}{\partial \mathbf{F}} \\ 0 &= \frac{\partial \Phi}{\partial \mathbf{F}} + \frac{\partial \Phi}{\partial x} \frac{\partial x}{\partial \mathbf{F}} \\ \frac{\partial x}{\partial \mathbf{F}} &= - \left( \frac{\partial \Phi}{\partial x} \right)^{-1} \frac{\partial \Phi}{\partial \mathbf{F}} \end{aligned} \quad (6.18)$$

This solution is substituted in Equation 6.16:

$${}^4\mathbf{S}_x = - \frac{\partial \sigma_s}{\partial x} \left( \frac{\partial \Phi}{\partial x} \right)^{-1} \frac{\partial \Phi}{\partial \mathbf{F}} \quad (6.19)$$

The derivative  $\frac{\partial \Phi}{\partial x}$  is already known since it is used within the stress calculation [Clarijs, 2017]. The derivatives  $\frac{\partial \sigma_s}{\partial x}$  and  $\frac{\partial \Phi}{\partial \mathbf{F}}$  are unknown and derived in this section. Both derivatives are split up as shown below:

$$\begin{array}{ccc} \frac{\partial \sigma_s}{\partial x} & \rightarrow & \frac{\partial \sigma_s}{\partial \tilde{\gamma}_p} \\ & & \frac{\partial \sigma_s}{\partial \lambda_{x,i}} \\ \frac{\partial \Phi}{\partial \mathbf{F}} & \rightarrow & \frac{\partial f_{x,i}}{\partial \mathbf{F}} \\ & & \frac{\partial g}{\partial \mathbf{F}} \end{array}$$

The four derivatives on the right are derived in the four paragraphs in this section.

#### DERIVATIVE DRIVING STRESS WITH RESPECT TO THE EQUIVALENT PLASTIC STRAIN

The driving stress is not dependent on the equivalent plastic strain  $\tilde{\gamma}_p$ , thus the derivative of the driving stress with respect to the equivalent plastic strain is:

$$\frac{\partial \sigma_s}{\partial \tilde{\gamma}_p} = 0 \quad (6.20)$$

#### DERIVATIVE DRIVING STRESS WITH RESPECT TO THE PLASTICITY PARAMETERS

The driving stress is dependent on the plasticity parameters  $\lambda_{x,i}$  as seen in the following equation:

$$\begin{aligned} \frac{\partial \sigma_s}{\partial \lambda_{x,i}} &= \sum_{j=1}^n \left( G_{\alpha,j} \frac{\partial \tilde{\mathbf{B}}_{e_{\alpha,j}}^d}{\partial \lambda_{x,i}} \right) + \sum_{k=1}^m \left( G_{\beta,k} \frac{\partial \tilde{\mathbf{B}}_{e_{\beta,k}}^d}{\partial \lambda_{x,i}} \right) \\ &= \sum_{j=1}^n \left( G_{\alpha,j} \left( {}^4\mathbf{I} - \frac{1}{3} \mathbf{II} \right) \frac{\partial \tilde{\mathbf{B}}_{e_{\alpha,j}}}{\partial \lambda_{x,i}} \right) + \sum_{k=1}^m \left( G_{\beta,k} \left( {}^4\mathbf{I} - \frac{1}{3} \mathbf{II} \right) \frac{\partial \tilde{\mathbf{B}}_{e_{\beta,k}}}{\partial \lambda_{x,i}} \right) \end{aligned} \quad (6.21)$$

The plastic part of the right Cauchy-Green deformation tensor  $\mathbf{C}_p$  is defined below:

$$\begin{aligned} \mathbf{C}_p &= \mathbf{F}_p^T \cdot \mathbf{F}_p \\ &= \tilde{\mathbf{F}}^T \cdot \tilde{\mathbf{B}}_e^{-1} \cdot \tilde{\mathbf{F}} \end{aligned} \quad (6.22)$$

The plastic right Cauchy Green deformation tensor  $\mathbf{C}_p$  is in the stress calculation updated using the plasticity parameters  $\lambda_{x,i}$ :

$$\mathbf{C}_p(t_{n+1}) = (1 - \lambda_{x,i}) \cdot \tilde{\mathbf{C}}(t_{n+1}) + \lambda_{x,i} \cdot \mathbf{C}_p(t_n) \quad (6.23)$$

Equations 6.22 and 6.23 are used to calculate the derivative of the isochoric, elastic left Cauchy-Green deformation tensor with respect to the plasticity parameters  $\frac{\partial \tilde{\mathbf{B}}_{e_{\alpha,j}}}{\partial \lambda_{x,i}}$  (for the alpha process):

$$\begin{aligned} \frac{\partial \tilde{\mathbf{B}}_{e_{\alpha,j}}}{\partial \lambda_{x,i}} &= \tilde{\mathbf{F}} \cdot \frac{\partial \mathbf{C}_{p_{\alpha,j}}^{-1}}{\partial \lambda_{x,i}} \cdot \tilde{\mathbf{F}}^T \\ &= -\tilde{\mathbf{F}} \cdot \mathbf{C}_{p_{\alpha,j}}^{-1} \cdot \frac{\partial \mathbf{C}_{p_{\alpha,j}}}{\partial \lambda_{x,i}} \cdot \mathbf{C}_{p_{\alpha,j}}^{-1} \cdot \tilde{\mathbf{F}}^T \end{aligned} \quad (6.24)$$

$$\begin{aligned} \frac{\partial \mathbf{C}_{p_{\alpha,j}}}{\partial \lambda_{x,i}} &= \delta_{ji} \cdot \mathbf{C}_{p_{\alpha,j}}(t_n) - \tilde{\mathbf{C}}(t_{n+1}) \\ \frac{\partial \mathbf{C}_{p_{\alpha,j}}}{\partial \lambda_{x,j}} &= \mathbf{C}_{p_{\alpha,j}}(t_n) - \tilde{\mathbf{C}}(t_{n+1}) \end{aligned} \quad (6.25)$$

All derived derivatives can be substituted in Equation 6.21 where the following tensor is introduced  $\mathbf{M} = \tilde{\mathbf{F}} \cdot \mathbf{C}_{p_{x,i}}^{-T} = \tilde{\mathbf{F}} \cdot \mathbf{C}_{p_{x,i}}^{-1}$ :

$$\begin{aligned}
\frac{\partial \sigma_s}{\partial \lambda_{x,i}} &= \sum_{i=1}^n G_{x,i} \left( {}^4\mathbf{I} - \frac{1}{3} \mathbf{II} \right) \frac{\partial \tilde{\mathbf{B}}_{e_{x,i}}}{\partial \lambda_{x,i}} \\
&= \sum_{i=1}^n -G_{x,i} \left( {}^4\mathbf{I} - \frac{1}{3} \mathbf{II} \right) : \left[ \tilde{\mathbf{F}} \cdot \mathbf{C}_{p_{\alpha,j}}^{-1} \cdot \frac{\partial \mathbf{C}_{p_{\alpha,j}}}{\partial \lambda_{x,i}} \cdot \mathbf{C}_{p_{\alpha,j}}^{-1} \cdot \tilde{\mathbf{F}}^T \right] \\
&= \sum_{i=1}^n -G_{x,i} \left( {}^4\mathbf{I} - \frac{1}{3} \mathbf{II} \right) : \left[ \mathbf{M} \cdot \left( \mathbf{M} \cdot \left( \frac{\partial \mathbf{C}_{p_{\alpha,j}}}{\partial \lambda_{x,i}} \right)^T \right)^T \right] \\
&= \sum_{i=1}^n -G_{x,i} \left( {}^4\mathbf{I} - \frac{1}{3} \mathbf{II} \right) : \left[ \mathbf{M} \cdot {}^4\mathbf{I}^T : \left( \mathbf{M} \cdot \left( \frac{\partial \mathbf{C}_{p_{\alpha,j}}}{\partial \lambda_{x,i}} \right)^T \right) \right] \\
&= \sum_{i=1}^n -G_{x,i} \left( {}^4\mathbf{I} - \frac{1}{3} \mathbf{II} \right) : \left[ \mathbf{M} \cdot \left( {}^4\mathbf{I}^T \cdot \mathbf{M} \right) : \left( \frac{\partial \mathbf{C}_{p_{\alpha,j}}}{\partial \lambda_{x,i}} \right)^T \right] \\
&= \sum_{i=1}^n G_{x,i} \left( {}^4\mathbf{I} - \frac{1}{3} \mathbf{II} \right) : \left[ {}^4\tilde{\mathbf{A}}_{x,i}^{(2)} : \left( \mathbf{C}_{p_{x,i}}(t_n) - \tilde{\mathbf{C}}(t_{n+1}) \right)^T \right]
\end{aligned} \tag{6.26}$$

${}^4\tilde{\mathbf{A}}_{x,i}^{(2)}$  is a tensor that is also used for computing the deviatoric stiffness tensor  ${}^4\mathbf{S}_d$ .

**DERIVATIVE  $f_{x,i}$  WITH RESPECT TO THE DEFORMATION GRADIENT**  $f_{x,i}$  is firstly differentiated with respect to the deformation gradient:

$$f_{x,i} = \lambda_{x,i} \cdot (\Gamma_{x,i} \Delta t + 1) = \lambda_{x,i} \cdot \left( \frac{G_{x,i}}{\eta_{x,i}} \Delta t + 1 \right) \tag{6.27}$$

$$\frac{\partial f_{x,i}}{\partial \mathbf{F}} = -\frac{\lambda_{x,i} \Delta t}{\eta_{x,i}} \left( G_{const,x,i} E_{G,x} \frac{\partial I_{r,non}}{\partial \mathbf{F}} + \Gamma_{x,i} \frac{\partial \eta_{x,i}}{\partial \mathbf{F}} \right) \tag{6.28}$$

The derivative of the invariant function  $\frac{\partial I_{r,non}}{\partial \mathbf{F}}$  is shown in Equation 6.10 and the derivative of the viscosity function with respect to the deformation gradient is as follows:

$$\frac{\partial \eta_{x,i}}{\partial \mathbf{F}} = \eta_{x,i} \left[ \frac{\mu_x}{\tau_{0,x}} \frac{\partial p}{\partial \mathbf{F}} + \left( \frac{1}{\bar{\tau}_x} - \frac{\coth\left(\frac{\bar{\tau}_x}{\tau_{0,x}}\right)}{\tau_{0,x}} \right) \frac{\partial \bar{\tau}_x}{\partial \mathbf{F}} + M_{x,low} \frac{\partial I_{r,non}}{\partial \mathbf{F}} + M_{x,high} \frac{\partial I_r}{\partial \mathbf{F}} \right] \tag{6.29}$$

Where for  $d = low$  or  $high$ ,  $x = \alpha$  or  $\beta$  and  $k = \eta$ ,  $\Delta H$  or  $V$ :

$$\begin{aligned}
M_{x,d} &= E_{\eta,x,d} + \frac{E_{\Delta H,x,d}}{R} \left( \frac{1}{T} - \frac{1}{T_{x,base}} \right) + \frac{\mu_x p E_{V,x,d}}{k_B T} - \\
&\quad \frac{E_{V,x,d} \tau_{0,x}}{k_B T} \left( \frac{\bar{\tau}_x \coth\left(\frac{\bar{\tau}_x}{\tau_{0,x}}\right)}{\tau_{0,x}} - 1 \right)
\end{aligned} \tag{6.30}$$

$$E_{k,\alpha,low} = C_{k,1,\alpha} C_{k,2,\alpha} \cdot \operatorname{sech}^2(C_{k,2,\alpha} \cdot (I_{r,non} - C_{k,3,\alpha})) \tag{6.31}$$

$$E_{k,\alpha,high} = C_{k,4,\alpha} 2I_r \tag{6.32}$$

$$E_{k,\beta,low} = 0 \quad (6.33)$$

$$E_{k,\beta,high} = C_{k,4,\beta} 2I_r \quad (6.34)$$

The derivation of Equations 6.29 to 6.34 is shown in Appendix G.

The derivative of the total equivalent stress (Equation 2.14 with respect to the deformation gradient  $\frac{\partial \bar{\tau}_x}{\partial \mathbf{F}}$  and the derivative of the pressure (Equation 2.15) with respect to the deformation gradient  $\frac{\partial p}{\partial \mathbf{F}}$  in Equation 6.29 are still unknown. The former is computed first:

$$\frac{\partial \bar{\tau}_x}{\partial \mathbf{F}} = \frac{1}{4\bar{\tau}_x} \left( \sigma_{s_x} : \frac{\partial \sigma_{s_x}}{\partial \mathbf{F}} + \frac{\partial \sigma_{s_x}}{\partial \mathbf{F}} : \sigma_{s_x} \right) \quad (6.35)$$

$\frac{\partial \sigma_{s_x}}{\partial \mathbf{F}}$  is here either the sum over the  $\alpha$  or  $\beta$  part in Equation 6.15.

The last partial derivative in Equation 6.29 is computed from the definition of the pressure (Equation 2.15) and Equation 6.14:

$$\frac{\partial p}{\partial \mathbf{F}} = -\kappa \frac{\partial J}{\partial \mathbf{F}} = -\kappa J \mathbf{F}^{-T} \quad (6.36)$$

**DERIVATIVE  $g$  WITH RESPECT TO THE DEFORMATION GRADIENT**  $g$  is differentiated with respect to the deformation gradient:

$$g = \bar{\gamma}_p - \dot{\bar{\gamma}}_p \Delta t = \bar{\gamma}_p - \frac{\bar{\tau}_{\alpha,1}}{\eta_{\alpha,1}} \Delta t \quad (6.37)$$

$$\frac{\partial g}{\partial \mathbf{F}} = -\Delta t \left( \frac{1}{\eta_{\alpha,1}} \frac{\partial \bar{\tau}_{\alpha,1}}{\partial \mathbf{F}} - \frac{\bar{\tau}_{\alpha,1}}{\eta_{\alpha,1}^2} \frac{\partial \eta_{\alpha,1}}{\partial \mathbf{F}} \right) \quad (6.38)$$

$\frac{\partial \eta_{\alpha,1}}{\partial \mathbf{F}}$  is shown in Equation 6.29 and  $\frac{\partial \bar{\tau}_{\alpha,1}}{\partial \mathbf{F}}$  is very similar to Equation 6.35:

$$\frac{\partial \bar{\tau}_{\alpha,1}}{\partial \mathbf{F}} = \frac{1}{4\bar{\tau}_{\alpha,1}} \left( \sigma_{s_{\alpha,1}} : \frac{\partial \sigma_{s_{\alpha,1}}}{\partial \mathbf{F}} + \frac{\partial \sigma_{s_{\alpha,1}}}{\partial \mathbf{F}} : \sigma_{s_{\alpha,1}} \right) \quad (6.39)$$

Lastly,  $\frac{\partial \sigma_{s_{\alpha,1}}}{\partial \mathbf{F}}$  is computed in the same way as Equation 6.15:

$$\frac{\partial \sigma_{s_{\alpha,1}}}{\partial \mathbf{F}} = G_{\alpha,1} \left( {}^4\mathbf{I} - \frac{1}{3} \mathbf{II} \right) : {}^4\mathbf{B}_{\alpha,1} : {}^4\mathbf{F} - G_{const,\alpha,1} E_{G,\alpha} \frac{\partial I_{r,non}}{\partial \mathbf{F}} \tilde{\mathbf{B}}_{e_{\alpha,1}}^d \quad (6.40)$$

### 6.3 CONVERGENCE RATE

The ultimate goal of creating the updated linearization is having a higher convergence rate and increased calculation speed. The influence of the updated linearization on the original EGP model is also investigated since the state variable stiffness tensor  ${}^4\mathbf{S}_x$  was not included in the implementation of the original EGP model and the model should still perform well when there is no evolution of parameters used.

**IMPLEMENTATION** The implementation of the calculation of the stiffness tensor in the C++ code is shown in appendix H. A second order tensor representation of fourth order tensors is used in the largest part of this implementation [TUE, 2010], while the calculation of Equation 6.19 is performed using the tensor notation from *live* because third order tensors are used for this computation [Dynaflow Research Group, 2020].

**CONVERGENCE RATE INVESTIGATION** Determining the run-time of an analysis and comparing it to another analysis is very hard since the run-time is influenced by other processes running on that computer. It is possible to purely investigate the number of iterations, but this can also lead to incorrect conclusions. This is because of the iterative stress calculation that is included in the EGP model. A large step-size will lead to few iterations but can take a lot of time due to this iterative stress calculation. This is why a combination of run-time and number of iterations is used to reach the best conclusion. An average of at least five analyses is always taken for the run-time.

**STIFFNESS CALCULATION RUN-TIME** Calculating the updated linearization naturally takes longer than the original linearization since the state variable stiffness tensor part is included. Running the calculation of the stiffness tensor 1000 times takes 0.026 seconds on average for the original linearization and 0.047 seconds on average for the updated linearization. This shows that the calculation of the updated stiffness tensor takes on average 81% longer. This does not mean that the total run-time is longer since this longer stiffness calculation can be counteracted with a faster convergence due to the more accurate stiffness tensor.

**INFLUENCING FACTORS** Multiple factors influence the total run-time and number of iterations of an analysis with the EGP model and have been varied to investigate their influence. The resulting total run-time and number of iterations for these variations can be seen in Tables 6.1 to 6.4. The same analysis as described in section 3.2 is run to obtain these values. The factors that are varied and their influence are as follows:

- *Temperature*: Changing the temperature does not lead to any large differences in the run-time or number of iterations. This is the expected behaviour;
- *Strain-rate*: Changing the strain-rate does generally not lead to any large difference in the run-time or number of iterations as can be seen in Tables 6.1 to 6.4. This is the expected behaviour;
- *MNR/FNR*: Using either the Modified Newton-Raphson (MNR) or the Full Newton-Raphson (FNR) iteration scheme does not lead to differences while making an analysis with the original linearization and the original EGP model. But fewer iterations are needed if an analysis with either or both the updated linearization or the updated EGP model is run using the FNR iteration scheme. The state variables and invariant function are updated each iteration, thus the FNR iteration scheme leads to a more accurate stiffness tensor between iterations. The state variables and the invariant function are not included in the original linearization and original EGP model. Thus, almost no difference is seen here;
- *Original/Updated EGP model*: The number of iterations and run-time are almost the same for the original and updated EGP model as can be seen if Tables 6.1 and 6.2 are compared to Tables 6.3 and 6.4;
- *Original/Updated linearization*: A large difference in the run-time and the number of iterations is observed between making an analysis with the updated linearization compared to the original linearization. This difference is highly influenced by using either a fixed step-size or adaptive stepping as discussed in the following paragraph;
- *Step-size (range)*: Calculations can be run with a fixed step-size or with an adaptive step-size range. This is of great influence for the number of iterations as can be seen if Tables 6.1 and 6.2 or Tables 6.3 and 6.4 are compared to each other.

**ORIGINAL LINEARIZATION VERSUS UPDATED LINEARIZATION** The updated linearization should yield fewer iterations and need a lower run-time compared to the original linearization because including the state variable stiffness tensor should lead to a more accurate stiffness tensor.

Table 6.1 shows the number of iterations and run-time of the original EGP model with a fixed step size. Table 6.1a shows that the number of iterations increases with the updated linearization while Table 6.1b shows that the total run-time stays approximately the same. The reason that the run-time is the same even if the number of iterations is different could be due to faster convergence of the iterative stress calculation. This could also be the reason that the MNR and FNR iteration schemes take approximately the same amount of time.

Table 6.2 also shows the number of iterations and run-time for the original EGP model, but now with an adaptive step size. A large improvement is seen if adaptive stepping is used with the updated linearization. Table 6.2a shows a decrease in the total number of iterations of 26% on average for the MNR iteration scheme and 39% on average for the FNR iteration scheme. Table 6.2b shows a decrease in the total run-time of 20% on average for the MNR iteration scheme and 23% on average for the FNR iteration scheme.

The updated linearization has a faster convergence rate for the small strain range in all cases ( $\epsilon < 0.1$ ). The reason that more iterations are needed for the case shown in table 6.1a is that the convergence rate is worse in the large strain range for the updated linearization compared to the original linearization. This becomes very visible when a fixed step-size is used. In the case of adaptive stepping, the step-size can increase fast in the small strain range with the faster convergence rate and the worse convergence rate at larger strains has almost no influence on the number of iterations because of the large step-size. This leads to the fewer number of iterations that are shown in Table 6.2a.

The influence of the updated linearization is better in the case of the updated EGP model with a fixed step size, as seen in Table 6.3a. But further, the same observations as for the original EGP model are made for the updated EGP model in Tables 6.3 and 6.4.

The conclusion is that the updated linearization always leads to the same or better results if the run-time is investigated. However, worse results are in some cases observed when the number of iterations is investigated. This hints that the updated linearization is not fully correctly derived and/or implemented. Since the results are generally better for both the number of iterations and run-time, it is advised to always use the updated linearization within the EGP model.

**ADAPTIVE STEPPING FOR THE UPDATED EGP MODEL** Very small first steps are needed for convergence when the updated EGP model is run. This does not lead to a large number of extra steps. These small initial steps are probably needed because the fast-changing Ree-Eyring parameters lead to divergence when the first steps are too large. The small initial steps can also be seen in Tables 6.3 and 6.4.

**Table 6.1:** (a) The number of iterations and (b) run-time needed to reach a strain of 0.8 at 60°C for the original EGP model. The results are shown for a fixed step-size using either the original or updated linearization and using either the Modified Newton-Raphson (MNR) of Full Newton-Raphson (FNR) iteration scheme.

(a) The number of iterations.

<i>Original EGP model</i>		<b>Original linearization</b>		<b>Updated linearization</b>	
<b>Strain-rate</b>	<b>step-size</b>	<b>MNR</b>	<b>FNR</b>	<b>MNR</b>	<b>FNR</b>
$10^{-1} \text{ s}^{-1}$	0.01	2114	2115	2376	2509
$10^{-2} \text{ s}^{-1}$	0.1	2134	2133	2546	2398
$10^{-3} \text{ s}^{-1}$	1	2149	2147	2552	2399
$10^{-4} \text{ s}^{-1}$	10	2110	2109	2497	2379
$10^{-5} \text{ s}^{-1}$	100	2072	2068	2466	2377
Average:		2116	2114	2487	2388

(b) The average run-time over five runs.

<i>Original EGP model</i>		<b>Original linearization</b>		<b>Updated linearization</b>	
<b>Strain-rate</b>	<b>step-size</b>	<b>MNR</b>	<b>FNR</b>	<b>MNR</b>	<b>FNR</b>
$10^{-1} \text{ s}^{-1}$	0.01	5.65 s	5.63 s	5.65 s	5.64 s
$10^{-2} \text{ s}^{-1}$	0.1	5.69 s	5.66 s	5.66 s	5.66 s
$10^{-3} \text{ s}^{-1}$	1	5.66 s	5.65 s	5.67 s	5.68 s
$10^{-4} \text{ s}^{-1}$	10	5.66 s	5.65 s	5.70 s	5.66 s
$10^{-5} \text{ s}^{-1}$	100	5.66 s	5.64 s	5.65 s	5.66 s
Average:		5.66 s	5.65 s	5.67 s	5.66 s

**Table 6.2:** (a) The number of iterations and (b) run-time needed to reach a strain of 0.8 at 60°C for the original EGP model. The results are shown for a variable step-size using either the original or updated linearization and using either the Modified Newton-Raphson (MNR) of Full Newton-Raphson (FNR) iteration scheme.

(a) The number of iterations.

<i>Original EGP model</i>		<b>Original linearization</b>		<b>Updated linearization</b>	
<b>Strain-rate</b>	<b>step-size</b>	<b>MNR</b>	<b>FNR</b>	<b>MNR</b>	<b>FNR</b>
$10^{-1} \text{ s}^{-1}$	0.01-0.03	1195	1237	962	905
$10^{-2} \text{ s}^{-1}$	0.1-0.4	1195	1241	824	783
$10^{-3} \text{ s}^{-1}$	1-4	1235	1221	817	657
$10^{-4} \text{ s}^{-1}$	10-40	1089	1133	720	628
$10^{-5} \text{ s}^{-1}$	100-400	1122	1036	978	633
Average:		1168	1174	860	721

(b) The average run-time over five runs.

<i>Original EGP model</i>		<b>Original linearization</b>		<b>Updated linearization</b>	
<b>Strain-rate</b>	<b>step-size</b>	<b>MNR</b>	<b>FNR</b>	<b>MNR</b>	<b>FNR</b>
$10^{-1} \text{ s}^{-1}$	0.01-0.03	1.30 s	1.37 s	1.04 s	1.30 s
$10^{-2} \text{ s}^{-1}$	0.1-0.4	1.25 s	1.55 s	0.94 s	1.19 s
$10^{-3} \text{ s}^{-1}$	1-4	1.24 s	1.49 s	0.94 s	1.02 s
$10^{-4} \text{ s}^{-1}$	10-40	1.10 s	1.42 s	0.82 s	0.99 s
$10^{-5} \text{ s}^{-1}$	100-400	1.13 s	1.31 s	1.06 s	0.99 s
Average:		1.20 s	1.43 s	0.96 s	1.10 s

**Table 6.3:** (a) The number of iterations and (b) run-time needed to reach a strain of 0.8 at 60°C for the updated EGP model. The results are shown for a small variable step-size using either the original or updated linearization and using either the Modified Newton-Raphson (MNR) or Full Newton-Raphson (FNR) iteration scheme.

(a) The number of iterations.

<i>Updated EGP model</i>		<b>Original linearization</b>		<b>Updated linearization</b>	
<b>Strain-rate</b>	<b>step-size</b>	<b>MNR</b>	<b>FNR</b>	<b>MNR</b>	<b>FNR</b>
$10^{-1} \text{ s}^{-1}$	0.001-0.01	2119	1906	2138	2318
$10^{-2} \text{ s}^{-1}$	0.001-0.1	2443	2227	2376	2278
$10^{-3} \text{ s}^{-1}$	0.001-1	2361	2193	2372	2164
$10^{-4} \text{ s}^{-1}$	0.0001-10	2874	2262	2495	2399
$10^{-5} \text{ s}^{-1}$	0.001-100	2793	2230	2475	2410
Average:		2518	2164	2371	2314

(b) The average run-time over five runs.

<i>Updated EGP model</i>		<b>Original linearization</b>		<b>Updated linearization</b>	
<b>Strain-rate</b>	<b>step-size</b>	<b>MNR</b>	<b>FNR</b>	<b>MNR</b>	<b>FNR</b>
$10^{-1} \text{ s}^{-1}$	0.001-0.01	5.41 s	5.05 s	5.07 s	5.07 s
$10^{-2} \text{ s}^{-1}$	0.001-0.1	6.10 s	5.74 s	5.39 s	5.44 s
$10^{-3} \text{ s}^{-1}$	0.001-1	5.81 s	5.51 s	5.16 s	5.21 s
$10^{-4} \text{ s}^{-1}$	0.0001-10	7.13 s	6.04 s	5.83 s	5.81 s
$10^{-5} \text{ s}^{-1}$	0.001-100	7.08 s	6.07 s	5.85 s	5.79 s
Average:		6.31 s	5.68 s	5.46 s	5.46 s

**Table 6.4:** (a) The number of iterations and (b) run-time needed to reach a strain of 0.8 at 60°C for the updated EGP model. The results are shown for a large variable step-size using either the original or updated linearization and using either the Modified Newton-Raphson (MNR) or Full Newton-Raphson (FNR) iteration scheme.

(a) The number of iterations.

<i>Updated EGP model</i>		<b>Original linearization</b>		<b>Updated linearization</b>	
<b>Strain-rate</b>	<b>step-size</b>	<b>MNR</b>	<b>FNR</b>	<b>MNR</b>	<b>FNR</b>
$10^{-1} \text{ s}^{-1}$	0.001-0.05	1154	1174	1217	666
$10^{-2} \text{ s}^{-1}$	0.001-0.5	1230	1182	954	689
$10^{-3} \text{ s}^{-1}$	0.001-5	1195	1179	1086	689
$10^{-4} \text{ s}^{-1}$	0.0001-50	1144	1045	1061	578
$10^{-5} \text{ s}^{-1}$	0.001-500	1060	980	805	593
Average:		1157	1112	1025	620

(b) The average run-time over five runs.

<i>Updated EGP model</i>		<b>Original linearization</b>		<b>Updated linearization</b>	
<b>Strain-rate</b>	<b>step-size</b>	<b>MNR</b>	<b>FNR</b>	<b>MNR</b>	<b>FNR</b>
$10^{-1} \text{ s}^{-1}$	0.001-0.05	1.26 s	1.25 s	1.29 s	0.98 s
$10^{-2} \text{ s}^{-1}$	0.001-0.5	1.18 s	1.44 s	1.06 s	1.04 s
$10^{-3} \text{ s}^{-1}$	0.001-5	1.18 s	1.40 s	1.22 s	0.90 s
$10^{-4} \text{ s}^{-1}$	0.0001-50	1.18 s	1.37 s	1.13 s	0.92 s
$10^{-5} \text{ s}^{-1}$	0.001-500	1.18 s	1.35 s	1.08 s	0.91 s
Average:		1.20 s	1.36 s	1.16 s	0.95 s

## CONCLUSION AND DISCUSSION

---

The research question stated in the introduction of this thesis is as follows:

*How can the Eindhoven Glassy Polymer model be adapted to correspond better to the higher experimentally observed strain-rate dependency and higher experimentally observed yield stress at lower temperatures for uniaxial compression tests of Poly(ether-ether-ketone)?*

The work in this thesis leads to the answer to this question; the Eindhoven Glassy Polymer model will correspond better to the experimentally observed strain-rate dependency and yield behaviour of Poly(ether-ether-ketone) in uniaxial compression tests when the viscosity function is strain-dependent. The obtained results from the EGP model are very accurate if compared to the experimental results. The viscosity function is based on the Ree-Eyring equation where all three Ree-Eyring parameters (activation volume, activation energy and initial viscosities) must be strain-dependent for both the  $\alpha$ - and  $\beta$ -process. The evolution of the Ree-Eyring parameters is expressed by a  $\tanh()$  function for small strains of the  $\alpha$ -process and a quadratic function for large strains of both the  $\alpha$ - and  $\beta$ -process. The evolution of the Ree-Eyring parameters is characterized in a few steps where the basis is fitting the original Ree-Eyring equation to the experimental data over the full strain range. The shear moduli are also made strain-dependent to correctly model stresses in the pre-yield regime. The strain dependency is modelled with an invariant function that is approximately proportional to the strain. This invariant function is prevented from reducing for the evolution based on the  $\tanh()$  function when the loading direction is reversed but does reduce for the evolution based on the quadratic function to correctly model cyclic loading.

**GENERAL RESULTS** A benchmark for comparing results is set up with the original EGP model. This benchmark showed large stress deviations of maximal 14 MPa on a stress of 140 MPa. Furthermore, both the strain-rate dependency and temperature dependency are incorrect at small and large strains. These problems were solved by changing the three Ree-Eyring parameters and the shear moduli to be strain-dependent instead of constant (Equations 4.11 to 4.16 and 4.9) in which the invariant function  $I_r$  in the  $\tanh()$  term is prevented from reducing as defined in Equations 5.1 and 5.2. Together with an update to the viscosity function, this has led to the updated EGP model. The large deviations that occurred in analyses performed with the original EGP model have disappeared. The largest deviations after the yield point are 2.5 MPa on a stress of 90 MPa. This is only a maximum relative deviation of 2.8% instead of the 10.0% for the benchmark. This deviation of the updated EGP model is deemed very small and accurate for stress-strain curves. The problems with the incorrect strain-rate dependency and temperature dependency are solved by making the three Ree-Eyring parameters strain-dependent, which means that the main goal of this thesis has been successfully reached and the results can be

used within future research. Furthermore, the updated EGP model also performs well for strain-rates and temperatures outside the ranges where the model has been characterized on. The strain-rate dependency and the characteristics of the yield point for higher temperatures are as described in literature [Bower, 2003; Barba et al., 2020] while this was not observed in the original EGP model. However, no evidence was found for the decreasing stress at large strains for high temperatures, but this could be because these high temperatures lie within the glass transition zone and cannot accurately be captured with the EGP model.

**PRE-YIELD REGIME AND SHEAR MODULI** It should be noted that the stresses in the pre-yield regime ( $\epsilon < 0.05$ ) show larger deviations than after the yield point. These deviations are in any way still smaller than the deviations found for the benchmark and thus an improvement. The strain-rate dependency in the pre-yield regime (Figure 4.8) is also not as accurately captured as after the yield point. The viscosity is used to implement the strain-rate dependency and is related to the plastic flow. There should be plastic flow to capture the strain-rate dependency. It is a fact that plastic flow starts at the onset of loading for polymers, which is the case for the updated EGP model in contrast to the original EGP model where the plastic flow starts at the yield point. But the low amount of this plastic flow makes it impossible to capture the strain-rate dependency. This could be seen as a limitation of a visco-plastic model such as the EGP model.

There is almost the same deviation visible at all strain-rates and temperatures in the pre-yield regime when only the evolution of the Ree-Eyring parameters is included in the EGP model. This was solved by increasing the shear moduli for the pre-yield regime with a  $\tanh()$  function related to the invariant function. This approach is not very elegant. Because one specific stress-strain curve could be captured by having the shear moduli change over the entire strain range instead of changes in the viscosity, this would then not account for effects like temperature dependency and strain-rate dependency when running other analyses. The shear moduli are determined with a method outlined by [Van Breemen et al., 2011], but this method takes a constant activation volume into account while the activation volume evolves over the strain in the updated EGP model. Simply including the evolving activation volume in the method to determine the shear moduli does not lead to useful results. The method could perhaps in the future be changed entirely to correctly include the evolution of the activation volume, which could lead to better shear moduli that capture the pre-yield regime correctly. The simple evolution of the shear moduli for the pre-yield regime works fine until that time.

**PRESSURE DEPENDENCY** It was concluded in the analysis to determine the pressure dependency (section 4.1) that this parameter is not constant over the strain. This was seen as well for the Ree-Eyring parameters, but the choice was made to not make the pressure dependency strain-dependent. This is because a strain-dependent pressure dependency led to large changes in the stress from the EGP model that did not correspond with the experimental results. It might be possible that the approach from Govaert et al. [2001] that was followed in section 4.1 is not valid for PEEK.

Including the activation volume evolution into the calculation of the pressure dependency did not lead to very different results. However, it is possible that the behaviour of the pressure dependency evolution that is shown in Figure 4.2d is qualitatively correct and should be fitted such that the pre-yield regime is correctly captured by a pressure dependency evolution instead of a shear moduli evolution. However, it is not possible to point out which option is more correct with the available data.

**GENERALISATION OF THE EVOLUTION OF THE REE-EYRING PARAMETERS** The evolution of the Ree-Eyring parameters consists of a part related to the small strain range and a part related to the large strain range.

The part of the evolution related to the small strain range is dependent on a  $\tanh()$  function, which is through the invariant function related to the strain. This function has the useful characteristic to become constant at larger strains, making it a very safe function to use. The function follows the shape of the evolution of the Ree-Eyring parameters very well and can be easily characterized with some intuitive parameters that still give a large range of freedom. All this makes the evolution through the  $\tanh()$  function a great addition to the EGP model.

The part of the evolution related to the large strain range is dependent on a quadratic function, which is through the invariant function related to the strain. This function also follows the evolution of the Ree-Eyring parameters very well and can be easily characterized. The stresses from the EGP model become incorrect when the activation energy or activation volume is near zero or the initial viscosities become very small. A (decreasing) quadratic function will lead to this for large strains. No lower and/or upper limit for these Ree-Eyring parameters is included since this would lead to even more new parameters in the EGP model and it is unknown what the limit should be with the available experimental data. However, it is expected that the part of the evolution related to the large strain range is used with care. It should be checked if the Ree-Eyring parameters are not deviating too much due to very large strains. A possibility is to reduce the influence of the quadratic function if very large strains are expected. This would lead to less accurate results at larger strains, but not to incorrect stress results or divergence of the FEM analysis.

The constants within the evolution of the Ree-Eyring parameters have been chosen such that the updated EGP model can reduce to the original EGP model with the constant Ree-Eyring parameters. This is done such that the EGP model stays very general to model other polymers where the constant Ree-Eyring parameters are a better (and perhaps easier) assumption.

An important question is how general the evolution of the Ree-Eyring parameters is. The available data led to the combination of the  $\tanh()$  and quadratic evolution. The current evolution of the Ree-Eyring parameters can handle a lot of different cases since the evolution at small strains and large strains are separated. But it cannot be said with 100% certainty that this evolution of the Ree-Eyring parameters is the best fit for different types of PEEK or other polymers. [Wendlandt et al. \[2005\]](#) shows evolving activation volume for several polymers. It seems that the shape of the activation volume evolution of the polymers PMMA, PPO, PC and PS can be approximated well with the combination of the  $\tanh()$  and quadratic functions, except for the evolution at very large strains in which the activation volume evolution shows a decrease in slope.

**PHYSICAL BEHAVIOUR** The EGP model is created at a macro-mechanical level as opposed to a micromechanical level including the microstructural composition [[Senden, 2009](#)]. This thesis also solves a problem from a macro-mechanical view without checking material related physics at a micro-level. The possible material related changes that lead to the evolution of the Ree-Eyring parameters are discussed based on the available literature.

The crystallinity of a polymer is dependent on the temperature. The temperature dependency (activation energy) can then be linked to the rate of crystallinity. This rate of crystallinity is, from a material physics point of view, the mechanism that changes the mechanical behaviour [[Doumeng et al., 2019](#)]. The crystallinity of PEEK decreases at larger strains of  $\approx 0.6$  for the strain rates used in this thesis ( $< 10^3 \text{ s}^{-1}$ ) [[Rae et al., 2007](#)]. The yielding of polymers can be seen as stress-induced rubbery behaviour [[Van Melick et al., 2003](#)], which could lead to strain-induced crystallization at larger strains [[Chien and Weiss, 1988](#)]. Any of these changes in

crystallinity could also lead to a different rate of crystallinity and thus a different temperature dependency for larger strains.

The activation volume can be linked to the activation energy in that it determines the decrease of activation energy for segmental motion in the direction of the applied stress [Wendlandt et al., 2005]. As such, activation volume could also be linked to the crystallinity or rate of crystallinity of a polymer.

Plastic flow leads to the separation of crystalline segments at lower strains, which could be the reason for the quickly changing activation volume, activation energy and initial viscosities at lower strains. As described before, the plastic flow does already start at the onset of loading, just like the Ree-Eyring parameters evolution.

**BENCHMARK ACCURACY** The benchmark introduced in chapter 3 is one of many possible characterizations of the original EGP model due to the large number of parameters within the model. It should be empathised that no characterization leads to the same results as for the experiments. This is because the strain-rate dependency and temperature dependency change over the strain, which is not included in the original EGP model. Each characterization would lead to the same confirmation of the problem statement in section 3.4. There are characterizations possible that would lead to, for example, better results in the low strain range. But these characterizations would also lead to worse results for moderate and large strains. The characterization of the benchmark is chosen as it is for two reasons. Firstly, it shows all the issues with the original EGP model to make a good comparison with results obtained from the updated EGP model. Secondly, it is as close to the experimental results as possible over the entire strain range.

The benchmark uses 23  $\alpha$ -modes and 4  $\beta$ -modes, which is a high number of modes. A higher number of modes is more accurate but is also more computationally expensive. This thesis focuses on accuracy, which is the reason for the high number of modes. It is also possible to obtain good results with a smaller number of modes. It is advisable to lower the number of modes when using this characterization in large models.

Another comment on the benchmark is that the experimental results for strains above 0.5 are considered less accurate due to the failing lubrication of the sample and inhomogeneous deformation that play a role in the stress-strain behaviour. It is assumed that this effect will lead to the same stress deviation for all strain-rates and temperatures, meaning that the effect could be countered by changing the elastic hardening contribution. This will then not change anything for the results of this thesis. It is unknown how extensive the effect is, so no correction is made.

**CYCLIC LOADING** Cyclic loading is relevant to the 'SafeRIDE' project (See chapter 1) since it will investigate the long term behaviour of fibre reinforced PEEK in terms of fatigue. Thus, cyclic loading cases are investigated. This thesis only takes a first step in the right direction by making sure that the qualitative behaviour of the cyclic loading with the strain-dependent viscosity is good. Due to the lack of data, no conclusions on the cyclic loading behaviour are made. Thus, it is of great importance to, in the future, gather good data on cyclic loading cases for PEEK.

Another important aspect of polymers for cyclic loading cases is viscous strain hardening. This has been a subject of research before and has been added to constitutive models by making one or two Ree-Eyring parameters strain-dependent [Senden et al., 2012a; Wendlandt et al., 2005]. This thesis has the goal of correctly modelling stress-strain behaviour instead of including viscous strain hardening. It has been shown that by including the evolution of all three Ree-Eyring parameters, the viscous strain hardening is still included in the model. It can very well be that including the exact evolution of the Ree-Eyring parameters is the most accurate way of modelling the stress behaviour for all loading cases. It might even be said that keeping true to the original work of Ree and Eyring [1955] is the key to correctly model PEEK.

## 7.1 RECOMMENDATIONS

Seven recommendations are drawn up based on the work within this thesis and the discussion in this chapter:

- *Larger strains:* Experimental uniaxial compression tests at strains larger than 0.7 can give an insight into the evolution of the Ree-Eyring parameters at these larger strains or/and possible lower bounds of the Ree-Eyring parameters. Effects like inhomogeneous deformation and insufficient lubrication of the sample have to be accounted for if tests at these very large strains are performed. For example, [Rae et al. \[2007\]](#) performs incremental compression loading with re-lubrication between the steps, but these test results could be influenced by cold crystallisation;
- *Cyclic loading:* Stress-strain curves for a cyclic loading test of PEEK have to be experimentally obtained to correctly model the response of the EGP model for cyclic loading cases. It is relatively easy to test compression/compression cyclic loading cases and investigate the results. Tension/tension cyclic loading cases are also possible, but extra care is needed due to non-linear effects such as necking.

Another possibility is to use fully-reversed compression/tension cyclic loading cases. The experimental procedure outlined in [Senden et al. \[2010\]](#) can be used to obtain experimental stress-strain results. This paper uses dog-bone shaped samples, which are loaded in tension until a prescribed strain. Whereafter, the samples are unloaded to zero force. lastly, cylindrical specimens machined from the pretensioned samples are loaded in compression to obtain the compression behaviour. [Li et al. \[2019\]](#) shows that a reduction in stiffness is expected in the case of fully-reversed cyclic loading, which is currently not included in the EGP model. The correct evolution of the Ree-Eyring parameters after the reversal of loading can be investigated as well.

- *Updating the characterization of the modal parameters:* The evolution of the activation volume can be included in the characterization of the initial viscosities and shear moduli as outlined by [Van Breemen et al. \[2011\]](#) and lead to more accurate results. It is possible that the shear moduli evolution in the pre-yield regime is not necessary anymore if this characterization step is updated;
- *Pressure dependency:* Section 4.1 shows that the pressure dependency changes over the strain. It is possible that the behaviour of the pressure dependency evolution is qualitatively correct and should be fitted such that the pre-yield regime is correctly captured by a pressure dependency evolution instead of a shear moduli evolution. Stress-strain results for different loading cases (which implicitly means that there is a different pressure dependency) are needed to make correct conclusions about the pressure dependency (evolution);
- *Rate of crystallisation:* An evolving rate of crystallisation could be the micro-mechanical explanation of the evolution of the Ree-Eyring parameters but cannot be concluded based on the currently available literature. The crystallisation of PEEK can be investigated at multiple temperatures and strain rates over a large strain range. [Kong and Hay \[2002\]](#) shows how differential scanning calorimetry (DSC) can be used to determine the crystallinity of a polymer.
- *Generalisation:* Experimental tests on other grades of PEEK and/or other polymers could point out which generalisation of the evolution of the Ree-Eyring parameters is the best for a general model such as the EGP model.
- *Linearization:* Section 6.3 hints that the updated linearization is not fully correctly derived and/or implemented. The updated linearization can be checked.



## BIBLIOGRAPHY

---

- Barba, D., Arias, A., and Garcia-Gonzalez, D. (2020). Temperature and strain rate dependences on hardening and softening behaviours in semi-crystalline polymers: Application to peek. *International Journal of Solids and Structures*, 182:205–217.
- Bauschinger, J. (1881). Changes of the elastic limit and the modulus of elasticity on various metals. *Zivilingenieur*, 27:289–348.
- Bower, D. I. (2003). An introduction to polymer physics.
- Boyce, M. C., Weber, G., and Parks, D. M. (1989). On the kinematics of finite strain plasticity. *Journal of the Mechanics and Physics of Solids*, 37(5):647–665.
- Chien, M. C. and Weiss, R. (1988). Strain-induced crystallization behavior of poly(ether ether ketone)(peek). *Polymer Engineering & Science*, 28(1):6–12.
- Clarijs, C. (2017). The epg model for dummies.
- Doumeng, M., Ferry, F., Delbé, K., Mérian, T., Chabert, F., Berthet, F., Marsan, O., Nassiet, V., and Denape, J. (2019). Evolution of crystallinity of peek and glass-fibre reinforced peek under tribological conditions using raman spectroscopy. *Wear*, 426:1040–1046.
- Dynaflow Research Group (2020). Jive • dynaflow research group. [Online; accessed 9-December-2021].
- Edwards, S. and Vilgis, T. (1986). The effect of entanglements in rubber elasticity. *Polymer*, 27(4):483–492.
- El-Qoubaa, Z. and Othman, R. (2015). Characterization and modeling of the strain rate sensitivity of polyetheretherketone's compressive yield stress. *Materials & Design (1980-2015)*, 66:336–345.
- Govaert, L., Schellens, H., Thomassen, H., Smit, R., Terzoli, L., and Peijs, T. (2001). A micromechanical approach to time-dependent failure in off-axis loaded polymer composites. *Composites Part A: Applied Science and Manufacturing*, 32(12):1697–1711.
- Govaert, L., Timmermans, P., and Brekelmans, W. (2000). The influence of intrinsic strain softening on strain localization in polycarbonate: modeling and experimental validation. *J. Eng. Mater. Technol.*, 122(2):177–185.
- Haward, R. and Thackray, G. . (1968). The use of a mathematical model to describe isothermal stress-strain curves in glassy thermoplastics. *Proceedings of the Royal Society of London. Series A. Mathematical and Physical Sciences*, 302(1471):453–472.
- Hoy, R. S. and Robbins, M. O. (2008). Strain hardening of polymer glasses: Entanglements, energetics, and plasticity. *Physical Review E*, 77(3):031801.
- Klompen, E., Engels, T., Govaert, L., and Meijer, H. (2005). Modeling of the postyield response of glassy polymers: influence of thermomechanical history. *Macromolecules*, 38(16):6997–7008.
- Klompen, E. and Govaert, L. E. (1999). Nonlinear viscoelastic behaviour of thermorheologically complex materials. *Mechanics of Time-Dependent Materials*, 3(1):49–69.

- Kong, Y. and Hay, J. (2002). The measurement of the crystallinity of polymers by dsc. *Polymer*, 43(14):3873–3878.
- Kramer, E. J. (2005). Open questions in the physics of deformation of polymer glasses.
- Li, W., Gazonas, G., Brown, E. N., Rae, P. J., and Negahban, M. (2019). Thermomechanical model for monotonic and cyclic loading of peek. *Mechanics of Materials*, 129:113–138.
- Nayak, K., Read, D. J., McLeish, T. C., Hine, P. J., and Tassieri, M. (2011). A coarse-grained molecular model of strain-hardening for polymers in the marginally glassy state. *Journal of Polymer Science Part B: Polymer Physics*, 49(13):920–938.
- Rae, P., Brown, E., and Orler, E. (2007). The mechanical properties of poly (ether-ether-ketone)(peek) with emphasis on the large compressive strain response. *Polymer*, 48(2):598–615.
- Ree, T. and Eyring, H. (1955). Theory of non-newtonian flow. i. solid plastic system. *Journal of Applied Physics*, 26(7):793–800.
- Roylance, D. (2001). Engineering viscoelasticity. *Department of Materials Science and Engineering—Massachusetts Institute of Technology, Cambridge MA*, 2139:1–37.
- Safari, K. H., Zamani, J., Ferreira, F. J., and Guedes, R. M. (2013). Constitutive modeling of polycarbonate during high strain rate deformation. *Polymer Engineering & Science*, 53(4):752–761.
- Scipy org (2021). Scipy python package v1.6.3. <https://www.scipy.org/>. released on 25-04-2021.
- Senden, D. (2009). *Towards a macroscopic model for the finite-strain mechanical response of semi-crystalline polymers*. PhD thesis, Master Thesis, University of Technology Eindhoven.
- Senden, D., Van Dommelen, J., and Govaert, L. (2010). Strain hardening and its relation to bauschinger effects in oriented polymers. *Journal of Polymer Science Part B: Polymer Physics*, 48(13):1483–1494.
- Senden, D. J., Krop, S., van Dommelen, J., and Govaert, L. (2012a). Rate-and temperature-dependent strain hardening of polycarbonate. *Journal of Polymer Science Part B: Polymer Physics*, 50(24):1680–1693.
- Senden, D. J., Van Dommelen, J. A., and Govaert, L. E. (2012b). Physical aging and deformation kinetics of polycarbonate. *Journal of Polymer Science Part B: Polymer Physics*, 50(22):1589–1596.
- Sundararajan and Govaert (2021). personal communication.
- Tervoort, T., Brekelmans, W., and Govaert, L. (1994). A 3-d stress-strain relation for glassy polymers. In *9th International Conference on Deformation, Yield and Fracture of Polymers (DYFP 1994)*, pages P66–1. The Institute of Materials.
- Tervoort, T., Klompen, E., and Govaert, L. (1996). A multi-mode approach to finite, three-dimensional, nonlinear viscoelastic behavior of polymer glasses. *Journal of Rheology*, 40(5):779–797.
- Tervoort, T., Smit, R., Brekelmans, W., and Govaert, L. (1997). A constitutive equation for the elasto-viscoplastic deformation of glassy polymers. *Mechanics of Time-Dependent Materials*, 1(3):269–291.
- TUE (2010). Vector and tensor algebra (including column and matrix notation).

- Van Breemen, L., Klompen, E., Govaert, L., and Meijer, H. (2011). Extending the epp constitutive model for polymer glasses to multiple relaxation times. *Journal of the Mechanics and Physics of Solids*, 59(10):2191–2207.
- Van Melick, H., Govaert, L., and Meijer, H. (2003). On the origin of strain hardening in glassy polymers. *Polymer*, 44(8):2493–2502.
- Wendlandt, M., Tervoort, T. A., and Suter, U. W. (2005). Non-linear, rate-dependent strain-hardening behavior of polymer glasses. *Polymer*, 46(25):11786–11797.
- Yasuda, K. (1979). *Investigation of the analogies between viscometric and linear viscoelastic properties of polystyrene fluids*. PhD thesis, Massachusetts Institute of Technology.



## ORIGINAL EGP MODEL PARAMETERS

Table A.1: All parameters of the original EGP model. For each parameter; it's name, equations it was used in, and influence on the model is given.

$T$	<p><b>Name:</b> Temperature</p> <p><b>Equation(s):</b> 2.12 and underlying functions</p> <p><b>Influence:</b> The temperature has a very big influence on the model.</p>
$R$	<p><b>Name:</b> Universal gas constant</p> <p><b>Equation(s):</b> 2.12 and 2.17</p> <p><b>Influence:</b> constant value of <math>8.3144598 \cdot 10^3</math>.</p>
$k_b$	<p><b>Name:</b> Boltzmann's constant</p> <p><b>Equation(s):</b> 2.13</p> <p><b>Influence:</b> constant value of <math>1.38064852 \cdot 10^{-20}</math>.</p>
$\Delta H_{0\alpha}$	<p><b>Name:</b> activation enthalpy/energy; alpha process</p> <p><b>Equation(s):</b> 2.29</p> <p><b>Influence:</b> Influence on the temperature dependency of the alpha process. A higher value will lead to lower stresses at higher temperatures.</p>
$\Delta H_{0\beta}$	<p><b>Name:</b> activation enthalpy/energy; beta process</p> <p><b>Equation(s):</b> 2.30</p> <p><b>Influence:</b> Influence on the temperature dependency of the beta process. A higher value will lead to lower stresses at higher temperatures.</p>
$C_{1,\alpha}$	<p><b>Name:</b> Viscous hardening stress constant for activation energy evolution; alpha process</p> <p><b>Equation(s):</b> 2.29</p> <p><b>Influence:</b> Leads in a quadratic relationship to strain to lower/higher activation energy at higher strains for the alpha process. this leads to different stresses at higher strains for other temperatures than the one characterized on. Parameter is mainly needed for loading/unloading situations.</p>
$C_{2,\alpha}$	<p><b>Name:</b> Viscous hardening stress constant for initial viscosity evolution; alpha process</p> <p><b>Equation(s):</b> 2.27</p> <p><b>Influence:</b> Leads in a quadratic relationship to strain to lower/higher initial viscosities at higher strains for the alpha process. this leads to different stresses at higher strains. Parameter is mainly needed for loading/unloading situations.</p>

(Continued on the next page)

$C_{1,\beta}$	<p><b>Name:</b> Viscous hardening stress constant for activation energy evolution; beta process</p> <p><b>Equation(s):</b> 2.30</p> <p><b>Influence:</b> Leads in a linear relationship to strain to lower/higher activation energy at higher strains for the beta process. this leads to different stresses at higher strains for other temperatures than the one characterized on. Parameter is mainly needed for loading/unloading situations.</p>
$C_{2,\beta}$	<p><b>Name:</b> Viscous hardening stress constant for initial viscosity evolution; beta process</p> <p><b>Equation(s):</b> 2.28</p> <p><b>Influence:</b> Leads in a linear relationship to strain to lower/higher initial viscosities at higher strains for the beta process. this leads to different stresses at higher strains. Parameter is mainly needed for loading/unloading situations.</p>
$G_r$	<p><b>Name:</b> Elastic strain hardening modulus</p> <p><b>Equation(s):</b> 2.21</p> <p><b>Influence:</b> Determines the linear slope of elastic strain hardening behaviour.</p>
$\alpha_r$	<p><b>Name:</b> Limited extensibility of the molecular network</p> <p><b>Equation(s):</b> 2.22</p> <p><b>Influence:</b> Determines the non-linear response of the elastic strain hardening. A higher value leads to larger slopes of the strain hardening stress at higher strains.</p>
$\zeta_r$	<p><b>Name:</b> Mobility of entanglements of the molecular network</p> <p><b>Equation(s):</b> 2.22</p> <p><b>Influence:</b> Determines the non-linear response of the elastic strain hardening. Should be kept at 0 for polymers.</p>
$V_\alpha$	<p><b>Name:</b> Shear equivalent activation volume; alpha process</p> <p><b>Equation(s):</b> 2.13</p> <p><b>Influence:</b> Determines the strain-rate dependency of the alpha process. A higher value leads to a lower strain rate dependency. the activation volume is also needed to determine the initial viscosities.</p>
$V_\beta$	<p><b>Name:</b> Shear equivalent activation volume; beta process</p> <p><b>Equation(s):</b> 2.13</p> <p><b>Influence:</b> Determines the strain-rate dependency of the beta process. A higher value leads to a lower strain rate dependency. the activation volume is also needed to determine the initial viscosities.</p>
$\mu_\alpha$	<p><b>Name:</b> Pressure dependency; alpha process</p> <p><b>Equation(s):</b> 2.12</p> <p><b>Influence:</b> Changes the height of the yield stress for the alpha process based on the pressure on the model. Works together with temperature and the activation volume.</p>
$\mu_\beta$	<p><b>Name:</b> Pressure dependency; beta process</p> <p><b>Equation(s):</b> 2.12</p> <p><b>Influence:</b> Changes the height of the yield stress for the beta process based on the pressure on the model. Works together with temperature and the activation volume.</p>

(Continued on the next page)

$S_{S_\alpha}$	<p><b>Name:</b> Ageing-induced changes in entropy; alpha process</p> <p><b>Equation(s):</b> <a href="#">2.17</a></p> <p><b>Influence:</b> A higher value leads to a higher yield stress and a stronger softening behaviour in the alpha process. The parameter is based on the age of the polymer</p>
$S_{S_\beta}$	<p><b>Name:</b> Ageing-induced changes in entropy; beta process</p> <p><b>Equation(s):</b> <a href="#">2.17</a></p> <p><b>Influence:</b> A higher value leads to a higher yield stress and a stronger softening behaviour in the beta process. The parameter is based on the age of the polymer</p>
$S_{H_\alpha}$	<p><b>Name:</b> Ageing of the activation enthalpy; alpha process</p> <p><b>Equation(s):</b> <a href="#">2.17</a> and <a href="#">2.29</a></p> <p><b>Influence:</b> A higher value leads to a stronger yield stress and a stronger softening behaviour in the alpha process, but is influenced by the temperature. The parameter also influences the activation energy based on the softening function.</p>
$S_{H_\beta}$	<p><b>Name:</b> Ageing of the activation enthalpy; beta process</p> <p><b>Equation(s):</b> <a href="#">2.17</a> and <a href="#">2.30</a></p> <p><b>Influence:</b> A higher value leads to a stronger yield stress and a stronger softening behaviour in the beta process, but is influenced by the temperature. The parameter also influences the activation energy based on the softening function.</p>
$r_{0_\alpha}$ , $r_{1_\alpha}$ , $r_{2_\alpha}$	<p><b>Name:</b> fitting parameters of the modified Carreau-Yassuda function; alpha process</p> <p><b>Equation(s):</b> <a href="#">2.20</a></p> <p><b>Influence:</b> The parameters determine the shape of the softening behaviour for the alpha process. Mainly, the slopes and length of the slopes can be determined.</p>
$r_{0_\beta}$ , $r_{1_\beta}$ , $r_{2_\beta}$	<p><b>Name:</b> fitting parameters of the modified Carreau-Yassuda function; beta process</p> <p><b>Equation(s):</b> <a href="#">2.20</a></p> <p><b>Influence:</b> The parameters determine the shape of the softening behaviour for the beta process. Mainly, the slopes and length of the slopes can be determined.</p>
$\kappa$	<p><b>Name:</b> Bulk modulus</p> <p><b>Equation(s):</b> <a href="#">2.8</a></p> <p><b>Influence:</b> constant value of 5475 for PEEK.</p>
$G_i$	<p><b>Name:</b> Shear moduli</p> <p><b>Equation(s):</b> <a href="#">2.9</a></p> <p><b>Influence:</b> Determines the shape of the yield behaviour. One shear modulus is needed for each mode included in the model.</p>
$\eta_{0_i}$	<p><b>Name:</b> Initial viscosities</p> <p><b>Equation(s):</b> <a href="#">2.27</a> and <a href="#">2.28</a></p> <p><b>Influence:</b> Determines the shape of the yield behaviour. One initial viscosity is needed per mode.</p>



## CHARACTERIZATION OF THE BENCHMARK

---

The Tables B.1, B.2 and B.3 show the values determined for each parameter of the original EGP model.

**Table B.1:** The general parameters of the original EGP model.

Parameter	Value	Unit
$T$	Variable	$^{\circ}\text{C}$
$R$	8.31	$\text{J} \cdot \text{mol}^{-1} \cdot \text{K}^{-1}$
$k_b$	$1.38 \cdot 10^{-20}$	$\text{N} \cdot \text{mm} \cdot \text{K}^{-1}$
$\Delta H_{0\alpha}$	$685 \cdot 10^3$	$\text{J} \cdot \text{mol}^{-1}$
$\Delta H_{0\beta}$	$90 \cdot 10^3$	$\text{J} \cdot \text{mol}^{-1}$
$C_{1,\alpha}$	0	-
$C_{2,\alpha}$	0	-
$C_{1,\beta}$	0	-
$C_{2,\beta}$	0	-
$G_r$	5.0	$\text{MPa}$
$\alpha_r$	0.22	-
$\xi_r$	0	-
$V_{\alpha}$	$9.2 \cdot 10^{-18}$	$\text{mm}^3$
$V_{\beta}$	$5.0 \cdot 10^{-18}$	$\text{mm}^3$
$\mu_{\alpha}$	0.06	-
$\mu_{\beta}$	0.06	-
$S_{S_{\alpha}}$	2.0	-
$S_{S_{\beta}}$	0	-
$S_{H_{\alpha}}$	0	-
$S_{H_{\beta}}$	0	-
$r_{0\alpha}$	0.965	-
$r_{1\alpha}$	-5.0	-
$r_{2\alpha}$	-5.0	-
$r_{0\beta}$	0.965	-
$r_{1\beta}$	-5.0	-
$r_{2\beta}$	-5.0	-
$\kappa$	5475	$\text{N}/\text{mm}^2$

**Table B.2:** The modal parameters for the  $\alpha$ -process of the original EGP model.

<b>Mode</b>	<b>shear modulus</b> $G_j$ [MPa]	<b>initial viscosity</b> $\eta_j$ [MPa·s]
1	97.663	$1.646 \cdot 10^{-57}$
2	96.330	$2.319 \cdot 10^{-58}$
3	43.014	$1.479 \cdot 10^{-59}$
4	50.714	$2.491 \cdot 10^{-60}$
5	51.848	$3.638 \cdot 10^{-61}$
6	64.795	$6.494 \cdot 10^{-62}$
7	84.610	$1.211 \cdot 10^{-62}$
8	109.077	$2.231 \cdot 10^{-63}$
9	99.498	$2.907 \cdot 10^{-64}$
10	75.487	$3.150 \cdot 10^{-65}$
11	34.353	$2.048 \cdot 10^{-66}$
12	36.707	$3.126 \cdot 10^{-67}$
13	24.847	$3.022 \cdot 10^{-68}$
14	24.904	$4.327 \cdot 10^{-69}$
15	17.940	$4.453 \cdot 10^{-70}$
16	21.714	$7.699 \cdot 10^{-71}$
17	15.974	$8.090 \cdot 10^{-72}$
18	14.928	$1.080 \cdot 10^{-72}$
19	15.567	$1.609 \cdot 10^{-73}$
20	8.351	$1.233 \cdot 10^{-74}$
21	6.457	$1.362 \cdot 10^{-75}$
22	1.166	$3.513 \cdot 10^{-77}$
23	35.205	$1.128 \cdot 10^{-97}$

**Table B.3:** The modal parameters for the  $\beta$ -process of the original EGP model.

<b>Mode</b>	<b>shear modulus</b> $G_k$ [MPa]	<b>initial viscosity</b> $\eta_k$ [MPa·s]
1	19.909	$1.939 \cdot 10^{-13}$
2	114.628	$4.310 \cdot 10^{-13}$
3	43.595	$2.443 \cdot 10^{-14}$
4	28.914	$6.256 \cdot 10^{-15}$

## STRESS-STRAIN CURVES FROM THE BENCHMARK

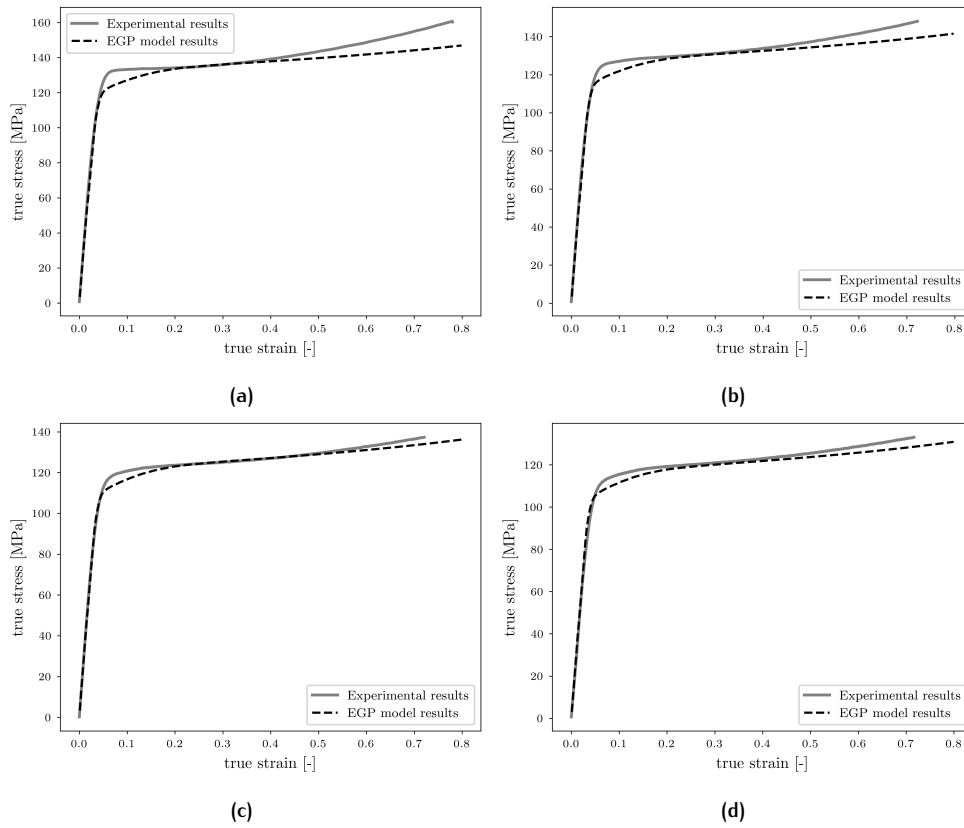


Figure C.1: The original EGP model results and experimental results at 20°C and a strain rate of (a)  $10^{-2}$ , (b)  $10^{-3}$ , (c)  $10^{-4}$  and (d)  $10^{-5}$ .

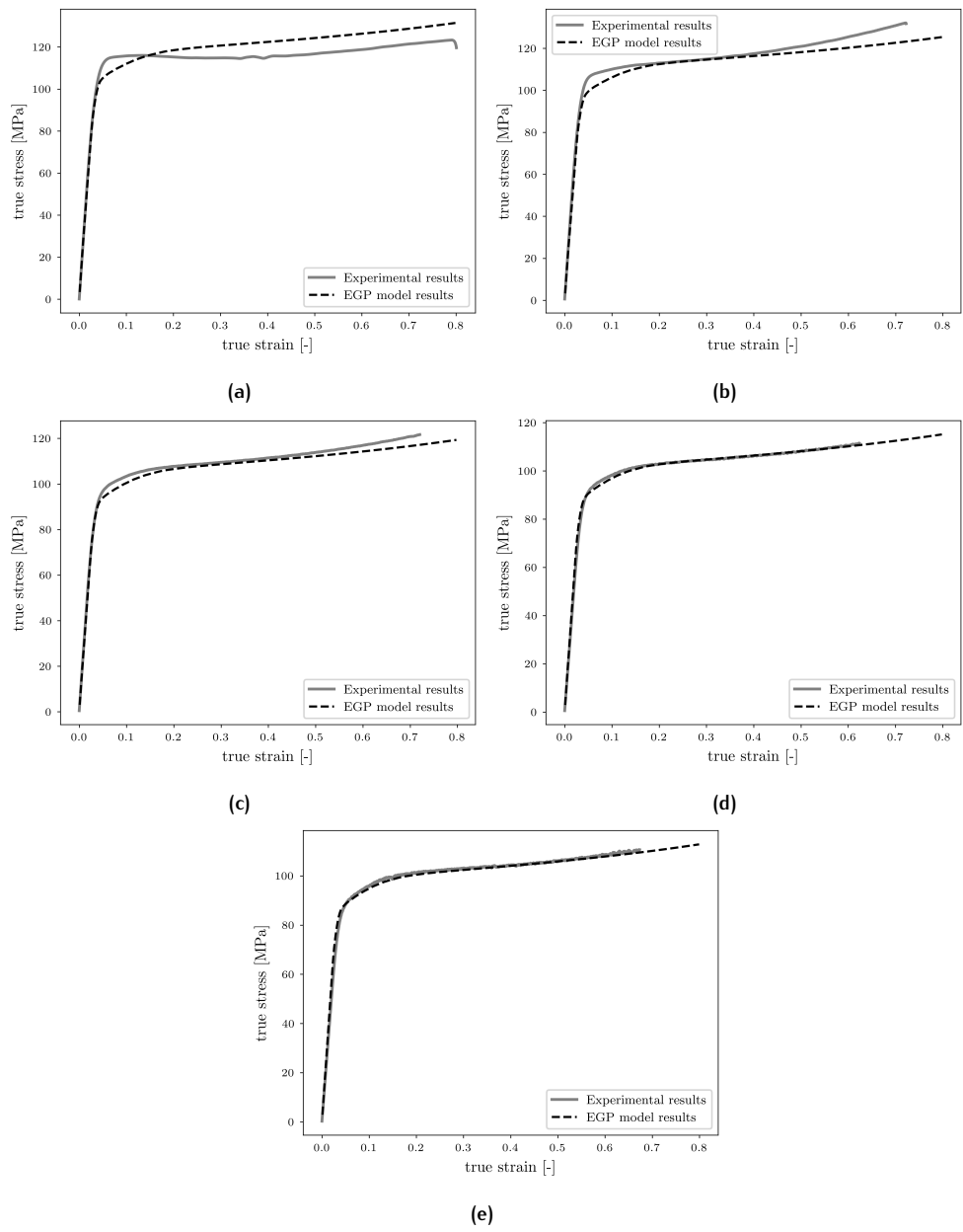


Figure C.2: The original EGP model results and experimental results at  $60^{\circ}\text{C}$  and a strain rate of (a)  $10^{-1}$ , (b)  $10^{-2}$ , (c)  $10^{-3}$ , (d)  $10^{-4}$  and (e)  $10^{-5}$ .

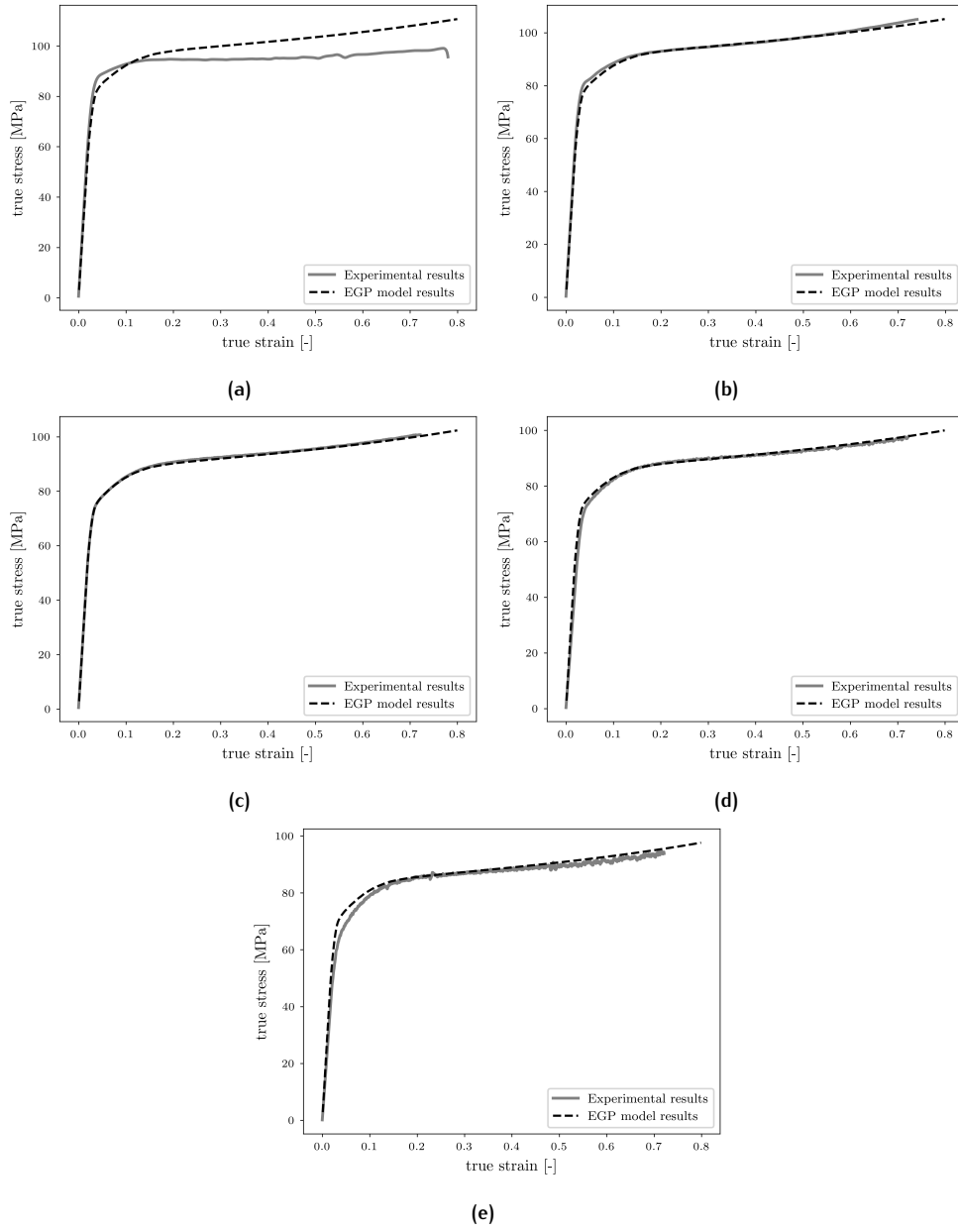


Figure C.3: The original EGP model results and experimental results at  $100^{\circ}\text{C}$  and a strain rate of (a)  $10^{-1}$ , (b)  $10^{-2}$ , (c)  $10^{-3}$ , (d)  $10^{-4}$  and (e)  $10^{-5}$ .



# APPENDIX D

## STRESS-STRAIN CURVES FROM THE UPDATED EGP MODEL

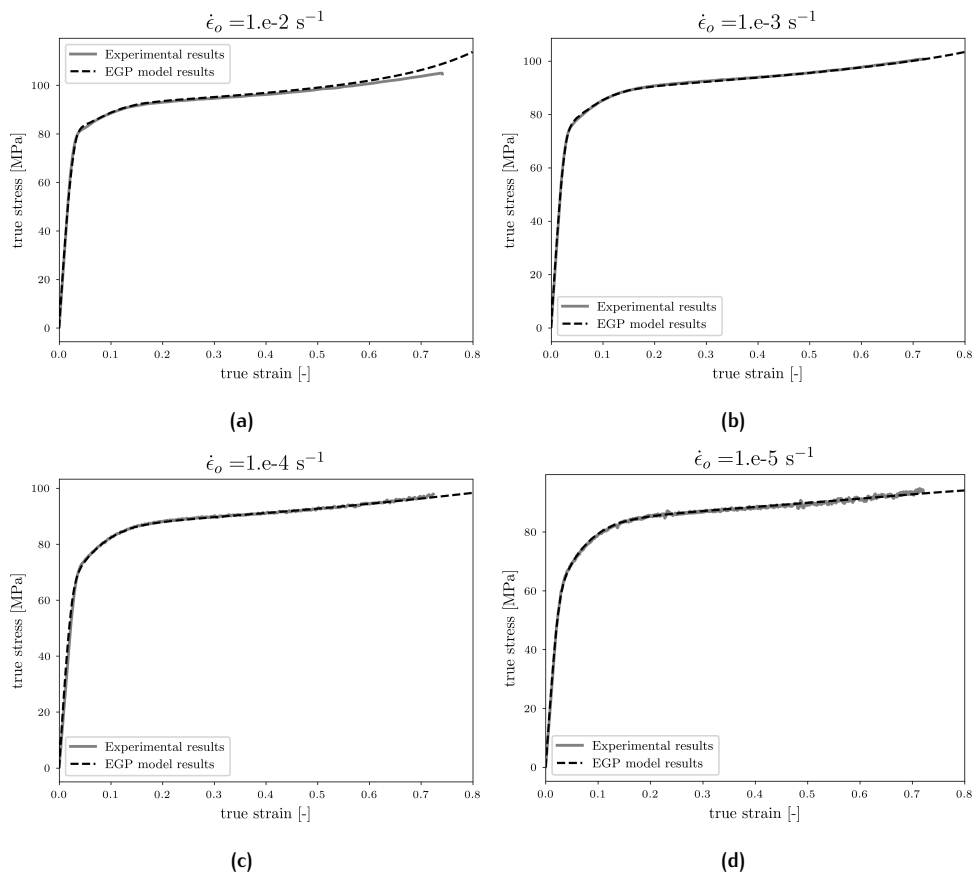


Figure D.1: The updated EGP model results and experimental results at 20°C and a strain rate of (a)  $10^{-2}$ , (b)  $10^{-3}$ , (c)  $10^{-4}$  and (d)  $10^{-5}$ .

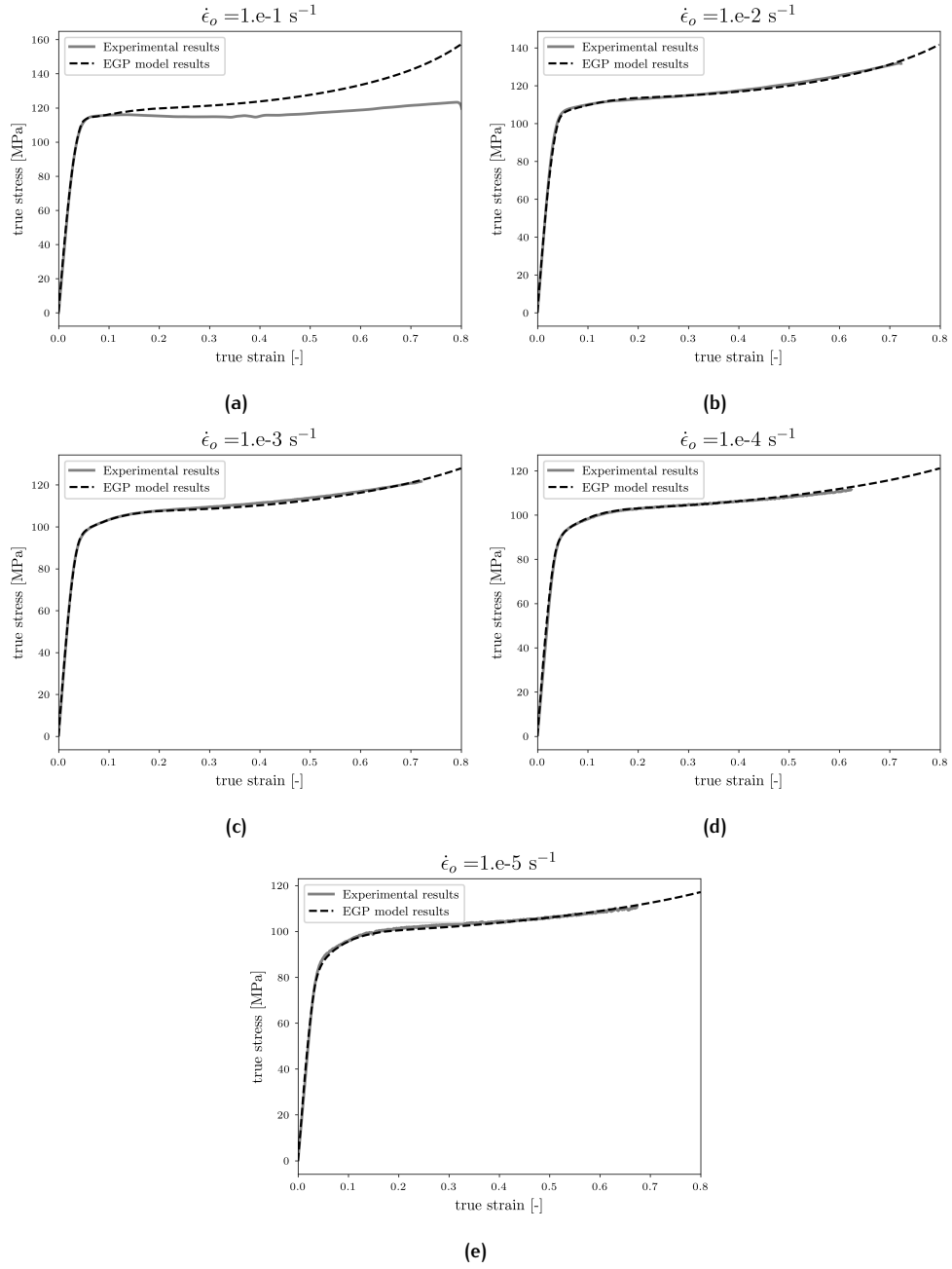


Figure D.2: The updated EGP model results and experimental results at  $60^\circ\text{C}$  and a strain rate of (a)  $10^{-1}$ , (b)  $10^{-2}$ , (c)  $10^{-3}$ , (d)  $10^{-4}$  and (e)  $10^{-5}$ .

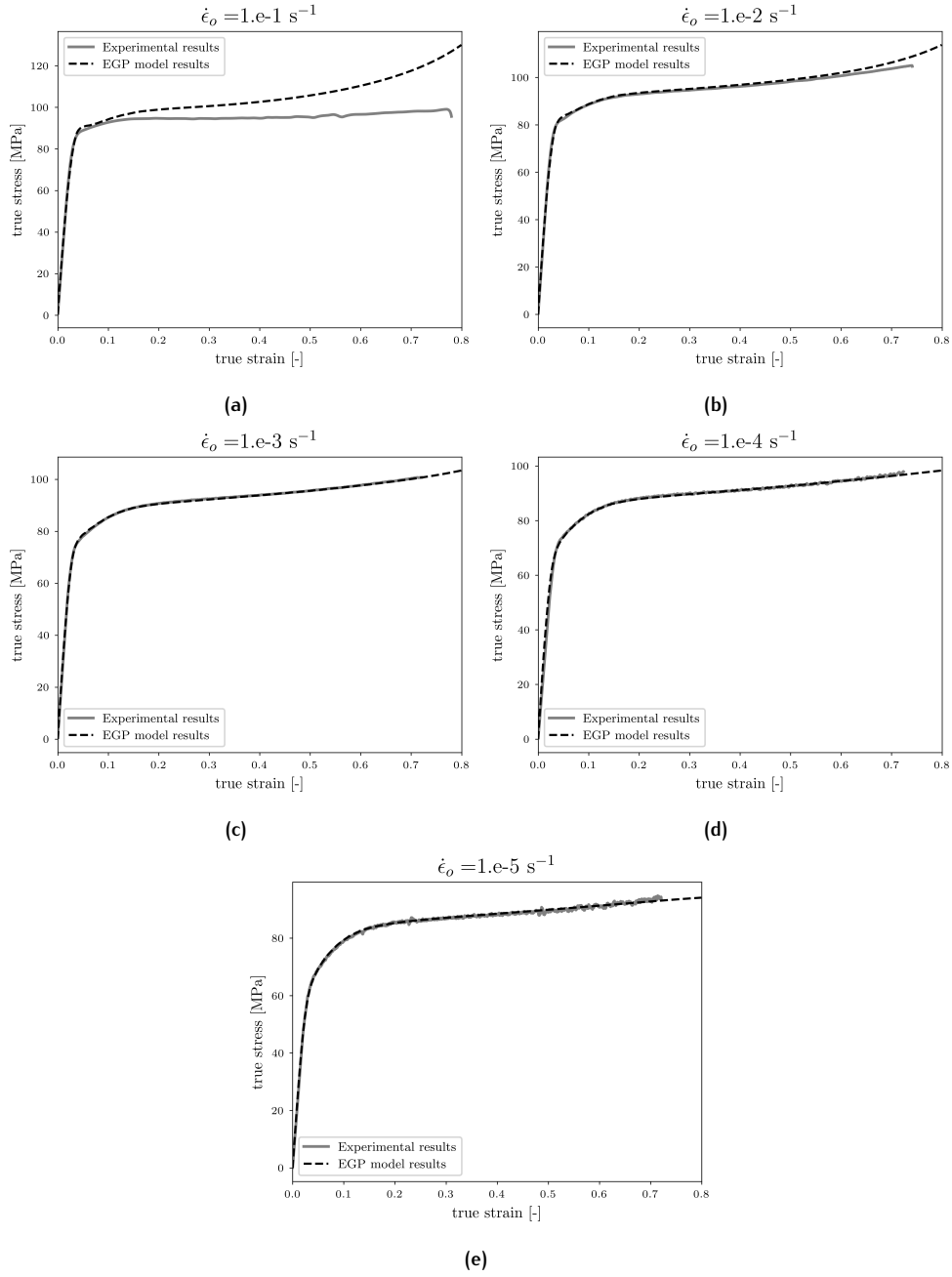


Figure D.3: The updated EGP model results and experimental results at 100°C and a strain rate of (a)  $10^{-1}$ , (b)  $10^{-2}$ , (c)  $10^{-3}$ , (d)  $10^{-4}$  and (e)  $10^{-5}$ .



## UPDATED C++ CODE FOR THE STRESS CALCULATION

Code E.1: The new C++ code for the invariant function

```

1 // Update htB and htBnon
2
3 double I_1, I_2, trmtB2, htB;
4
5 trace ( mtB, I_1 );
6
7 trace ( matmul ( mtB, mtB ), trmtB2 );
8
9 I_2 = 0.5 * ( pow(I_1, 2) - trmtB2 );
10
11 htB = pow( pow(I_1, 2) / 3 - I_2, 0.5 );
12
13 if ( htB < htBnonB ) {htBnon = htBnonB;}
14 else {htBnon = htB;}

```

Code E.2: The new C++ code for the shear moduli and activation volume evolution

```

1 double toa, tob;
2
3 if ( strHardening_ == "NEOHOOKEAN" )
4 {
5   toa = toa_;
6   tob = tob_;
7 }
8 else
9 {
10 // Strain dependent activation volume
11
12 double Vacta, Vactb;
13
14 Vacta = (Vconsta_ - CV1a_) + CV1a_ * tanh (CV2a_ * (htBnon - CV3a_) +
15   CV4a_ * pow(htB, 2));
16
17 Vactb = Vconstb_ + CV4b_ * pow(htB, 2);
18
19 toa = kb_ * T_ / Vacta;
20 tob = kb_ * T_ / Vactb;
21
22 // Strain dependent shear moduli
23
24 for (idx_t i = 0; i < nam_; i++)
25   {G[i] = Gconst_[i] * ((1 + CG1a_) - CG1a_ *
26     tanh (CG2a_ * (htBnon - CG3a_)));}
27
28 for (idx_t i = nam_; i < nom_; i++)
29   {G[i] = Gconst_[i];}
30 }

```

Code E.3: The updated C++ code for the viscosity function

```

1 //-----
2 //   update viscosity
3 //-----
4
5 void          EGPMaterial::updateViscosity_
6
7   (const Vector& h, const Vector& Rg, const double htB,
8
9    const double htBnon, const Vector& S, const double& p,
10
11   const double& toa, const double& tob, const Vector& teq,
12
13   const M33& mtB, Vector& ho, double& dHoa, double& dHob)
14
15 {
16   // For the Simplified EGP model viscosity
17
18   if ( strHardening_ == "NEOHOOKEAN" )
19   {
20     if (teq[0] > 1.0e-15)
21     {
22       for (idx_t i = 0; i < nam_; i++)
23       {
24         h[i] = ho[i] * exp(S[0] + (ma_ * p) / toa) *
25
26           (teq[0] / toa) / sinh(teq[0] / toa);
27
28         if (h[i] < 1.0e-15) { h[i] = 1.0e-15; }
29       }
30     }
31
32     if (mode_ == 2)
33     {
34       if (teq[1] > 1.0e-15)
35       {
36         for (idx_t i = nam_; i < nom_; i++)
37         {
38           h[i] = ho[i] * exp(S[1] + (mb_ * p) / tob) *
39
40             (teq[1] / tob) / sinh(teq[1] / tob);
41
42           if (h[i] < 1.0e-15) { h[i] = 1.0e-15; }
43         }
44       }
45     }
46   }
47
48   // For the full EGP model viscosity
49
50   else
51   {
52     if (teq[0] > 1.0e-15)
53     {
54       dHoa = (dHconsta_ - CdH1a_) + CdH1a_ *
55
56         tanh(CdH2a_ * (htBnon - CdH3a_)) +
57
58         CdH4a_ * pow(htB, 2) + SHa_ * Rg[0];
59
60       for (idx_t i = 0; i < nam_; i++)
61       {
62         ho[i] = nconst_[i] * exp(-Cn1a_ + Cn1a_ *
63
64           tanh(Cn2a_ *(htBnon - Cn3a_))) *
65
66           exp(Cn4a_ * pow(htB, 2));
67
68         h[i] = ho[i] * exp(dHoa / R_ * (1 / T_ - 1 / T_base_a_)) *
69

```

```

70         exp(S[0]) * exp(ma_ * p / toa) *
71         (teq[0] / toa / sinh(teq[0] / toa));
72
73     if (h[i] < 1.0e-15)
74     {
75         h[i] = 1.0e-15;
76     }
77 }
78 }
79 }
80
81 if (mode_ == 2)
82 {
83     if (teq[1] > 1.0e-15)
84     {
85
86         dHob = dHconstb_ + CdH4b_ * pow(htB, 2) + SHb_ * Rg[1];
87
88         for (idx_t i = nam_; i < nom_; i++)
89         {
90             ho[i] = nconst_[i] * exp(Cn4b_ * pow(htB, 2));
91
92             h[i] = ho[i] * exp(dHob / R_ * (1 / T_ - 1 / T_base_b_ )) *
93                 exp(S[1]) * exp(mb_ * p / tob) *
94                 (teq[1] / tob / sinh(teq[1] / tob));
95
96             if (h[i] < 1.0e-15)
97             {
98                 h[i] = 1.0e-15;
99             }
100         }
101     }
102 }
103 }
104 }
105 }
106 }

```



## LARGER TEMPERATURE AND STRAIN RATE RANGE STRESS-STRAIN CURVES

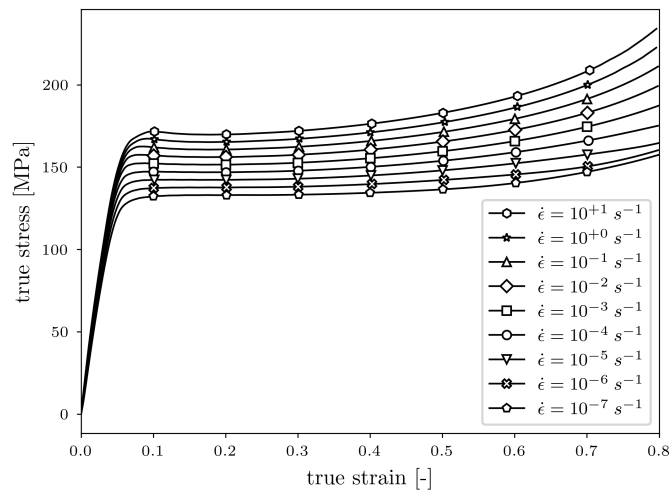


Figure F.1: The updated EGP model results for a large strain-rate range at  $-20^{\circ}\text{C}$ .

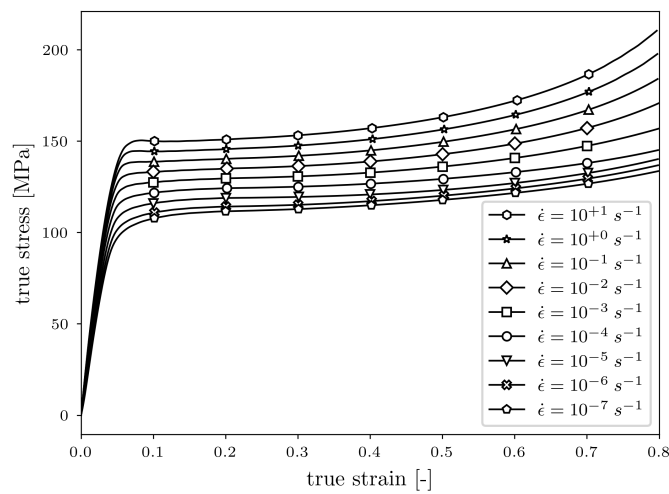


Figure F.2: The updated EGP model results for a large strain-rate range at  $20^{\circ}\text{C}$ .

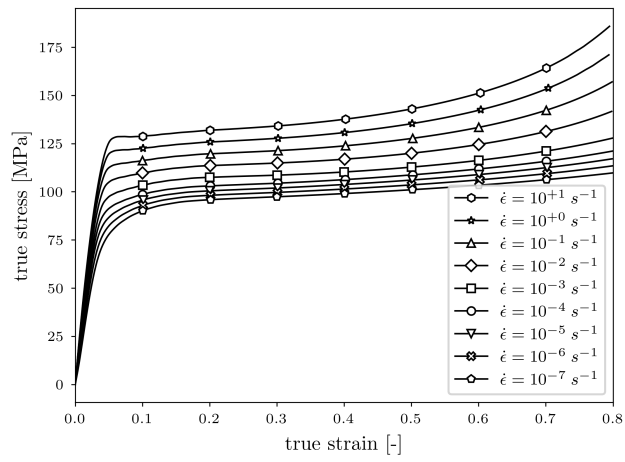


Figure F.3: The updated EGP model results for a large strain-rate range at 60°C.

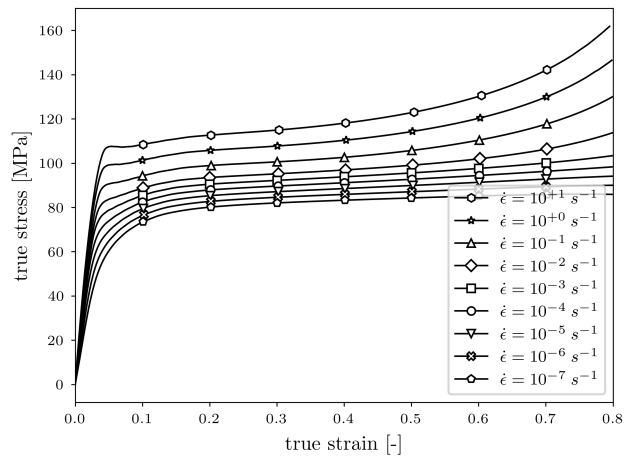


Figure F.4: The updated EGP model results for a large strain-rate range at 100°C.

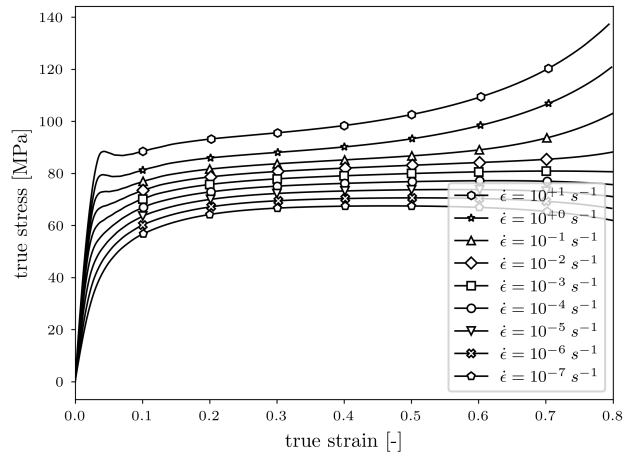


Figure F.5: The updated EGP model results for a large strain-rate range at 140°C.

## DERIVATIVE OF THE VISCOSITY

The derivative of the viscosity function as given in Equation 4.8 with respect to the deformation gradient is determined in this appendix. Firstly, the viscosity function is split in three sub-functions:

$$\eta_{x,i} = \underbrace{\eta_{0_{x,i}}(I_r)}_{f_1(F)} \underbrace{\frac{\bar{\tau}_x / \tau_{0_x}}{\sinh(\bar{\tau}_x / \tau_{0_x})}}_{f_2(F)} \underbrace{\exp\left(\frac{\Delta H_x(I_r)}{R} \left(\frac{1}{T} - \frac{1}{T_{x,base}}\right) + \frac{\mu_x p}{\tau_{0_x}}\right)}_{f_3(F)} \exp(S_x) \quad (\text{G.1})$$

The following derivative has to be calculated:

$$\frac{\partial \eta_{x,i}}{\partial \mathbf{F}} = \exp(S_x) \left[ (f_1(F) f_2'(F) + f_2(F) f_1'(F)) \cdot f_3(F) + f_1(F) f_2(F) f_3'(F) \right] \quad (\text{G.2})$$

The following evolution for the Ree-Eyring parameters has been introduced (for the alpha process):

$$\tau_{0_\alpha} = \frac{k_B T}{(V_{const,\alpha} - C_{V,1,\alpha}) + C_{V,1,\alpha} \cdot \tanh(C_{V,2,\alpha} \cdot (I_{r,non}(\tilde{\mathbf{B}}) - C_{V,3,\alpha})) + C_{V,4,\alpha} I_r^2(\tilde{\mathbf{B}})} \quad (\text{G.3})$$

$$\Delta H_{0_\alpha} = (\Delta H_{const,\alpha} - C_{\Delta H,1,\alpha}) + C_{\Delta H,1,\alpha} \cdot \tanh(C_{\Delta H,2,\alpha} \cdot (I_{r,non}(\tilde{\mathbf{B}}) - C_{\Delta H,3,\alpha})) + C_{\Delta H,4,\alpha} I_r^2(\tilde{\mathbf{B}}) + S_{H_\alpha} R \gamma_\alpha(\bar{\gamma}_p) \quad (\text{G.4})$$

$$\eta_{0_{\alpha,i}} = \eta_{const,\alpha,i} \cdot \exp(-C_{\eta,1,\alpha} + C_{\eta,1,\alpha} \cdot \tanh(C_{\eta,2,\alpha} \cdot (I_{r,non}(\tilde{\mathbf{B}}) - C_{\eta,3,\alpha}))) \cdot \exp(C_{\eta,4,\alpha} I_r^2(\tilde{\mathbf{B}})) \quad (\text{G.5})$$

Since  $I_r(\tilde{\mathbf{B}})$  is dependent on the deformation gradient, the derivative of Equations G.3-G.5 with respect to the deformation gradient is determined:

$$\frac{\partial \tau_{0_x}}{\partial \mathbf{F}} = -\frac{\tau_{0_x}^2}{k_B T} \left( E_{V,x,low} \frac{\partial I_{r,non}}{\partial \mathbf{F}} + E_{V,x,high} \frac{\partial I_r}{\partial \mathbf{F}} \right) \quad (\text{G.6})$$

$$\frac{\partial \Delta H_{0_x}}{\partial \mathbf{F}} = E_{\Delta H,x,low} \frac{\partial I_{r,non}}{\partial \mathbf{F}} + E_{\Delta H,x,high} \frac{\partial I_r}{\partial \mathbf{F}} \quad (\text{G.7})$$

$$\frac{\partial \eta_{0_{x,i}}}{\partial \mathbf{F}} = \eta_{0_{x,i}} \left( E_{\eta,x,low} \frac{\partial I_{r,non}}{\partial \mathbf{F}} + E_{\eta,x,high} \frac{\partial I_r}{\partial \mathbf{F}} \right) \quad (\text{G.8})$$

where for  $k = \eta, \Delta H$  or  $V$  and  $x = \alpha$  or  $\beta$ :

$$E_{k,\alpha,low} = C_{k,1,\alpha} C_{k,2,\alpha} \cdot \text{sech}^2(C_{k,2,\alpha} \cdot (I_{r,non} - C_{k,3,\alpha})) \quad (\text{G.9})$$

$$E_{k,\alpha,high} = C_{k,4,\alpha} 2I_r \quad (\text{G.10})$$

$$E_{k,\beta,low} = 0 \quad (\text{G.11})$$

$$E_{k,\beta,high} = C_{k,4,\beta} 2I_r \quad (\text{G.12})$$

Calculate  $f'_1(\mathbf{F})$ ,  $f'_2(\mathbf{F})$  and  $f'_3(\mathbf{F})$ :

$$f'_1(\mathbf{F}) = \frac{\partial \eta_{0,x,i}}{\partial \mathbf{F}} = f_1(\mathbf{F}) \left( E_{\eta,x,low} \frac{\partial I_{r,non}}{\partial \mathbf{F}} + E_{\eta,x,high} \frac{\partial I_r}{\partial \mathbf{F}} \right) \quad (\text{G.13})$$

$$f'_2(\mathbf{F}) = \frac{\tau_{0,x} - \bar{\tau}_x \coth \frac{\bar{\tau}_x}{\tau_{0,x}} \operatorname{csch} \frac{\bar{\tau}_x}{\tau_{0,x}} \frac{\partial \bar{\tau}_x}{\partial \mathbf{F}}}{\tau_{0,x}^2} - \frac{\bar{\tau}_x \left( \bar{\tau}_x \coth \frac{\bar{\tau}_x}{\tau_{0,x}} - \tau_{0,x} \right) \operatorname{csch} \frac{\bar{\tau}_x}{\tau_{0,x}}}{\tau_{0,x}^3} \cdot \frac{\tau_{0,x}^2}{k_B T} \left( E_{V,x,low} \frac{\partial I_{r,non}}{\partial \mathbf{F}} + E_{V,x,high} \frac{\partial I_r}{\partial \mathbf{F}} \right) \quad (\text{G.14})$$

$$f'_3(\mathbf{F}) = \left[ \left( \frac{E_{\Delta H,x,low}}{R} \left( \frac{1}{T} - \frac{1}{T_{x,base}} \right) + \frac{\mu_x p E_{V,x,low}}{k_B T} \right) \frac{\partial I_{r,non}}{\partial \mathbf{F}} + \left( \frac{E_{\Delta H,x,high}}{R} \left( \frac{1}{T} - \frac{1}{T_{x,base}} \right) + \frac{\mu_x p E_{V,x,high}}{k_B T} \right) \frac{\partial I_r}{\partial \mathbf{F}} + \frac{\mu_x}{\tau_{0,x}} \frac{\partial p}{\partial \mathbf{F}} \right] \cdot f_3(\mathbf{F}) \quad (\text{G.15})$$

Substitute all needed functions in equation G.2:

$$\begin{aligned} \frac{\partial \eta_{x,i}}{\partial \mathbf{F}} &= \exp(S_x) f_1(\mathbf{F}) f_2(\mathbf{F}) f_3(\mathbf{F}) \cdot \\ &\left[ \frac{\tau_{0,x} - \bar{\tau}_x \coth \frac{\bar{\tau}_x}{\tau_{0,x}} \operatorname{csch} \frac{\bar{\tau}_x}{\tau_{0,x}} \frac{\partial \bar{\tau}_x}{\partial \mathbf{F}}}{\tau_{0,x}^2 f_2(\mathbf{F})} - \frac{\bar{\tau}_x \left( \bar{\tau}_x \coth \frac{\bar{\tau}_x}{\tau_{0,x}} - \tau_{0,x} \right) \operatorname{csch} \frac{\bar{\tau}_x}{\tau_{0,x}}}{\tau_{0,x}^3 f_2(\mathbf{F})} \cdot \frac{\tau_{0,x}^2}{k_B T} \left( E_{V,x,low} \frac{\partial I_{r,non}}{\partial \mathbf{F}} + E_{V,x,high} \frac{\partial I_r}{\partial \mathbf{F}} \right) + \right. \\ &E_{\eta,x,low} \frac{\partial I_{r,non}}{\partial \mathbf{F}} + E_{\eta,x,high} \frac{\partial I_r}{\partial \mathbf{F}} + \\ &\left. \left( \frac{E_{\Delta H,x,low}}{R} \left( \frac{1}{T} - \frac{1}{T_{x,base}} \right) + \frac{\mu_x p E_{V,x,low}}{k_B T} \right) \frac{\partial I_{r,non}}{\partial \mathbf{F}} + \left( \frac{E_{\Delta H,x,high}}{R} \left( \frac{1}{T} - \frac{1}{T_{x,base}} \right) + \frac{\mu_x p E_{V,x,high}}{k_B T} \right) \frac{\partial I_r}{\partial \mathbf{F}} + \frac{\mu_x}{\tau_{0,x}} \frac{\partial p}{\partial \mathbf{F}} \right] \quad (\text{G.16}) \end{aligned}$$

The following result is obtained:

$$\frac{\partial \eta_{x,i}}{\partial \mathbf{F}} = \eta_{x,i} \left[ \frac{\mu_x}{\tau_{0,x}} \frac{\partial p}{\partial \mathbf{F}} + \left( \frac{1}{\bar{\tau}_x} - \frac{\coth \left( \frac{\bar{\tau}_x}{\tau_{0,x}} \right)}{\tau_{0,x}} \right) \frac{\partial \bar{\tau}_x}{\partial \mathbf{F}} + M_{x,low} \frac{\partial I_{r,non}}{\partial \mathbf{F}} + M_{x,high} \frac{\partial I_r}{\partial \mathbf{F}} \right] \quad (\text{G.17})$$

For  $d = low$  or  $high$  and  $x = \alpha$  or  $\beta$ :

$$M_{x,d} = E_{\eta,x,d} + \frac{E_{\Delta H,x,d}}{R} \left( \frac{1}{T} - \frac{1}{T_{x,base}} \right) + \frac{\mu_x p E_{V,x,d}}{k_B T} - \frac{E_{V,x,d} \tau_{0,x}}{k_B T} \left( \frac{\bar{\tau}_x \coth \left( \frac{\bar{\tau}_x}{\tau_{0,x}} \right)}{\tau_{0,x}} - 1 \right) \quad (\text{G.18})$$

## UPDATED C++ CODE FOR THE STIFFNESS CALCULATION

---

Code H.1: The updated C++ code for the calculation of the stiffness tensor

```

1 //-----
2 //  update the tangent stiffness matrix
3 //-----
4
5 void EGPMaterial::stiffness_
6
7     (const Matrix& Stiff, const M33& mF, const M33& mFB, M33& mtB,
8
9     const Array<M33>& mtBe, const Array<M33>& mtBeB,
10
11     const Vector& h, const Vector& G, const Vector& mteq,
12
13     const Vector& lambda, const Vector& teq, double J, double JB,
14
15     const M33 DF, const M33 mSs, const M33 mSsa, const M33 mSsb,
16
17     const double& dt, Array<M33>& mbsdi, double& eqps, double htB,
18
19     double htBnon, Matrix mat)
20
21 {
22     // define all variables
23
24     idx_t noe = nom_ + 1; // number of equations
25
26
27     M33  mI, mtF, mtFB, mtC, mFi, mtBeBi, mCp, mCpi, mtBed, mM;
28
29     M33  mB, mC, mdgdF, mbsd1t, mdfdF, mdssdgtmp, mdssdg;
30
31
32     M91  ccdgdF, ccda1dF, ccbsd1t, ccbsd1, ccdI2dF;
33
34     M91  ccSsta, ccSsa, ccSstb, ccSsb, ccFit, cctBt;
35
36     M91  ccdssdg, ccdssdgtmp, ccdssdgtmp2, ccdhtBdF;
37
38     M91  ccdfdF, ccdpdF, ccdtadF, ccdtbdF, ccdhtBnondF;
39
40     M91  ccI, ccF, ccFi, cctB, ccTemp;
41
42     M91  cctBe, ccB, ccdI1dF, ccIt;
43
44
45     M99  mmI, mmtF, mmtFt, mmFt, mmSda, mmSdb, mmtFc;
46
47     M99  mmStiffh, mmStiffd, mmHic, mmStiff, mmStiffx;
48
49     M99  mmStiffc, mmStiffR, mmStress, mmtFcr, mmTemp;

```

```

50 M99 mmK, mmM, mmMc, mmMcr, mmFtr, mmds1dFc, mmB21c;
51
52 M99 mmF4, mmKtot, mmSdatmp, mmSdbtmp, mmds1dF;
53
54 M99 mmStiffdac, mmStiffdbc, mmStiffda, mmStiffdb;
55
56 M99 mmF, mmFc, mmFcr, mmdtBdF, mmHi, mmSda2tmp;
57
58 M99 mmtFtc, mmtFtcr, mmC4r, mmF4r, mmdtBdFr;
59
60
61 Array <M91> cctBed(nom_), ccdndF(nom_);
62
63
64 Array <M99> mmA1(nom_), mmA2(nom_);
65
66 Array <M99> mmB2(nom_), mmB1(nom_), mmC4(nom_);
67
68
69 Array <M33> mCpB(nom_);
70
71
72 Array<double,3> matdsdx(3, 3, noe);
73
74 Array<double,3> matdxdf(noe, 3, 3);
75
76 Array<double,3> matstiffxtmp(3,3, noe);
77
78 Array<double,4> matstiffx(3,3,3,3);
79
80
81 Matrix mati(noe, noe);
82
83
84 double trmtBe, deqpsdt, dSdea, dSdeb;
85
86 double p, toa, tob, Vacta, Vactb, Jn;
87
88 double Enalpha_low, Enalpha_high, Enbeta;
89
90 double EdHalp_low, EdHalp_high, EdHbeta;
91
92 double EValpha_low, EValpha_high, EVbeta;
93
94 double trmtB, Egalp, Egbeta;
95
96
97 Vector gamma(nom_);
98
99 gamma = G / h;
100
101 // initialize second and fourth order unit tensors
102 // convert them to corresponding column vectors
103
104 inimI(mI);
105 m2cc(ccI, mI, 9); // different than Voigt representation
106
107 inimI4(mml);
108
109 // calculate kinetic variables
110
111 mtF = mF / pow(J, 1. / 3.);
112
113 mtFB = mFB / pow(JB, 1. / 3.);
114
115 mtC = matmul(mtF.transpose(), mtF);
116
117 mFi = inverse(mF);
118
119 m2cc(ccF, mF, 9);
120

```

```

121 m2cc (ccFi, mFi, 9);
122
123 m2cc (ccFit, mFi.transpose(), 9);
124
125 m2nm (mmtF, mtF, 9);
126
127 mm2nmc (mmtFc, mmtF, 9);
128
129 mm2nmr (mmtFcr, mmtFc, 9);
130
131 m2nm (mmtFt, mtF.transpose(), 9);
132
133 m2nm (mmFt, mF.transpose(), 9);
134
135 mm2nmr (mmFtr, mmFt, 9);
136
137 for (idx_t i = 0; i < nom_; i++)
138 {
139     mtBeBi = inverse ( mtBeB[i] );
140
141     mCpB[i] = matmul (mtFB.transpose(), matmul ( mtBeBi, mtFB ) );
142
143     mCp = (1. - lambda[i]) * mtC + lambda[i] * mCpB[i];
144
145     mCpi = inverse (mCp);
146
147     trace (mtBe[i], trmtBe );
148
149     mtBed = mtBe[i] - 1. / 3. * trmtBe * mI;
150
151     ccTemp = 0.0;
152
153     m2cc (ccTemp, mtBed, 9);
154
155     cctBed[i] = ccTemp;
156
157     mM = matmul (mtF, mCpi);
158
159     m2nm (mmM, mM, 9);
160
161     mm2nmc (mmMc, mmM, 9);
162
163     mm2nmr (mmMcr, mmMc, 9);
164
165     mmA1[i] = mmMcr + mmMc;
166
167     mmA2[i] = -1. * matmul (mmM, mmMcr);
168 }
169
170 mmF4 = -1. / 3. / pow (J, 1./3.) * matmul (ccF, ccFi.transpose()) +
171     1. / pow (J, 1./3.) * mml;
172
173
174
175 // Determine the Ree–Eyring parameters and related derivatives
176 // Determine the activation volume and tau_0 parameters
177
178 if ( strHardening_ == "NEOHOOKEAN" )
179 {
180     toa = toa_;
181
182     tob = tob_;
183 }
184 else
185 {
186     Vacta = (Vconsta_ - CV1a_) + CV1a_ * tanh (CV2a_ * (htBnon - CV3a_)) +
187         CV4a_ * pow(htB, 2.);
188
189     Vactb = Vconstb_ + CV4b_ * pow(htB, 2.);
190
191

```

```

192   toa = kb_ * T_ / Vacta;
193
194   tob = kb_ * T_ / Vactb;
195 }
196
197 // Determine E-factors related to Ree-Eyring parameters evolution
198
199 Enalpha_low = Cn1a_ * Cn2a_ *
200               pow ( 1. / (cosh (Cn2a_ * (htBnon - Cn3a_))), 2.);
201
202 Enalpha_high = Cn4a_ * 2. * htB;
203
204 Enbeta = Cn4b_ * 2. * htB;
205
206 EdHalp_low = CdH1a_ * CdH2a_ *
207              pow ( 1. / (cosh (CdH2a_ * (htBnon - CdH3a_))), 2.);
208
209 EdHalp_high = CdH4a_ * 2. * htB;
210
211 EdHbeta = CdH4b_ * 2. * htB;
212
213 EValpha_low = CV1a_ * CV2a_ *
214              pow ( 1. / (cosh (CV2a_ * (htBnon - CV3a_))), 2.);
215
216 EValpha_high = CV4a_ * 2. * htB;
217
218 EVbeta = CV4b_ * 2. * htB;
219
220 Egalpha = CG1a_ * CG2a_ *
221           pow ( 1. / (cosh (CG2a_ * (htBnon - CG3a_))), 2.);
222
223 Egbeta = 0.;
224
225 // derivative of left Cauchy-Green deformation tensor wrt def.grad.
226
227 m2mm(mmF,mF,9);
228
229 mm2mmc (mmFc, mmF, 9);
230
231 mm2mmr (mmFcr, mmFc, 9);
232
233 mB = matmul (mF, mF.transpose());
234
235 m2cc (ccB, mB, 9);
236
237 mmdtBdF = pow (J, -2.0 / 3.0) * ( ( mmFc + mmFcr ) -
238                               2.0 / 3.0 * matmul(ccB, ccFit.transpose()) );
239
240 // Derivative first invariant wrt the deformation gradient
241
242 cc2cct(ccIt, ccI, 9);
243
244 ccdI1dF = matmul (ccIt.transpose(), mmdtBdF).transpose();
245
246 // Derivative of second invariant wrt the deformation gradient
247
248 trace (mtB, trmtB); // First invariant of mtB
249
250 m2cc(cctB, mtB, 9);
251
252 cc2cct(cctBt, cctB, 9);
253
254 mm2mmr (mmdtBdFr, mmdtBdF, 9);
255
256 ccdI2dF = trmtB * ccdI1dF - 0.5 * (matmul(mmdtBdFr, cctBt) +
257                                   matmul(cctB.transpose(), mmdtBdF).transpose());
258
259 // Derivative invariant function wrt the deformation gradient
260
261 if (std::isnan(htB)) {htB = 1e-20;}
262 if (std::isnan(htBnon)) {htBnon = 1e-20;}

```

```

263 if (htB < 1e-20 && -1e-20 < htB) {htB = 1e-20;}
264 if (htBnon < 1e-20 && -1e-20 < htBnon) {htBnon = 1e-20;}
265
266 ccdhtBdF = (2. / 3. * trmtB * ccdI1dF - ccdI2dF) /
267           (2. * htB) ; // Derivative of I_r
268
269 if (htBnon == htB)
270 {
271   ccdhtBnondF = (2. / 3.* trmtB * ccdI1dF - ccdI2dF) /
272               (2. * htBnon) ; // Derivative of I_r-non
273 }
274 else
275 {
276   ccdhtBnondF = 0.;
277 }
278
279
280 //-----
281 //   hardening stiffness
282 //-----
283
284 if ( strHardening_ == "NEOHOOKEAN" )
285 {
286   mmTemp = mmtFcr + mmtFc - 2. / 3. *
287
288           matmul(matmul(ccI , ccI.transpose() ) ,mmtFc) ;
289
290   mmStiffrr = Gr_ * matmul(mmTemp,mmF4) ;
291 }
292 else
293 {
294   edvilStiff_ (mmStiffrr , mtB, mB, mF, J) ;
295 }
296
297 //-----
298 //   hydrostatic stiffness
299 //-----
300
301 mmStiffhh = k_ * J * matmul (ccI , ccFit.transpose()) ;
302
303 //-----
304 //   deviatoric stiffness
305 //-----
306
307 mmSdatmp = 0.0 ;
308 mmSdaztmp = 0.0 ;
309 mmSdbtmp = 0.0 ;
310
311 mmzmmc (mmtFtc , mmtFt, 9) ;
312
313 mmzmmr (mmtFtcr , mmtFtc, 9) ;
314
315 mmzmmr(mmF4r , mmF4, 9) ;
316
317 mmHi = mmI - 1.0 / 3.0 * matmul (ccI , ccI.transpose()) ;
318
319 mmzmmc(mmHic , mmHi, 9) ;
320
321 // Determine the deviatoric stiffness tensor
322
323 for (idx_t i = 0; i < nam_ ; i++) // For alpha process
324 {
325   mmC4[i] = (1.0 - lambda[i]) * (mmtFtcr + mmtFtc) ;
326
327   mmzmmr(mmC4r , mmC4[i] , 9) ;
328
329   mmB1[i] = mmA1[i] + matmul (mmA2[i] , mmC4r) ;
330
331   mmB2[i] = matmul (mmB1[i] , mmF4r) ;
332
333   mmSdatmp += mmB2[i] * G[i] ;

```

```

334     mmSdztmp += -1. * Gconst_[i] * Egalpha *
335               matmul (cctBed[i], ccdhtBnondF.transpose());
336   }
337
338   mmStiffda = matmul (mmHic, mmSdatmp) + mmSdztmp;
339
340   for (idx_t i = nam_; i < nom_; i++) // For beta process
341   {
342     mmC4[i] = (1.0 - lambda[i]) * (mmtFtcr + mmtFtc);
343
344     mmzmmr(mmC4r, mmC4[i], 9);
345
346     mmB1[i] = mmA1[i] + matmul (mmA2[i], mmC4r);
347
348     mmB2[i] = matmul (mmB1[i], mmF4r);
349
350     mmSdbtmp += mmB2[i] * G[i];
351   }
352
353   mmStiffdb = matmul (mmHic, mmSdbtmp);
354
355   // Add the alpha and beta contribution
356
357   mmStiffd = mmStiffda + mmStiffdb;
358
359
360   //-----
361   //   State variable
362   //-----
363
364   // Derivative dev. stress wrt the state variables
365
366   matdsdx = 0.0;
367
368   for (idx_t k = 0; k < nom_; k++)
369   {
370     mdssdgtmp = mCpB[k] - mtC;
371
372     m2cc (ccdssdgtmp, mdssdgtmp, 9);
373
374     ccdssdgtmp2 = matmul (mmA2[k], ccdssdgtmp);
375
376     ccdssdg = G[k] * matmul (mmHic, ccdssdgtmp2);
377
378     cc2m(mdssdg, ccdssdg, 9);
379
380     for (idx_t i = 0; i < 3; i++)
381     {
382       for (idx_t j = 0; j < 3; j++)
383       {
384         matdsdx(i, j, k) = mdssdg(i, j);
385       }
386     }
387   }
388
389   // Derivative total equivalent stress wrt the the deformation gradient
390
391   m2cc(ccSsa, mSsa, 9);
392
393   cc2cct(ccSsta, ccSsa, 9);
394
395   m2cc(ccSsb, mSsb, 9);
396
397   cc2cct(ccSstb, ccSsb, 9);
398
399   mmzmmc(mmStiffdac, mmStiffda, 9);
400
401   mmzmmc(mmStiffdbc, mmStiffdb, 9);
402
403   if (teq[0] > 1.0e-15) // For alpha process
404

```

```

405 {
406     ccdtadF = 1. / (4. * teq[0]) * (matmul(mmStiffdac, ccSsa) +
407         matmul(ccSsta.transpose(), mmStiffda).transpose());
408 }
409 else
410 {
411     ccdtadF = 0.;
412 }
413
414 if (teq[1] > 1.0e-15) // For beta process
415 {
416     ccdtbdF = 1. / (4. * teq[1]) * (matmul(mmStiffdbc, ccSsb) +
417         matmul(ccSstb.transpose(), mmStiffdb).transpose());
418 }
419 else
420 {
421     ccdtbdF = 0.;
422 }
423
424 // Derivative pressure wrt the deformation gradient
425
426 ccdpdF = -1. * k_ * J * ccFit;
427
428 // Determine pressure
429
430 p = -1. * k_ * (J - 1.);
431
432 // Derivative of viscosity wrt the deformation gradient
433
434 if (teq[0] > 1.0e-15)
435 {
436     for (idx_t i = 0; i < nam_; i++) // For alpha process
437     {
438         ccdndF[i] = h[i] * ((Enalpha_low +
439             EdHalpha_low / R_ * (1. / T_ - 1. / T_base_a_)
440             + ma_ * EValpha_low * p / (kb_ * T_) -
441             EValpha_low * toa / (kb_ * T_) *
442             (teq[0] * (1. / tanh(teq[0] / toa)) / toa - 1.)) * ccdhtBnondF +
443             (Enalpha_high + EdHalpha_high / R_ * (1. / T_ - 1. / T_base_a_) +
444             ma_ * EValpha_high * p / (kb_ * T_) -
445             EValpha_high * toa / (kb_ * T_) *
446             (teq[0] * (1. / tanh(teq[0] / toa)) / toa - 1.)) * ccdhtBdF +
447             ma_ / toa * ccdpdF +
448             (1. / teq[0] - (1. / tanh(teq[0] / toa)) / toa) * ccdtadF);
449     }
450 }
451 else
452 {
453     for (idx_t i = 0; i < nam_; i++)
454     {
455         ccdndF[i] = 0.;
456     }
457 }
458
459 if (teq[1] > 1.0e-15)
460 {
461     for (idx_t i = nam_; i < nom_; i++) // For beta process
462     {
463         ccdndF[i] = h[i] * ((Enbeta +
464             EdHbeta / R_ * (1 / T_ - 1 / T_base_b_) +
465             mb_ * EVbeta * p / (kb_ * T_) -
466             EVbeta * tob / (kb_ * T_) *
467             (teq[1] * (1. / tanh(teq[1] / tob)) / tob - 1.)) * ccdhtBdF +
468             mb_ / tob * ccdpdF +
469             (1. / teq[1] - (1. / tanh(teq[1] / tob)) / tob) * ccdtbdF);
470     }
471 }
472 else
473 {
474     for (idx_t i = 0; i < nam_; i++)
475     {

```

```

476     ccdndF[i] = 0.;
477     }
478 }
479
480 // Derivative of f wrt the deformation gradient
481
482 matdxdF = 0.0;
483
484 for (idx_t m = 0; m < nam_; m++) // For alpha process
485 {
486     ccdfdF = lambda[m] * dt * (-Gconst_[m] * Egalpha * ccdhtBnondF / h[m] -
487         G[m] / pow(h[m], 2.) * ccdndF[m]);
488
489     cc2m(mdfdF, ccdfdF, 9);
490
491     for (idx_t q = 0; q < 3; q++)
492     {
493         for (idx_t r = 0; r < 3; r++)
494         {
495             matdxdF(m,q,r) = mdfdF(q,r);
496         }
497     }
498 }
499
500 for (idx_t m = nam_; m < nom_; m++) // For beta process
501 {
502     ccdfdF = lambda[m] * dt * (-Gconst_[m] * Egbeta * ccdhtBnondF / h[m] -
503         G[m] / pow(h[m], 2.) * ccdndF[m]);
504
505     cc2m(mdfdF, ccdfdF, 9);
506
507     for (idx_t q = 0; q < 3; q++)
508     {
509         for (idx_t r = 0; r < 3; r++)
510         {
511             matdxdF(m,q,r) = mdfdF(q,r);
512         }
513     }
514 }
515
516 // derivative of dev. stress alpha,1 wrt the deformation gradient
517
518 mm2mmc (mmB21c, mmB2[0], 9);
519
520 mmds1dF = G[0] * matmul(mmH1c, mmB21c) - Gconst_[0] * Egalpha *
521     matmul (cctBed [0], ccdhtBnondF.transpose());
522
523 // derivative of total eq. stress alpha wrt the deformation gradient
524
525 mbsd1t = mbsdi[0].transpose();
526
527 m2cc (ccbsd1, mbsdi[0], 9);
528
529 m2cc (ccbsd1t, mbsd1t, 9);
530
531 mm2mmc(mmds1dFc, mmds1dF, 9);
532
533 if (mteq[0] > 1.0e-15)
534 {
535     ccdta1dF = 1. / (4. * mteq[0]) * (matmul(mmds1dFc, ccbsd1) +
536         matmul(ccbsd1t.transpose(), mmds1dF).transpose());
537 }
538 else
539 {
540     ccdta1dF = 0;
541 }
542
543 // derivative of g wrt the deformation gradient
544
545 ccdgdF = -1. * dt * (1. / h[0] * ccdta1dF -
546     mteq[0] / pow(h[0], 2.) * ccdndF[0]);

```

```

547 cczm (mdgdF, ccdgdF, 9);
548
549 for (idx_t q = 0; q < 3; q++)
550 {
551     for (idx_t r = 0; r < 3; r++)
552     {
553         matdxdF(noe - 1, q, r) = mdgdF(q, r);
554     }
555 }
556
557 // Determine the state variable stiffness tensor
558 // derivative of state parameter wrt equivalent plastic strain
559
560 calcDSDeqps_ ( dSdea, dSdeb, eqps);
561
562 // calculate Jacobi matrix and its inverse
563
564 matstiffx = 0.0;
565 mmStiffx = 0.0;
566
567 deqpsdt = mteq[0] / h[0];
568
569 // Only calculate the Jacobian if it has not been done in
570 // the stress calculation
571
572 Jn = jem::numeric::det( DF );
573
574 if (Jn == 1.0 )
575 {
576     jacobimat_ (mat, gamma, lambda, mteq, teq, noe,
577                deqpsdt, dt, dSdea, dSdeb, toa, tob);
578 }
579
580 double Jmat = jem::numeric::det( mat ); // Check if Jacobian is singular
581
582 if ( Jmat != 0.0 && !std::isnan(Jmat))
583 {
584     mati = jem::numeric::inverse (mat);
585     TensorIndex i, j, k, m, q, r;
586     matstiffxtmp (i, j, m) = -1. * dot ( matdsdx(i, j, k) , mati(k, m), k );
587     matstiffx (i, j, q, r) = dot ( matstiffxtmp(i, j, m) , matdxdF(m, q, r), m );
588 }
589 else
590 {
591     matstiffx = 0.;
592 }
593
594 matzmm (mmStiffx, matstiffx, 9);
595
596 // -----
597 // calculate stress stiffness tensor
598 // -----
599
600 // adding the 4 parts together
601
602 mmStiff = mmStiffh + mmStiffd + mmStiffr + mmStiffx;
603
604 // shift columns in stiffness matrix
605
606 mmzmmc (mmStiffc, mmStiff, 9);
607
608 mmKtot = matmul (mmStiffc, mmFtr);
609
610 if ( stateString_ == "PLANE_STRAIN" )
611 {

```

```

618     Stiff(0,0) = mmKtot(0,0);
619     Stiff(1,0) = .5 * ( mmKtot(1,0) + mmKtot(0,1) );
620     Stiff(2,0) = .5 * ( mmKtot(3,0) + mmKtot(0,3) );
621     Stiff(0,1) = Stiff(1,0);
622     Stiff(1,1) = mmKtot(1,1);
623     Stiff(2,1) = .5* ( mmKtot(3,1) + mmKtot(1,3) );
624     Stiff(0,2) = Stiff(2,0);
625     Stiff(1,2) = Stiff(2,1);
626     Stiff(2,2) = mmKtot(3,3);
627 }
628
629 else if ( stateString_ == "AXISYMMETRIC" )
630 {
631     Stiff(0,0) = mmKtot(0,0);
632     Stiff(1,0) = .5 * ( mmKtot(1,0) + mmKtot(0,1) );
633     Stiff(2,0) = .5 * ( mmKtot(3,0) + mmKtot(0,3) );
634     Stiff(3,0) = .5 * ( mmKtot(2,0) + mmKtot(0,2) );
635     Stiff(0,1) = Stiff(1,0);
636     Stiff(1,1) = mmKtot(1,1);
637     Stiff(2,1) = .5 * ( mmKtot(3,1) + mmKtot(1,3) );
638     Stiff(3,1) = .5 * ( mmKtot(2,1) + mmKtot(1,2) );
639     Stiff(0,2) = Stiff(2,0);
640     Stiff(1,2) = Stiff(2,1);
641     Stiff(2,2) = mmKtot(3,3);
642     Stiff(3,2) = .5 * ( mmKtot(3,2) + mmKtot(2,3) );
643     Stiff(0,3) = Stiff(3,0);
644     Stiff(1,3) = Stiff(3,1);
645     Stiff(2,3) = Stiff(3,2);
646     Stiff(3,3) = mmKtot(2,2);
647 }
648 else
649 {
650     Stiff(0,0) = mmKtot(0,0);
651     Stiff(0,1) = .5 * ( mmKtot(0,1) + mmKtot(1,0) );
652     Stiff(0,2) = .5 * ( mmKtot(0,2) + mmKtot(2,0) );
653     Stiff(0,3) = .5 * ( mmKtot(0,3) + mmKtot(0,4) );
654     Stiff(0,4) = .5 * ( mmKtot(0,5) + mmKtot(0,6) );
655     Stiff(0,5) = .5 * ( mmKtot(0,7) + mmKtot(0,8) );
656     Stiff(1,0) = Stiff(0,1);
657     Stiff(1,1) = mmKtot(1,1);
658     Stiff(1,2) = .5 * ( mmKtot(1,2) + mmKtot(2,1) );
659     Stiff(1,3) = .5 * ( mmKtot(1,3) + mmKtot(1,4) );
660     Stiff(1,4) = .5 * ( mmKtot(1,5) + mmKtot(1,6) );
661     Stiff(1,5) = .5 * ( mmKtot(1,7) + mmKtot(1,8) );
662     Stiff(2,0) = Stiff(0,2);
663     Stiff(2,1) = Stiff(1,2);
664     Stiff(2,2) = mmKtot(2,2);
665     Stiff(2,3) = .5 * ( mmKtot(2,3) + mmKtot(2,4) );
666     Stiff(2,4) = .5 * ( mmKtot(2,5) + mmKtot(2,6) );
667     Stiff(2,5) = .5 * ( mmKtot(2,7) + mmKtot(2,8) );
668     Stiff(3,0) = Stiff(0,3);
669     Stiff(3,1) = Stiff(1,3);
670     Stiff(3,2) = Stiff(2,3);
671     Stiff(3,3) = .5 * ( mmKtot(3,3) + mmKtot(3,4) );
672     Stiff(3,4) = .5 * ( mmKtot(3,5) + mmKtot(3,6) );
673     Stiff(3,5) = .5 * ( mmKtot(3,7) + mmKtot(3,8) );
674     Stiff(4,0) = Stiff(0,4);
675     Stiff(4,1) = Stiff(1,4);
676     Stiff(4,2) = Stiff(2,4);
677     Stiff(4,3) = Stiff(3,4);
678     Stiff(4,4) = .5 * ( mmKtot(5,5) + mmKtot(5,6) );
679     Stiff(4,5) = .5 * ( mmKtot(5,7) + mmKtot(5,8) );
680     Stiff(5,0) = Stiff(0,5);
681     Stiff(5,1) = Stiff(1,5);
682     Stiff(5,2) = Stiff(2,5);
683     Stiff(5,3) = Stiff(3,5);
684     Stiff(5,4) = Stiff(4,5);
685     Stiff(5,5) = .5 * ( mmKtot(8,7) + mmKtot(8,8) );
686 }
687 }

```

## COLOPHON

This document was typeset using L<sup>A</sup>T<sub>E</sub>X. The document layout was generated using the `arsclassica` package by Lorenzo Pantieri with updates to the title format by Mark Aarsen. The package is an adaption of the original `classicthesis` package from André Miede.

